

LEVEL II

ARO 13635.5-PX

March 13, 1979

Final Report, MP 79-16

12

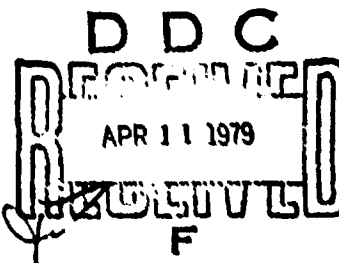
PHOTODISSOCIATION CROSS SECTIONS AND SPECTROSCOPY  
OF ATMOSPHERIC POSITIVE IONS

By: G. P. Smith, L. C. Lee, P. C. Cosby,  
J. R. Peterson, and J. T. Moseley  
Molecular Physics Laboratory

U.S. ARMY RESEARCH OFFICE  
Research Triangle Park, N.C. 27709

Contract DAAG29-76-C-0200  
SRI Project PYU-4909

Approved for Public Release;  
Distribution Unlimited.



SRI International  
333 Ravenswood Avenue  
Menlo Park, California 94025  
(415) 326-6200  
Cable: SRI INTL MNP  
TWX: 910-373-1248

Best Available Copy

AD A0 67186

DDC FILE COPY



79 04 09

Unclassified

18

AND

19

17135.5-PX

SECURITY CLASSIFICATION OF THIS PAGE (When Data Entered)

REPORT DOCUMENTATION PAGE		READ INSTRUCTIONS BEFORE COMPLETING FORM
1. REPORT NUMBER	2. GOVT ACCESSION NO.	3. RECIPIENT'S CATALOG NUMBER
4. TITLE (and Subtitle)		5. TYPE OF REPORT & PERIOD COVERED
Photodissociation Cross Sections and Spectroscopy of Atmospheric Positive Ions		Final Report. 16 Feb 1976 - 15 Feb 1979
6. AUTHOR(s)		7. PERFORMING ORG. REPORT NUMBER
G. P. Smith, L. C. Lee, P. C. Cosby, J. R. Peterson, J. T. Moseley		MP 79-16
8. PERFORMING ORGANIZATION NAME AND ADDRESS		9. CONTRACT OR GRANT NUMBER(s)
SRI International/ 333 Ravenswood Avenue Menlo Park, CA 94025		DAAG29-76-C-0020
10. CONTROLLING OFFICE NAME AND ADDRESS		11. REPORT DATE
U.S. Army Research Office P.O. Box 12211 Research Triangle Park, NC 27709		March 1979
12. MONITORING AGENCY NAME & ADDRESS (if different from Controlling Office)		13. NUMBER OF PAGES
12/62p		71
14. DISTRIBUTION STATEMENT (of this Report)		15. SECURITY CLASS. (of this report)
Approved for public release; distribution unlimited.		Unclassified
16. DISTRIBUTION STATEMENT (of the abstract entered in Block 20, if different from Report)		17a. DECLASSIFICATION/DOWNGRADING SCHEDULE
18. SUPPLEMENTARY NOTES		
The findings in this report are not to be construed as an official Department of the Army position, unless so designated by other authorized documents.		
19. KEY WORDS (Continue on reverse side if necessary and identify by block number)		
photodissociation                      sunlight photodissociation rates positive ions atmospheric ions drift tube mass spectrometer		
20. ABSTRACT (Continue on reverse side if necessary and identify by block number)		
Photodissociation cross sections have been measured for the atmospheric positive ions $O_4^+$ , $NONO^+$ , $N_4^+$ , $CO_2CO_2^+$ , $CO_4^+$ , $O_2^+-H_2O$ , and $O_2^+(2H_2O)$ at wavelengths between 3500 and 8400 Å using a drift tube mass spectrometer coupled with an argon or krypton ion laser or a tunable dye laser. Upper limits were set for the ions $COCO^+$ , $NO^+CO_2$ , $NO^+N_2$ , $NO^+nH_2O$ , and $H_3O^+nH_2O$ . Solar photolysis rates for these ions were calculated.		

DD FORM 1 JAN 72 1473

EDITION OF 1 NOV 68 IS OBSOLETE

Unclassified

SECURITY CLASSIFICATION OF THIS PAGE (When Data Entered)

1110 281

## CONTENTS

INTRODUCTION	1
RESEARCH PROGRAM	1
SUMMARY OF RESULTS	3
DISCUSSION	12
APPENDICES	
A. PHOTODISSOCIATION OF ATMOSPHERIC POSITIVE IONS. I. 5300-6700 Å	
B. LASER-ION COAXIAL BEAMS SPECTROMETER	
C. PHOTODISSOCIATION CROSS SECTIONS OF $\text{Ne}^+$ , $\text{Ar}_2^+$ , $\text{Kr}_2^+$ , AND $\text{Xe}_2^+$ FROM 3500 TO 5400 Å	
D. PHOTODISSOCIATION OF ATMOSPHERIC POSITIVE IONS. II. 3500-8600 Å	

ACCESSION for	
NTIS	White Section <input checked="" type="checkbox"/>
DDC	Buff Section <input type="checkbox"/>
UNANNOUNCED	<input type="checkbox"/>
JUSTIFICATION	
BY	
DISTRIBUTION AVAILABILITY CODES	
Dist.	Avail. or SPECIAL
A	

## INTRODUCTION

The main purpose of the research supported under this contract was to measure the photodissociation cross sections of positive ions occurring in the D-region of the ionosphere and in other ionized gases important in Army applications. The ionosphere is of importance to the Army because the free electron density in that region directly affects radar and radio transmission. This density is controlled by ion chemistry and photochemistry. Positive ion photodissociation rates are thus needed for modeling calculations of the ionosphere under normal and disturbed conditions. We have studied the photodissociation of important atmospheric positive ions from 3500 to 8500 Å and have estimated the effect of such processes on the D-region ion chemistry. We have also studied the photodissociation of rare gas dimer ions, which are important in the development of excimer lasers.

A second goal of these investigations was to examine the electronic states and bonding of weakly bound positive ions, such as the ionospheric cluster ions. Photodissociation of positive ions can be an important power-loss process in e-beam and gas discharge lasers, and a general model should prove useful in future developments and applications of interest to the U.S. Army.

## RESEARCH PROGRAM

During the first contract year, measurements were begun on the photodissociation cross sections of a large number of atmospheric positive ions from 5300 to 6700 Å, using the drift tube mass spectrometer-tunable dye laser apparatus. Dimer ions such as  $\text{NONO}^+$  had large cross sections, and the measurements were affected by diffusion. In contrast

to our measurements with negative atmospheric ions, fast equilibrium reactions couple many of the positive cluster ions studied and were also found to affect the measurements. We successfully modeled these systems kinetically, and by careful control and variation of drift tube conditions we have been able to eliminate this source of error in the measurements. This work is summarized in the paper "Photodissociation of Atmospheric Positive Ions I. 5300-6700 Å," published in The Journal of Chemical Physics; this paper is attached as Appendix A.

Also during this year, we completed construction of the photofragment spectrometer, which can provide more detailed measurements on ion photodissociation processes. This construction was done primarily under other sponsorship, but was partially supported by this contract. A copy of the article "A Laser-Ion Coaxial Beams Spectrometer," which appeared in Review of Scientific Instruments, is included as Appendix B. It describes the apparatus and the detailed information derivable from such experiments.

During the second year of this research program, detailed photodissociation cross section measurements were made for the major D-region ions from 5300 to 8600 Å. This extended the previous work to longer wavelengths. Preliminary work at shorter wavelengths was begun using the  $\text{Kr}^+$  laser lines between 4765 and 5309 Å. Measurements were also begun on the rare gas dimer ions  $\text{Ne}_2^+$ ,  $\text{Ar}_2^+$ ,  $\text{Kr}_2^+$ , and  $\text{Xe}_2^+$  at  $\text{Ar}^+$  and  $\text{Kr}^+$  laser lines between 3507 and 5309 Å. Results for these potential absorbers within the cavities of excimer lasers are given in Appendix C, a preprint of a paper to appear in Physical Review A. Development of a high pressure positive cluster ion source for the photofragment spectrometer apparatus was also initiated.

During the final year of this contract, photodissociation cross section measurements on the positive atmospheric ions were completed for the  $\text{Ar}^+$  and  $\text{Kr}^+$  laser lines between 3500 and 5300 Å. A paper

summarizing these results and the longer wavelength results, entitled "Photodissociation of Atmospheric Positive Ions II. 3500-8400 Å" and published in the Journal of Chemical Physics is attached as Appendix D. This paper also discusses the nature of the electronic states of positive cluster ions, as deduced from these measurements. The photodissociation cross sections of  $\text{CO}_4^+$  and  $\text{O}_2^+ \cdot \text{H}_2\text{O}$  were examined in greater detail by dye laser measurements from 4250 to 4500 Å, but no structure was observed.

Based on the data from this research, total sunlight photodissociation rates or upper limits have been calculated for the D-region positive ions. The implications of these rates on ionospheric chemistry will be discussed in a manuscript to be submitted to the Journal of Geophysical Research. An attempt was made to examine the photofragment spectroscopy of  $\text{O}_4^+$  and  $\text{O}_2^+ \cdot \text{H}_2\text{O}$ . Resolvable kinetic energy spectra could not be obtained, primarily because of vibrational excitation in the ions. Thus a more detailed understanding of polyatomic positive cluster ion photodissociation will require further ion source development.

#### SUMMARY OF RESULTS

While the publications attached as appendices (particularly Appendix D) provide a thorough discussion of research under this contract, a complete summary of the data is given here, and our major conclusions are discussed. Figures 1 through 7 graphically present the photodissociation cross section data for the ions  $\text{O}_4^+$ ,  $\text{HONO}^+$ ,  $\text{CO}_2\text{CO}_2^+$ ,  $\text{N}_4^+$ ,  $\text{O}_2^+ \cdot \text{H}_2\text{O}$ ,  $\text{O}_2^+ \cdot 2\text{H}_2\text{O}$ , and  $\text{CO}_4^+$ . Table 1 summarizes these data for wavelengths at roughly 0.1 eV intervals and includes upper limits for ions such as  $\text{NO}^+ \cdot \text{H}_2\text{O}$ ,  $\text{H}_3\text{O}^+ \cdot n\text{H}_2\text{O}$ ,  $\text{NO}^+ \cdot \text{N}_2$ ,  $\text{NO}^+ \cdot \text{CO}_2$ , and  $\text{COCO}^+$ . Total sunlight photodissociation rates are also given.

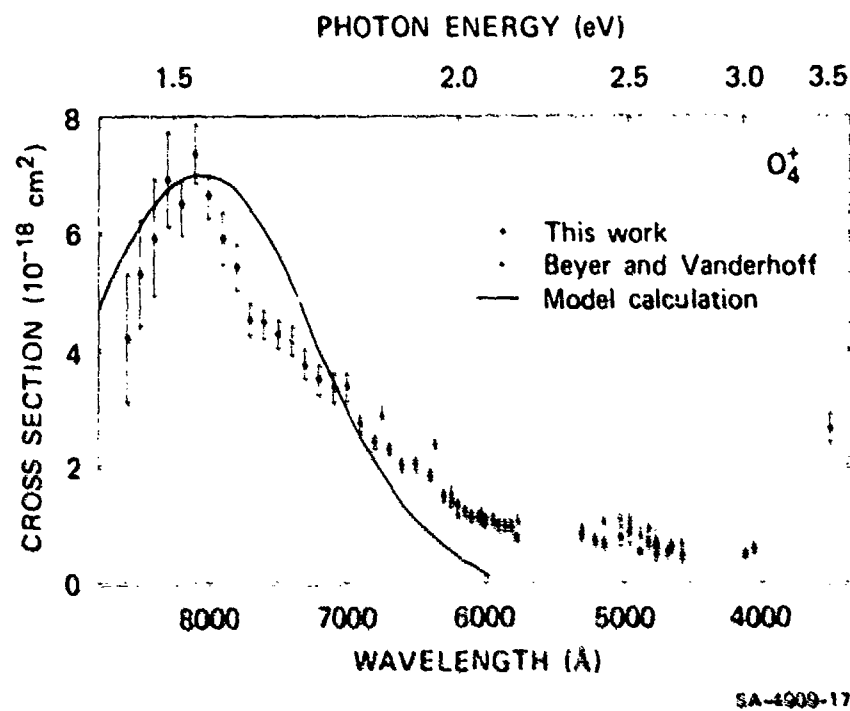
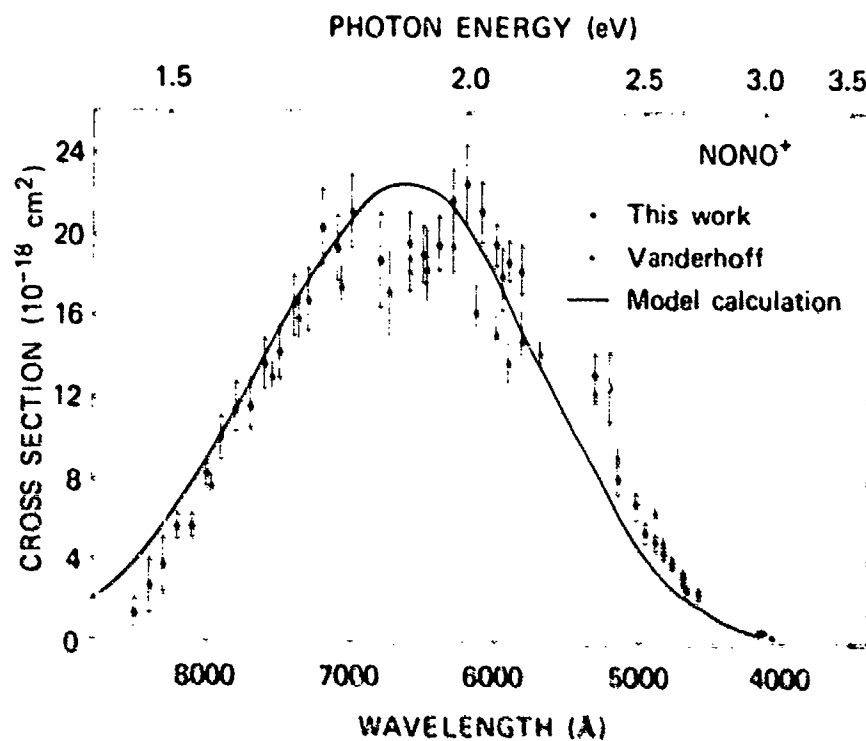


FIGURE 1 PHOTODISSOCIATION CROSS SECTIONS FOR  $O_4^+$

Filled triangles are the data of R. A. Beyer and J. A. Vanderhoff, J. Chem. Phys. 65, 2313 (1976). The model calculation is described in Appendix D.



SA-4909-16

FIGURE 2 PHOTODISSOCIATION CROSS SECTIONS FOR  $\text{NONO}^+$

Filled triangles are the data of J. A. Vanderhoff, J. Chem. Phys. 67, 2332 (1977). The model calculation is described in Appendix D.



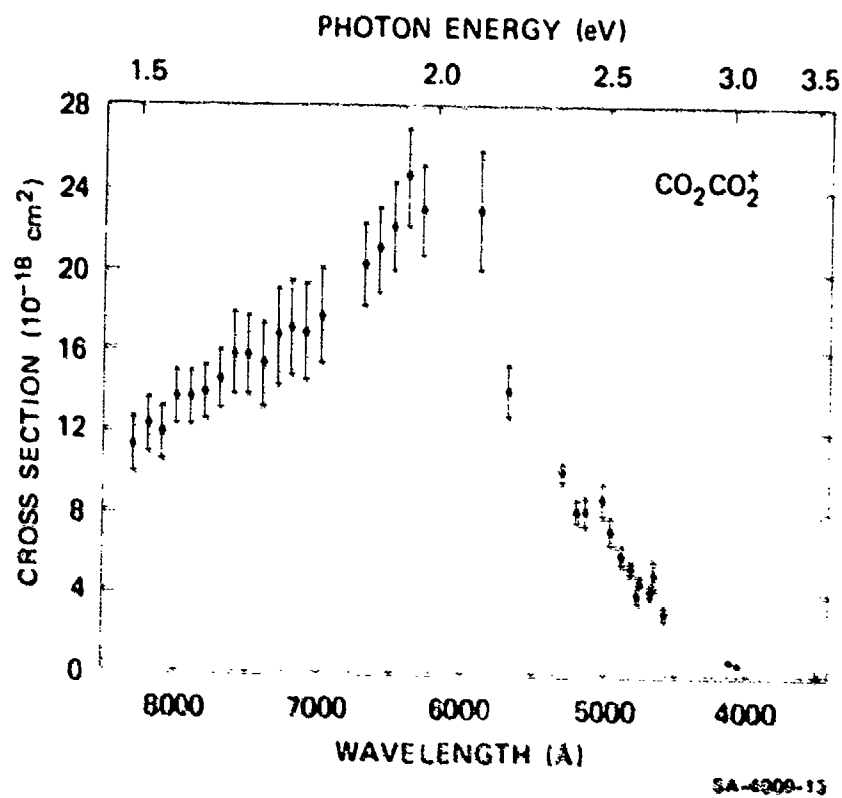


FIGURE 3 PHOTODISSOCIATION CROSS SECTIONS FOR  $\text{CO}_2\text{CO}_2^+$

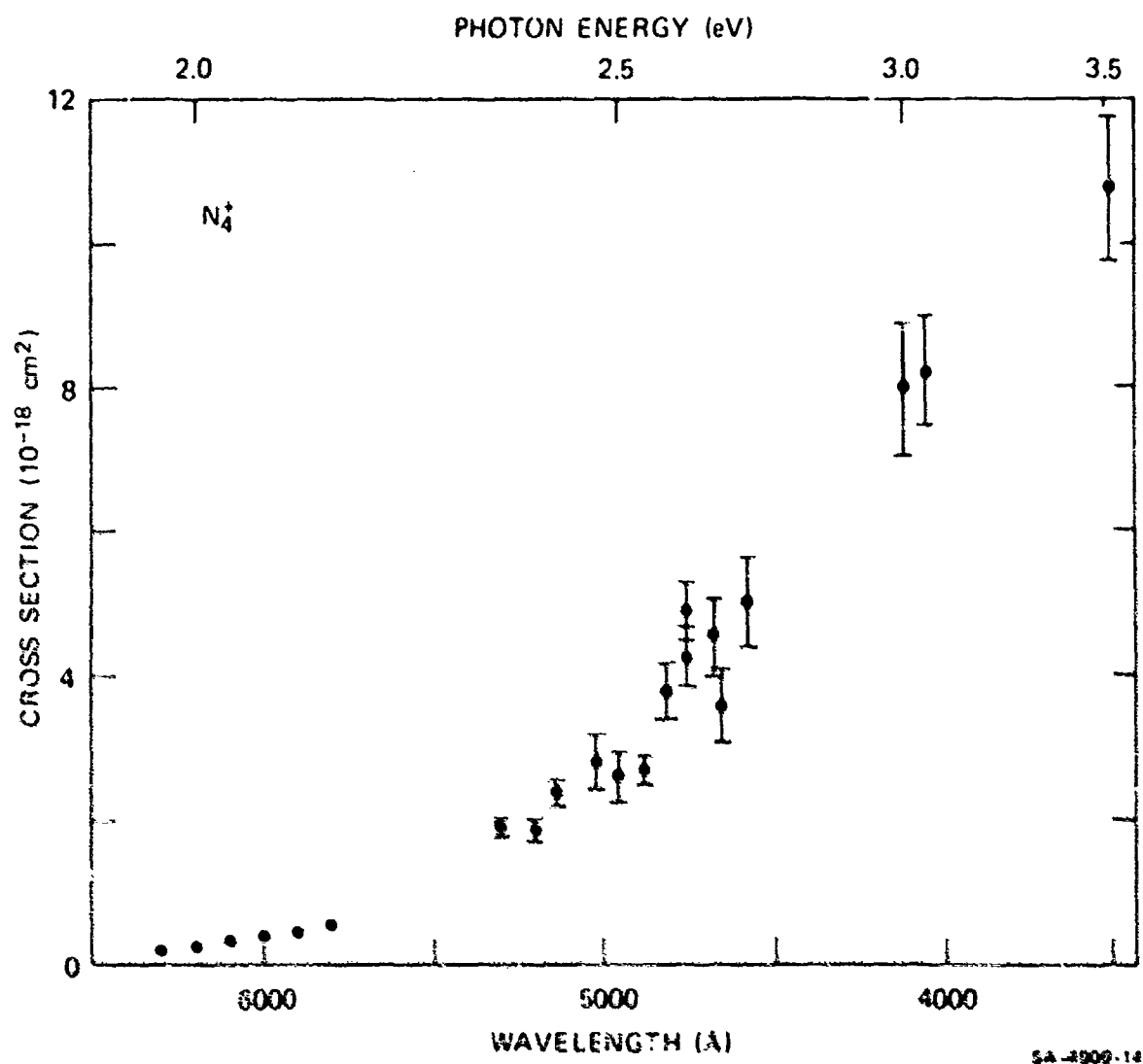


FIGURE 4 PHOTODISSOCIATION CROSS SECTIONS FOR  $N_4^+$

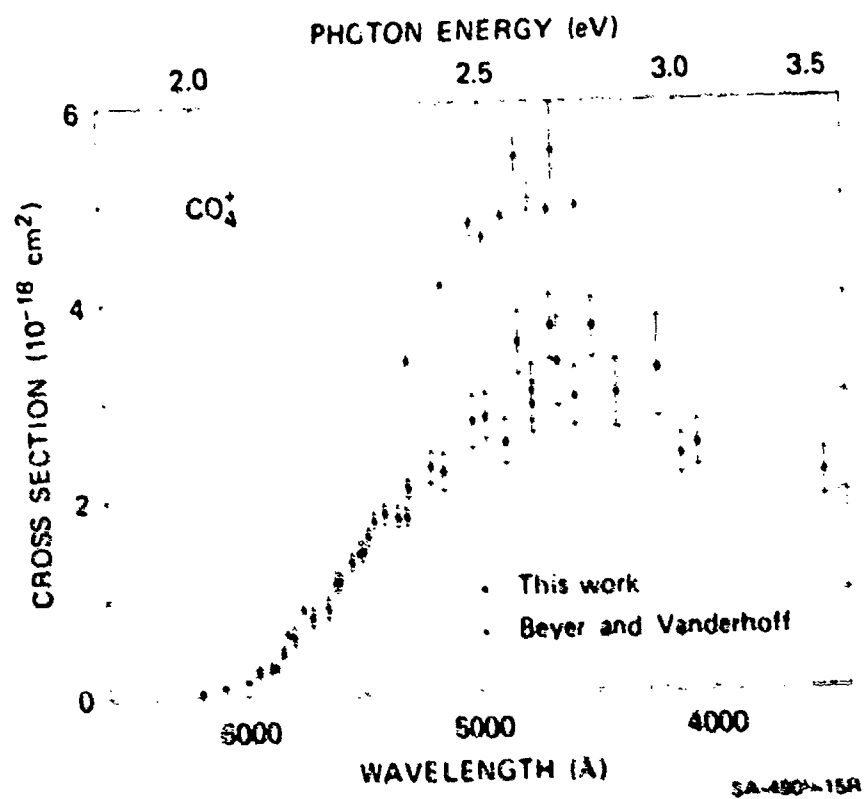
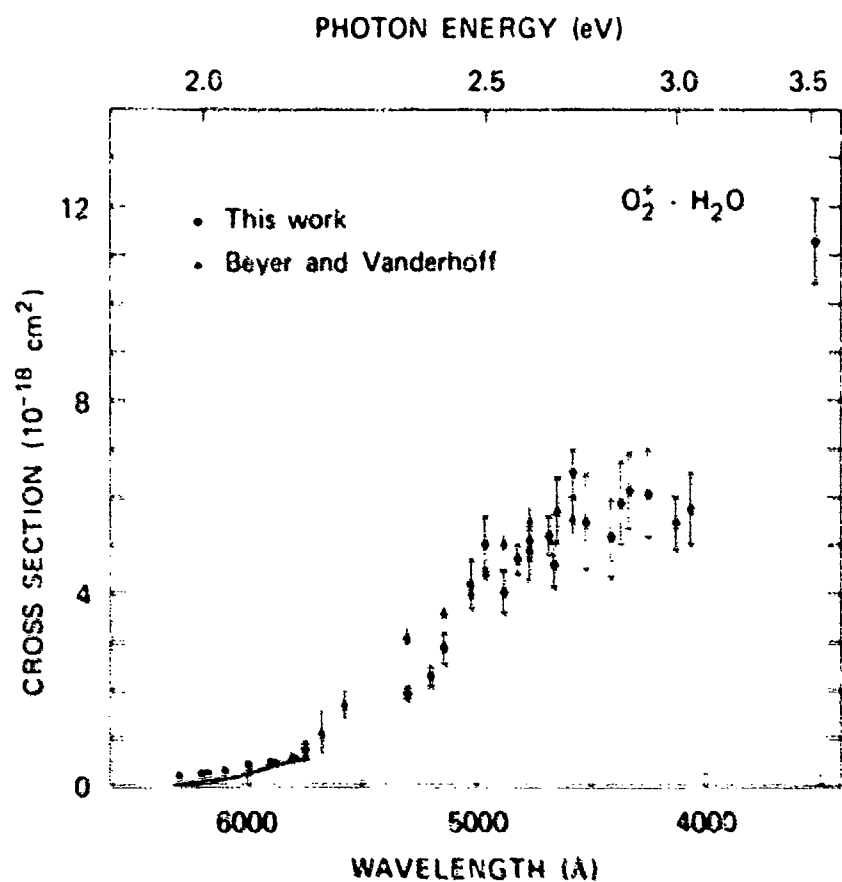


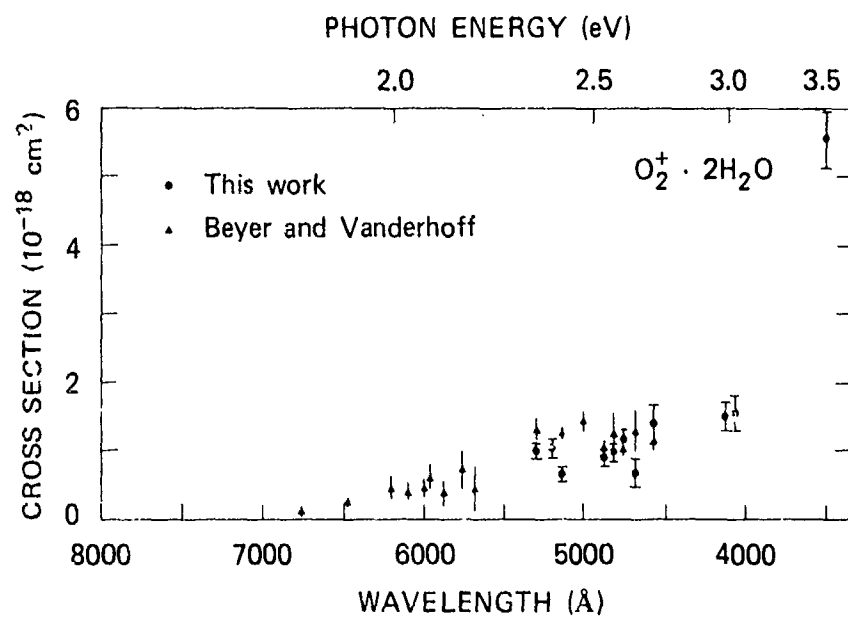
FIGURE 5 PHOTODISSOCIATION CROSS SECTION FOR  $\text{CO}_2^+$   
 Triangles are the data of R. A. Beyer and J. A. Vanderhoff, J. Chem. Phys. 65, 2313 (1976).



SA-4909-11R

FIGURE 6 PHOTODISSOCIATION CROSS SECTIONS FOR  $O_2^+ \cdot H_2O$

Triangles are the data of R. A. Beyer and J. A. Vanderhoff, *J. Chem. Phys.* 65, 2313 (1976). Solid line is the true long wavelength cross section, as discussed in Appendix A.



SA-4909-12

FIGURE 7 PHOTODISSOCIATION CROSS SECTIONS FOR  $\text{O}_2^+ \cdot 2\text{H}_2\text{O}$

Triangles are the data of R. A. Beyer and J. A. Vanderhoff, J. Chem. Phys. 65, 2313 (1976).

Table 1

D-REGION POSITIVE ION PHOTODISSOCIATION CROSS SECTIONS ( $10^{-18} \text{ cm}^2$ )<sup>\*</sup>

$\lambda$ (Å)	1.50	1.66	1.75	1.82	1.91	2.00	2.14	2.26	2.35	2.57	2.60	2.65	2.71	3.00	3.50	Solar Loss Rate ( $\text{s}^{-1}$ )
$\text{O}_4^+$	6.9	4.25	3.35	2.45	1.6	1.3	1.0		0.83	0.75	0.63	0.65	0.48	0.49	2.64	$0.59 \pm .07$
$\text{NO}^+\text{CO}_2^+$	3.6	14.2	19.4	18.7	19.0	22.5	18.2		13.1	12.6	4.34	3.88	2.36	0.46	<0.06	$2.7 \pm .3$
$\text{CO}_2\text{CO}_2^+$	11.3	15.7	17.0	20.2	22.0	23.0	14.9		9.95	8.15	5.18	4.63	3.09	0.68	<0.06	$3.7 \pm .1$
$\text{N}_4$		<0.03	<0.07			0.20	0.55		1.96	1.88	3.79	5.10	5.05	7.97	10.8	$0.42 \pm .10$
$\text{COO}^+$		<0.05							<0.02	<0.07	<0.04	<0.09		<0.05	<0.03	<.02
$\text{CO}_4^+$							0.60	1.85	1.79	2.32	3.55	3.05	3.01	2.44	2.50	$0.21 \pm .02$
$\text{O}_2^+\text{H}_2\text{O}$						0.10	0.50		1.93	2.34	4.67	5.07	6.55	5.46	5.75	$0.42 \pm .10$
$\text{O}_2^+\text{H}_2\text{O}$									1.02	1.07	0.97	1.14	1.39	1.50	1.56	$0.13 \pm .05$
$\text{NO}^+\text{H}_2$								<0.04	<0.20			<0.32		<0.47	<0.157	<0.10
$\text{NO}^+\text{CO}_2$								<0.09	<0.09	<0.19	<0.16	<0.11		<0.08	<0.08	<0.04
$\text{NO}^+\text{H}_2\text{O}$						<0.01	<0.02	<0.03	<0.02	<0.03	<0.07	<0.02		<0.04	<0.03	<0.02
$\text{NO}^+\text{H}_2\text{O}$						<0.01	<0.01	<0.01	<0.01	<0.01	<0.05	<0.03		<0.09	<0.14	<0.02
$\text{H}_3\text{O}^+$						<0.02	<0.04	<0.05	<0.03	<0.06	<0.10	<0.07		<0.11	<0.09	<0.02
$\text{H}_3\text{O}^+\text{H}_2\text{O}$						<0.03	<0.03	<0.04	<0.03	<0.05	<0.05	<0.07		<0.04	<0.09	<0.02
$\text{H}_3\text{O}^+\text{H}_2\text{O}$						<0.01	<0.05	<0.09	<0.03	<0.02	<0.04	<0.06		<0.05	<0.09	<0.02
$\text{H}_3\text{O}^+\text{H}_2\text{O}$									<0.02	<0.02	<0.02	<0.04		<0.04	<0.09	<0.02

\* Upper limits represent measurements consistent with zero cross sections and are based on one standard deviation statistical error. See Appendices A and D. Solar photo loss rates are calculated by the method of J. R. Peterson, J. Geophys. Res. 81, 77 (1976), for wavelengths longer than 3500 Å.

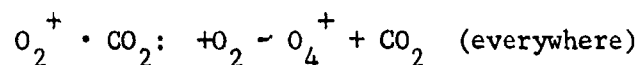
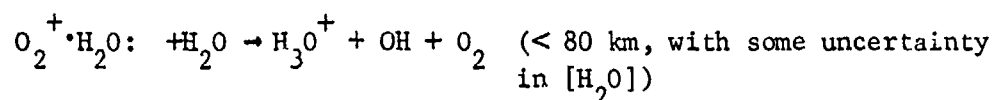
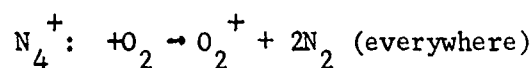
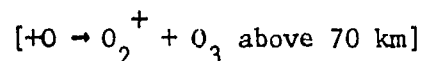
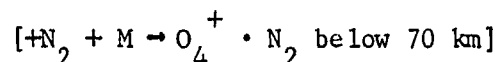
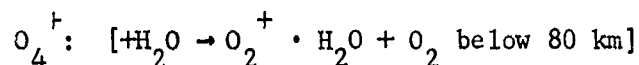
## DISCUSSION

The photodissociation of weakly bound positive atmospheric cluster ions can be characterized in terms of a pseudo-diatomic model. Dimer ions such as  $\text{NONO}^+$  have large ( $> 1 \times 10^{-17} \text{ cm}^2$ ), smooth, bell-shaped cross sections. The peaks occur at shorter wavelengths for the more strongly bound dimers. This indicates a repulsive upper state and suggests a pseudo-diatomic model for the potential surfaces analogous to  $\text{H}_2^+$  (or  $\text{Ar}_2^+$ ). For mixed clusters  $\text{A}^+ \cdot \text{B}$ , which are bound by weak electrostatic forces, the analogous surfaces are separated by an additional term representing the difference in A and B ionization potentials. Thus smooth, albeit smaller ( $\sim 5 \times 10^{-18} \text{ cm}^2$ ), cross sections are seen for  $\text{O}_2^+ \cdot \text{H}_2\text{O}$  and  $\text{CO}_4^+ (\text{O}_2^+ \cdot \text{CO}_2)$ , indicating a repulsive upper state of  $\text{B}^+ \cdot \text{A}$  configuration. Cluster ions of  $\text{NO}^+$  and  $\text{H}_3\text{O}^+$  do not photodissociate at wavelengths longer than  $3500 \text{ \AA}$  because of the large difference in parent and ligand ionization potentials. Thus  $\text{NO}^+ \cdot \text{H}_2\text{O}$  does not photodissociate at wavelengths longer than  $3700 \text{ \AA}$  (3.35 eV), the difference in the NO and  $\text{H}_2\text{O}$  ionization potentials.

Examination of D-region metal ion clusters was included in the proposed research under this contract. However, in view of this model and the low metal ionization potentials, these ions almost certainly do not photodissociate at wavelengths longer than  $3500 \text{ \AA}$ . For example, for  $\text{Na}^+ \cdot \text{H}_2\text{O}$ , the ionization potential difference predicts a threshold above 7.4 eV ( $1700 \text{ \AA}$ ).

The sunlight photodissociation rates for these ions were calculated and are listed in Table 1. Although the photodissociation of several of the atmospheric ions occurs readily and their rates for photodestruction by the incident solar photon flux are close to  $1 \text{ sec}^{-1}$ , these dissociating ions are all more rapidly destroyed by ion-molecule

reactions in the earth's atmosphere. For those ions that are likely to occur in the ionosphere, the more important destruction mechanisms are:



The ions  $NO^+ \cdot NO$  and  $CO_2^+ \cdot CO_2$  are unlikely to be formed in the earth's atmosphere.

The positive ions that are relatively stable against two-body collisional destruction (charge transfer or ion switching) are also stable against photodissociation. These are the clusters of  $NO^+$  and  $H_3O^+$ . Their stability in both cases is due to their low electron recombination energy compared with the ionization potential of the neutral clustering or collision partner. It is thus apparent that the only processes destroying  $H_3O^+$  hydrates are ion-ion neutralization or three-body association to larger clusters. Photodestruction is possible at high photon energies where absorptions can occur to excited  $H_3O^+$  or  $H_2O$  states, but this will be a very slow process. The ion-ion neutralization rates are apparently quite slow, for higher hydrates, so this stability may allow the buildup of very large clusters.



A paper presenting the sunlight photodestruction rates calculated from the cross-section data for both positive and negative ions is being prepared for publication. These rates will be compared with those of other destruction mechanisms at altitudes above 50 km, and their ionospheric importance will be discussed.

# Photodissociation of atmospheric positive ions. I. 5300–6700 Å<sup>a)</sup>

G. P. Smith, P. C. Cosby, and J. T. Moseley

*Molecular Physics Center, Stanford Research Institute, Menlo Park, California 94025*

(Received 9 June 1977)

Photodissociation cross sections have been investigated for several positive ions of atmospheric importance in the wavelength region from 5300 to 6700 Å, using a drift tube mass spectrometer and a tunable dye laser. The dimer ions  $\text{NONO}^+$  and  $\text{CO}_2\text{CO}^+$  are observed to have large photodissociation cross sections ( $> 10^{-17} \text{ cm}^2$ ) at these wavelengths. Three ions formed from oxygen cations  $\text{O}_2^+$ ,  $\text{CO}_2^+$ , and  $\text{O}_2^+\cdot\text{H}_2\text{O}$  have photodissociation cross sections near  $1 \times 10^{-18} \text{ cm}^2$ , with the latter two ions exhibiting a threshold near 6200 Å. The cluster ions  $\text{NO}^+\cdot\text{M}$ , where M is  $\text{H}_2\text{O}$ ,  $\text{N}_2$ ,  $\text{CO}_2$ , and  $\text{N}_2\text{O}$ , are not observed to photodissociate, nor are  $\text{H}_3\text{O}^+\cdot(\text{H}_2\text{O})_n$ . Upper limits on the photodissociation cross sections for these ions are established in the range  $10^{-19}$ – $10^{-20} \text{ cm}^2$ . For many of the ions studied here reactions coupling the ion of interest with other species present in the drift tube and diffusion effects following interaction with the laser must be explicitly considered to establish values or limits for the photodissociation cross sections.

## I. INTRODUCTION

Current attempts to understand and model the lower ionosphere require consideration of many positive ions,<sup>1</sup> such as  $\text{CO}_2^+$ ,  $\text{O}_2^+$ ,  $\text{O}_2^+\cdot\text{H}_2\text{O}$ , clusters of  $\text{NO}^+$ , and  $\text{H}_3\text{O}^+\cdot(\text{H}_2\text{O})_n$ . Since these ions are typically weakly bound,<sup>2</sup> photodissociation by visible sunlight is potentially important in the positive ion chemistry. In addition, photodissociation studies of ions can provide structural and energetic information on the molecular electronic states,<sup>3</sup> hence aiding our understanding of such ionic environments as gas discharges and lasers. We report here photodissociation cross sections, generally between 5300 and 6700 Å, for the following positive ions:  $\text{NONO}^+$ ,  $\text{CO}_2\text{CO}^+$ ,  $\text{O}_2^+$ ,  $\text{O}_2^+\cdot\text{H}_2\text{O}$ , and  $\text{CO}_2^+$ . We have also determined upper limits for the photodissociation cross sections of  $\text{NO}^+\cdot\text{CO}_2$ ,  $\text{NO}^+\cdot\text{N}_2\text{O}$ ,  $\text{NO}^+\cdot\text{H}_2\text{O}$ ,  $\text{NO}^+\cdot\text{N}_2$ , and the hydrates of  $\text{H}_3\text{O}^+$ . In addition, we have investigated the effects of diffusion and of equilibrium reactions on the measurement of photodestruction cross sections using drift tube techniques, and have developed a kinetic model for assisting in the interpretation of data obtained when these effects are important.

## II. EXPERIMENTAL PROCEDURE

The drift tube mass spectrometer and tunable dye laser apparatus used in these experiments has been described in detail previously.<sup>4</sup> Ions are formed by electron impact ionization of various gas mixtures in the source region, and by subsequent ion-molecule reactions. The mixtures and pressures (0.05–0.4 Torr) used are given in Table I for the various ions studied. The ratio of the weak applied electric field (which causes the ions to drift along the tube) to the gas density  $E/N$  is chosen so that the thermal velocity of the ions is much greater than the drift velocity. A typical  $E/N$  of 10 Td ( $10^{-16} \text{ V cm}^2$ ) coupled with a long drift distance (20 cm) insures many thermalizing collisions be-

fore the ions reach the laser interaction region. In most cases the de-excitation of ions was investigated by varying the pressure, drift distance, and  $E/N$ . However, when new ions are being formed all along the drift tube, even after equilibrium is established, some vibrationally excited ions may be present in the laser region.

The drifting ions intersect the 2 mm diameter dye laser beam, which is perpendicular to the drift field, and then drift approximately 1 mm to an extraction aperture at the end of the drift region. The ions exit the drift region into a high vacuum region where they are mass selected by a quadrupole and detected individually by an electron multiplier. The laser is a jet stream dye laser, and is pumped by a chopped 16 W argon ion laser beam. Photon absorption by the ions takes place inside the dye laser cavity. The dyes sodium fluorescein (5300–5700 Å), rhodamine 6G (5700–6300 Å), and rhodamine B (6000–6700 Å) were used.

The absolute photodissociation cross section  $\sigma$  at wavelength  $\lambda$  is given by

$$\sigma(\lambda) = G \ln(I_0/I) / t \Phi(\lambda), \quad (1)$$

where  $I_0/I$  is the ratio of ion intensities laser off/laser on,  $t$  is the average time for an ion to traverse the laser beam,  $\Phi$  is the photon flux, and  $G$ , a dimensionless number of order unity, takes into account the overlap of the laser beam with the ion swarm. It is difficult to determine this geometrical factor  $G$  accurately. Uncertainties in the laser beam diameter and spatial distribution make it advantageous to normalize the results to the known  $\text{O}^+$  and/or  $\text{O}_2^+$  photodetachment cross sections.<sup>5</sup> The normalization method effectively determines an experimental value for  $G$ . This previously described procedure<sup>5</sup> requires measurement of the  $\text{O}^+$  or  $\text{O}_2^+$  photodetachment cross section before or after each experiment, and a knowledge of the relative mobilities of the ions which determine the relative values of  $t$  in Eq. (1). The absolute uncertainty in a cross section derived from this procedure is roughly 20%.

<sup>a)</sup>This research was supported by the U. S. Army Research Office.

TABLE I. Experimental conditions.

No.	Ion	Gas	P(Torr)	Drift distance (cm)	E/N (Td)	$\mu$ (cm <sup>2</sup> /Vs)	Normalized	$\mu_{\text{ref}}$ (cm <sup>2</sup> /Vs)
1	O <sub>2</sub> <sup>+</sup>	O <sub>2</sub>	0.250	10	5	2.08 <sup>a</sup>	O <sub>2</sub> <sup>+</sup> in O <sub>2</sub>	2.16 <sup>a</sup>
2	NONO <sup>+</sup>	NO	0.200	30	10	1.78 <sup>a</sup>	O <sub>2</sub> <sup>+</sup> in NO	2.03 <sup>d</sup>
3	NONO <sup>+</sup>	2.5% O <sub>2</sub> in N <sub>2</sub> O	0.400	30	varied	1.45 <sup>b</sup>	O <sub>2</sub> <sup>+</sup> in N <sub>2</sub> O	1.52 <sup>b</sup>
4	NONO <sup>+</sup>	10% NO in Ar	0.200	30	10	2.2 <sup>c</sup>	O <sub>2</sub> <sup>+</sup> in O <sub>2</sub>	2.16 <sup>a</sup>
5	CO <sub>2</sub> CO <sub>2</sub> <sup>+</sup>	CO <sub>2</sub>	0.050	30	10	1.22 <sup>d</sup>	CO <sub>2</sub> <sup>+</sup> in CO <sub>2</sub>	1.3 <sup>a</sup>
6	NO <sup>+</sup> ·(H <sub>2</sub> O) <sub>n</sub> n = 1, 2	CO <sub>2</sub> , < 1% NO, H <sub>2</sub> O	0.400	30	10	1.37, 1.28 <sup>d</sup>	CO <sub>2</sub> <sup>+</sup> in CO <sub>2</sub>	1.3 <sup>a</sup>
7	O <sub>2</sub> <sup>+</sup> ·H <sub>2</sub> O	O <sub>2</sub> , < 0.2% H <sub>2</sub> O	0.400	30	10	2.1 <sup>a</sup>	O <sub>2</sub> <sup>+</sup> in O <sub>2</sub>	2.1 <sup>a</sup>
8	CO <sub>2</sub> <sup>+</sup>	3% O <sub>2</sub> in CO <sub>2</sub>	0.400	30	10	1.28 <sup>d</sup>	O <sub>2</sub> <sup>+</sup> in O <sub>2</sub>	2.16 <sup>a</sup>
		O <sub>2</sub> , CO <sub>2</sub> 50%	0.250	20	10	1.64 <sup>f</sup>	O <sub>2</sub> <sup>+</sup> in O <sub>2</sub>	2.16 <sup>a</sup>
9	NO <sup>+</sup> ·N <sub>2</sub>	N <sub>2</sub> , < 0.5% NO	0.400	20	10	2.3 <sup>a</sup>	NONO <sup>+</sup> in NO	2.3 <sup>a</sup>
10	NO <sup>+</sup> ·CO <sub>2</sub>	CO <sub>2</sub> , < 10% NO	0.250	20	10	1.25 <sup>d</sup>	CO <sub>2</sub> <sup>+</sup> in CO <sub>2</sub>	1.3 <sup>a</sup>
11	NO <sup>+</sup> ·N <sub>2</sub> O	N <sub>2</sub> O	0.400	20	varied	1.25 <sup>d</sup>	O <sub>2</sub> <sup>+</sup> in N <sub>2</sub> O	1.52 <sup>b</sup>
12	H <sub>2</sub> O <sup>+</sup> ·(H <sub>2</sub> O) <sub>n</sub> n = 0, 1, 2	O <sub>2</sub> , < 1% H <sub>2</sub> O	0.200	20	10	2.83, 2.36, 2.22 <sup>h</sup>	O <sub>2</sub> <sup>+</sup> in O <sub>2</sub>	2.16 <sup>a</sup>

<sup>a</sup>Reference 10.<sup>b</sup>Measured.<sup>c</sup>Scaled from O<sub>2</sub><sup>+</sup> in Ar.<sup>d</sup>Scaled from CO<sub>2</sub><sup>+</sup> in CO<sub>2</sub>.<sup>e</sup>Scaled from O<sub>2</sub><sup>+</sup> and O<sub>2</sub><sup>+</sup> in O<sub>2</sub>.<sup>f</sup>Blanc's law average (see Ref. 8) of CO<sub>2</sub><sup>+</sup> in CO<sub>2</sub> and CO<sub>2</sub><sup>+</sup> in O<sub>2</sub>.<sup>g</sup>Value for N<sub>2</sub><sup>+</sup> in N<sub>2</sub>, Ref. 10 (also value for scaling from CO<sub>2</sub><sup>+</sup> in N<sub>2</sub>).<sup>h</sup>Scaled from values in N<sub>2</sub>: I. Dotan, D. Albritten, W. Lindinger, and M. Pahl, J. Chem. Phys. 65, 5028 (1976).<sup>i</sup>Scaled from NONO<sup>+</sup> mobility in NO (Ref. 10).

plus the statistical error associated with the positive ion photodissociation measurement. This statistical error, the precision of the measurements, is indicative of the relative error versus wavelength, and is given by the error bars in the figures.

The mobilities used in these normalizations are listed in Table I, along with the experimental conditions employed in this study. Many of the required mobilities cannot be easily measured due to rapid reactions involving ions of interest in the particular gas. In such cases mobilities were estimated using previously measured values for other ions, and scaling them by the square root of the reduced mass of the ion and the gas molecule, using the Langevin theory.<sup>6</sup> This procedure is generally accurate to within 10%, except for cases where resonant charge exchange is important. The mobilities used, and how they were determined, are given in Table I.

Several of the positive ions studied here are distinguished by the rapidity of the ion-molecule reactions producing them in the drift tube, or by unusually large ( $> 10^{-17}$  cm<sup>2</sup>) photodissociation cross sections. Each of these characteristics requires special consideration when establishing accurate cross section in our apparatus. Sometimes a rapid equilibrium exists between the ion of interest and another ion with a large photodissociation cross section. Photodissociation of this second ion can lead to the apparent photodissociation of the first ion as the ions re-establish equilibrium. Although this effect can be detected and often reduced by changing the drift tube conditions, elimination of the in-

terfering ion often terminates the production of the desired ion, since the two are closely coupled. While we have constructed a procedure (described below) for obtaining photodissociation cross sections even when such equilibrium reactions are important, the resulting cross sections are usually less precise. In general, this effect is important whenever the reaction rate is comparable to the reciprocal of the drift time through the laser beam, and the concentration of the dissociating ion is more than 10% that of the ion of interest.

A second effect, to be discussed in detail in the next section, concerns diffusion. Since the ion swarm is larger than the laser beam diameter, ions can diffuse back into the interaction region during the short time between the laser interaction and extraction, and replace some of the photodissociated ions. For fixed conditions of laser interaction volume, E/N, pressure, and drift distance after interaction, a fixed fraction of the ions outside the interaction volume will diffuse into it, and vice versa. This effect is included in the geometrical factor G used in the calculation of the cross sections. If the fraction of ions photodissociated is linear with photon intensity [which is essentially true for dissociation fractions ( $I_0 - I$ )/ $I_0$  less than 0.1] for both the ion under investigation and the ion to which the cross section is to be normalized, the normalization procedure will correct for this effect, since the ratio of the spread of an ion swarm to the drift distance is independent of the diffusion coefficient and mobility at low E/N.<sup>6</sup> However, for larger dissociation fractions the ratio of the number of ions diffusing into the inter-

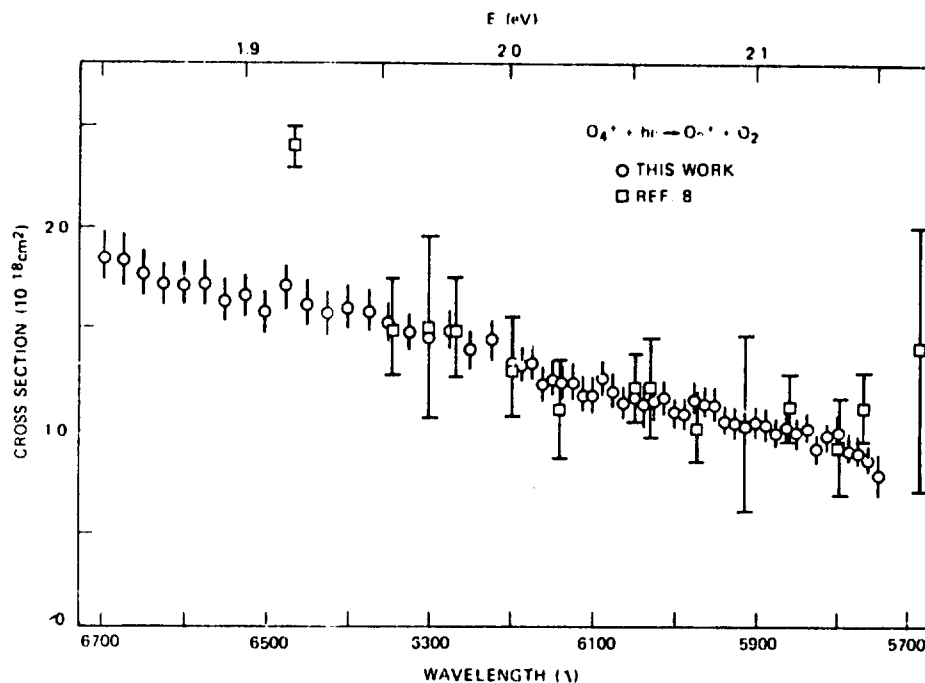


FIG. 1. Cross section for  $O_4^+$  photodissociation from 5750 to 6700 Å, comparing the present results (circles) to those from Ref. 8 (squares). Bars indicate the relative uncertainty.

action region to the number of ions diffusing out is no longer linear with photon intensity. This effect can produce an apparent dependence of the photodissociation cross section on laser intensity even though all dissociations occur via single photon absorptions. In our previous work we have always been able to work at low enough photon intensity to avoid this situation. However, two of the ions under study here  $NONO^+$  and  $CO_2CO^+$  have exceptionally large photodissociation cross sections, and thus force a more detailed consideration of diffusion effects.

The next section discusses the photodissociation of the dimer ions  $O_4^+$ ,  $NONO^+$ , and  $CO_2CO^+$ , including this diffusion effect. Section IV considers the hydrates of  $O_2^+$  and  $NO^+$ , and the effects of equilibria in the drift tube. Section V describes results on  $CO_4^+$ , while Sec. VI discusses other  $NO^+$  cluster ions. Finally, upper limits on the hydronium ion  $H_3O^+ \cdot (H_2O)_{n=0,1,2}$  photodissociation cross sections are determined in Sec. VII.

### III. DIMER IONS OF OXYGEN, NITRIC OXIDE, AND CARBON DIOXIDE

The  $O_4^+$  cross section was measured at 25 Å intervals between 5750 and 6700 Å to a precision (relative accuracy) of 7%. The ions are formed from  $O_2^+$  by the three-body reaction



with a reported rate constant<sup>7</sup>  $k = 2.5 \times 10^{-30} \text{ cm}^6/\text{s}$ . The experimental conditions and mobilities used are listed

in line 1 of Table I. Our measurements of the photodissociation cross section of  $O_4^+$  are given by the circles in Fig. 1, and show a smooth decrease with wavelength. The photodissociation of  $O_4^+$  has also been measured at 24 ion and dye laser wavelengths by Beyer and Vanderhoff.<sup>8</sup> Half of these measurements, which carry a precision of about 25%, are in our present wavelength range and are given by the squares in Fig. 1. There is excellent agreement between our results and the data of Ref. 8, except at 6471 Å. This discrepancy is not attributable to diffusion effects in our study, because the fraction of photodissociation was always below 0.15. Thus, only a very weak power dependence of the measured apparent photodissociation cross section was observed, and all reported results are extrapolations to low power. Our long wavelength results are more consistent with the shorter wavelength trend observed in both studies.<sup>8</sup> There is no statistically significant structure observed in the cross section, and  $O_4^+$  is the only energetically allowed product at these wavelengths. No pressure dependence of the cross section was observed below 250 μ, this indicating that Reaction (2) does not perturb the measurement.

Photodissociation of  $NONO^+$  was measured in NO (line 2, Table I), in a mixture of 2.5%  $O_2$  in  $N_2O$  (line 3), and in a mixture of 10% NO in Ar (line 4). For the conditions of lines 2 and 4 a three-body reaction produces  $NONO^+$  from NO:



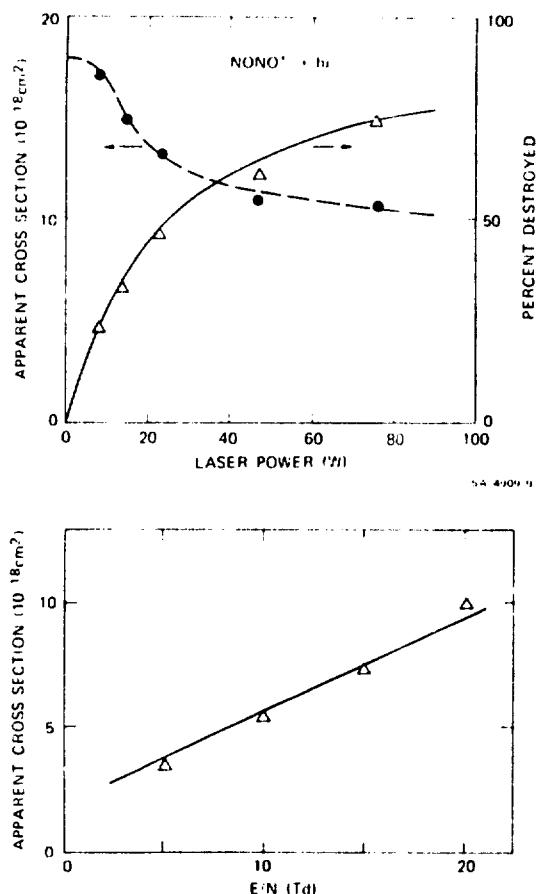


FIG. 2. The diffusion model for  $\text{NONO}^+$  photodissociation, (a) Percentage of  $\text{NONO}^+$  destroyed as a function of laser power at 5900 Å, and the resulting apparent photodissociation cross section. The points  $\Delta$  and  $\bullet$  indicate the experimental data. The solid line is the predicted destruction using the diffusion model, with  $k_D = 9000 \text{ s}^{-1}$ . The dashed line and  $\bullet$  represent the power variation in the apparent  $\text{NONO}^+$  photodissociation cross section. (b) Data and model calculation for the variation of the apparent  $\text{NONO}^+$  cross section with  $E/N$ .

with a rate constant<sup>9</sup>  $k = 5 \times 10^{-30} \text{ cm}^6/\text{s}$  ( $M = \text{NO}$ ). Care was taken to minimize the amount of water, and hence  $\text{NO}^+ \cdot \text{H}_2\text{O}$ , in the system since an equilibrium of this ion with  $\text{NONO}^+$  in  $\text{NO}$  can lower the apparent photodissociation. This effect is discussed in detail in the next section. Figure 2 shows the variation of the apparent  $\text{NONO}^+$  photodissociation cross section with laser power and with  $E/N$  at 5900 Å. The measurements are independent of the drift distance and do not vary with the fraction of  $\text{NO}$  diluted in  $\text{Ar}$  or  $\text{O}_2$ . Thus, this dependence of the apparent photodissociation cross section on laser power and on time spent by the ions traversing the laser beam ( $E/N$ ) indicates an effect on the measured apparent cross section which correlates with the fraction of dimer ions destroyed (also shown in the figure).

When a particular ion is "destroyed" by the laser a concentration gradient is established within the ion swarm, across the boundary of the laser beam. The net flux into this region attributable to diffusion is given by Fick's Law:

$$J = -DdC/dx, \quad (4)$$

where  $C$  is the ion concentration,  $D$  is the diffusion coefficient, and  $x$  is the distance normal to the laser beam axis. For our approximate scheme here with large dissociation fractions we consider diffusion occurring from regions above and below the laser, with a total volume equal to that of the laser region. Then the average  $dx$  is on the order of the laser beam radius  $r$ , and the concentration gradient  $dC/dx$  is proportional to  $(C_{\text{LASER}} - C)/r = \Delta C/x$ , where  $C_{\text{LASER}}$  is the ion concentration in the laser interaction region with the laser on. The flux equals the product of the replacement ion concentration  $\Delta C$  times the velocity  $v_D$  of the diffusing ions  $J = -v_D \Delta C$ . Now,  $v_D = x/t_D$  or  $xk_D$ , since the time for replacement  $t_D$  equals  $1/k_D$ , the ion replacement rate via diffusion. Thus,

$$J = -\Delta C v_D = -\Delta C x k_D \quad (5)$$

and

$$J = -DdC/dx = -D\Delta C/x. \quad (6)$$

Combining these equations yields  $k_D = D/x^2$ . Because  $k_D$  is independent of the ion concentrations, the magnitude of the diffusion effect varies linearly with the fraction of ions destroyed. The amount of photodissociation, however, decreases exponentially with the fraction of ions remaining, and thus the power dependence arises.

The diffusion coefficient  $D$  varies as the reduced mobility  $\kappa_0$  divided by the gas number density. Using  $x = r = 0.1 \text{ cm}$  (the approximate laser beam radius), and calculating a transverse diffusion rate constant of  $176 \text{ cm}^2/\text{s}$  from the mobility of  $\text{NONO}^+$  in  $\text{NO}$ ,<sup>10</sup> we obtain  $k_D \sim 17600 \text{ s}^{-1}$  for  $\text{NONO}^+$  in 0.200 Torr  $\text{NO}$ . However, since  $x$  is only known approximately, this analysis only indicates what order of magnitude of rates is reasonable in trying to fit the power dependence.

The rate equations for photodissociation and diffusive replacement are numerically integrated over time as the ions traverse a laser zone of  $2r = 0.2 \text{ cm}$  and a final drift zone of  $0.1 \text{ cm}$ . Note that the time integration can be replaced by a distance integration by using the drift velocity as derived from the mobility. Uncertainties in the laser interaction and final drift distance dimensions over which diffusive effects operate affect both the value of  $r$  and the limits of integration, thus contributing to the uncertainty in the value used for  $k_D = 9000 \text{ s}^{-1}$ . This fit yields a  $\text{NONO}^+$  photodissociation cross section of  $1.8 \times 10^{-17} \text{ cm}^2$  at 5900 Å. The calculations show that the effect of diffusion on the apparent cross section levels off just below the intracavity power levels to which we were able to descend, i.e., when the percent destroyed is less than 10%. At very high power, destruction of diffused ions becomes more important and the fraction of destroyed ions becomes constant, as a steady

TABLE II. Dimer ion cross sections ( $10^{-18}$  cm<sup>2</sup>).

	5725 Å	5900 Å	6000 Å	6200 Å
NONO <sup>+</sup>	17.4 ± 2.	17.2 ± 2.	17.5 ± 2.	18.5 ± 2.
CO <sub>2</sub> CO <sub>2</sub> <sup>+</sup>	23. ± 3.			
O <sub>2</sub> <sup>+</sup>	0.76 ± 0.1	1.02 ± 0.1	1.09 ± 0.1	1.32 ± 0.1

state situation arises with diffusion in the final 0.1 cm drift region becoming rate determining. At the highest powers this simple model no longer provides a reliable estimate of the true cross section.

If the diffusion and dissociation rates are increased by 35% to 12 000 and 13 000 s<sup>-1</sup>, respectively, the model predicts 68% of the NONO<sup>+</sup> ions will be destroyed by 76 W laser power. This clearly does not match the observed 74%, and so can provide an estimate of the uncertainty in this method of extrapolating the cross section measurements to low power. These higher rates lead to a photodissociation cross section which is 10% higher than that of the better fit shown in Fig. 2. Therefore, 10% is an estimate of the uncertainty in our reported NONO<sup>+</sup> cross sections due to the use of this approximate model.

The effects<sup>11</sup> of the three-body reaction (3) are too small to account for the observed power dependence. This is particularly apparent from our observations of large laser power effects on the apparent cross sections when less NO (line 4, Table I) or no NO (line 3) was used in the drift tube. Even for 0.20 Torr NO the pseudo-first order rate constant for production of NONO<sup>+</sup> from NO<sup>+</sup>,  $k' = k_3[\text{NO}]^2$ , is 250 s<sup>-1</sup>. Since the experimental concentrations of NO<sup>+</sup> and NONO<sup>+</sup> are nearly equal, this is far short of the roughly 9000 s<sup>-1</sup> required to fit the power dependence data.

The effect of diffusion on the apparent photodissociation cross section with increasing  $E/N$  is also shown in Fig. 2. Higher drift velocity and hence shorter interaction time decreases the fraction of ions dissociated, while the shorter drift time after the laser decreases the effect of diffusion. The net effect is an increase in the apparent cross section with increasing  $E/N$ , toward the true photodissociation cross section. Note that this variation of  $E/N$  was carried out at low values of  $E/N$  so that the drift velocity was always much less than thermal velocity. This tends to prevent extensive vibrational excitation of the ions which could affect the cross section.

The results of this study at 5900 Å were applied to adjust a set of data at 5700–6200 Å for the effects of diffusion on the NONO<sup>+</sup> cross section. Conditions for this experiment, in 10% NO/90% Ar, are given in line 4 of Table I. The results shown in Table II indicate a nearly constant cross section of  $1.8 \pm 0.2 \times 10^{-17}$  cm<sup>2</sup> over this range of wavelengths. A less detailed study yields a cross section of at least  $1.4 \times 10^{-17}$  cm<sup>2</sup> at 5300 Å. NO<sup>+</sup> was the photofragment observed at these wavelengths. The normalization (geometric) factor  $G$  in these measurements was essentially invariant over the

range of wavelengths reported, thus justifying our use of only one model diffusion coefficient. Nevertheless, a significant degree of uncertainty is introduced into these data by the approximate nature of our correction process. Further measurements of this cross section which incorporate much lower laser powers or detailed power dependence studies at each wavelength are therefore indicated. A lower power study is unfortunately complicated by the necessity of normalizing to the much smaller O<sup>+</sup> or O<sub>2</sub><sup>+</sup> cross sections.

Vanderhoff<sup>11</sup> has reported observing a cross section of  $2 \times 10^{-17}$  cm<sup>2</sup> for NONO<sup>+</sup> at 6764 Å, decreasing to  $3 \times 10^{-19}$  cm<sup>2</sup> at 4131 Å. This long wavelength value is consistent with the results of this study. Burke and Wayne<sup>12</sup> have also measured the cross sections for NONO<sup>+</sup> and O<sub>2</sub><sup>+</sup> at shorter wavelengths.

The photodissociation of CO<sub>2</sub>CO<sub>2</sub><sup>+</sup> was also briefly examined. Formation is due to a three-body reaction



with a rate constant<sup>13</sup>  $k = 3.3 \times 10^{-38}$  cm<sup>6</sup>/s. Photodissociation of this ion to produce CO<sub>2</sub><sup>+</sup> was observed with a large cross section throughout the 5300–6300 Å wavelength range. In order to minimize recombination of the CO<sub>2</sub><sup>+</sup> photofragments in the laser interaction region and to facilitate normalization to the CO<sub>2</sub><sup>+</sup> cross section<sup>5</sup> relatively low pressures were maintained in the drift tube (line 5, Table I). Since the diffusion coefficient varies inversely with pressure, this choice of conditions results in a power dependence in the apparent CO<sub>2</sub>CO<sub>2</sub><sup>+</sup> cross section which is even stronger than that observed for NONO<sup>+</sup>. Our model fitting of this dependence at 5900 Å results in a photodissociation cross section of  $2.3 \times 10^{-17}$  cm<sup>2</sup>.

Estimates of the cross section at 5300 and 6300 Å of  $2 \times 10^{-17}$  and  $4 \times 10^{-17}$  cm<sup>2</sup>, respectively, were obtained by employing the model with the same diffusion coefficient used at 5900 Å and neglecting possible variations in the geometric factor  $G$  with wavelength. Changes in  $G$  may reflect changes in the distance  $x$  and thus the diffusion rate  $k_D$ . These results are less certain than those obtained for the other dimer ions, and further studies of this cross section at higher drift tube total pressures and lower laser powers are planned. The CO<sub>2</sub>CO<sub>2</sub><sup>+</sup> photodissociation cross section has been measured by Vestal and Mauclaire.<sup>14</sup> In their tandem quadrupole mass spectrometer the ions traversed the laser interaction region at relatively high energy (20 eV), so diffusion effects were negligible. Their measurements are in agreement with the cross sections obtained in the present work.

The dimer ions may be pictured as pseudohomonuclear diatomics, with the charge equally shared between fragments. A "gerade" bound state and an "ungerade" repulsive excited state will be formed which are coupled by an optical transition, so the large structureless cross sections observed for these ions are not surprising. Similar behavior has been observed in the rare gas dimer ions<sup>15</sup> Ar<sub>2</sub><sup>+</sup>, Kr<sub>2</sub><sup>+</sup>, and Xe<sub>2</sub><sup>+</sup>, and in N<sub>2</sub><sup>+</sup>.<sup>16</sup>

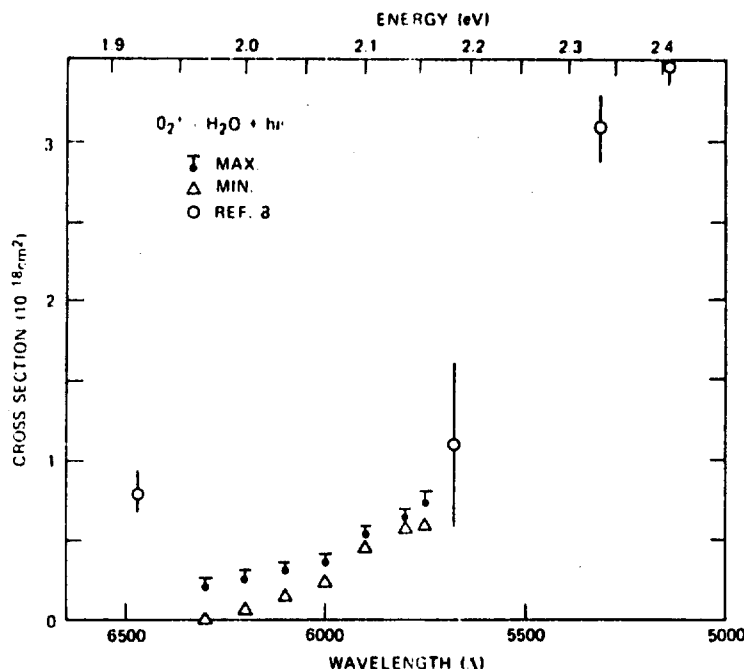


FIG. 3. Wavelength dependence of the  $O_2^+ \cdot H_2O$  photodissociation cross section from 5750 to 6300 Å. The open circles are the data of Ref. 8, taken at high water concentration. The labeled maximum values are those measured at lower water concentration in this study. The minimum values correct these values for the maximum effect of equilibrium reactions with photodissociating  $O_2^+$  on the apparent  $O_2^+ \cdot H_2O$  photodissociation.

#### IV. HYDRATES OF OXYGEN AND NITRIC OXIDE CATIONS

The photodissociation cross section of  $O_2^+ \cdot H_2O$  has been measured over the wavelength range 5750–6300 Å. Under the conditions employed in the drift tube (line 7, Table I) this ion is produced predominately from the reaction of  $O_2^+$  with  $H_2O$ . As shown by the data labeled "maximum values" in Fig. 3 the apparent cross section decreases from  $7.1 \times 10^{-18} \text{ cm}^2$  at 5750 Å to  $2.0 \times 10^{-18} \text{ cm}^2$  at 6300 Å. Over this same wavelength region, however, the photodissociation cross section of  $O_2^+$  increases from  $8 \times 10^{-19}$  to  $1.5 \times 10^{-18} \text{ cm}^2$ . Possible coupling of the photolysis of these two species through the equilibrium reactions



with rate constant<sup>17</sup>  $k_r = 1.5 \times 10^{-9} \text{ cm}^3/\text{s}$  must therefore be considered in determining the photodissociation cross section of  $O_2^+ \cdot H_2O$  at these wavelengths. Since the drift conditions (line 7, Table I) insure the establishment of equilibrium,  $k_r$  can always be calculated from the measured ion intensities and the water concentration. Here,  $k_r$  is  $1.0 \times 10^{-12} \text{ cm}^3/\text{s}$ . Given the known forward rate constant,<sup>9</sup> and using the water concentration in the drift tube of  $2 \times 10^{-4}$  Torr as measured by a residual gas analyzer attached to the apparatus, the calculated mean lifetime of  $O_2^+$  is 60 μs. From the known drift velocity of  $O_2^+$  this corresponds to a mean drift distance of 0.3 cm. Thus, the drift distance from source to detector of 30 cm is sufficient to ensure establishment of an equilibrium between dimer and hydrate. The hydrate concentration is observed to be comparable to that of the dimer in the drift tube, thus

indicating its lifetime is roughly the same as that of  $O_2^+$ . Since the drift distance between the first contact with the laser beam and the extraction aperture is 0.2–0.3 cm, the equilibrium perturbed by the  $O_2^+$  photodissociation will at least partially reassert itself prior to the extraction aperture, and some loss of  $O_2^+ \cdot H_2O$  will be caused by the photodissociation of its parent  $O_2^+$ .

The extent of this effect is uncertain, given our imprecise knowledge of the reaction rates, ion detection efficiencies, laser region geometry, and water concentration. However, even with these uncertainties accurate limits on this effect can be established. The hydrate loss from this source can never exceed the  $O_2^+$  cross section. A lower water concentration allows the reaction of  $O_2^+$  but not  $O_2^+ \cdot H_2O$ . Since the hydrate equilibrium concentration also decreases, there is no net effect on the time required to re-establish equilibrium. Only the oxygen pressure has a large effect on the extent of coupling between the ions.

The largest possible  $O_2^+$  contribution to the apparent hydrate photodissociation occurs at 6300 Å, where the  $O_2^+$  cross section is the largest. The effect will be less at shorter wavelengths because the  $O_2^+$  cross section decreases. Since the apparent  $O_2^+ \cdot H_2O$  cross section begins to increase, real photodissociation must be occurring at wavelengths below 6300 Å.

The maximum  $O_2^+ \cdot H_2O$  cross sections are the values measured directly. The minimum cross sections can be calculated by assuming the entire 6300 Å apparent photodestruction is attributable to the  $O_2^+$  equilibrium. One can then construct a simple kinetic model for the 0.2 cm laser zone and the 0.1 cm final drift zone which

TABLE III. NO<sup>+</sup> cluster ion cross section upper limits (10<sup>-18</sup> cm<sup>2</sup>).

	5500 Å	5800 Å	6200 Å
NO <sup>+</sup> ·H <sub>2</sub> O	≤ 0.03	≤ 0.018	≤ 0.0084
NO <sup>+</sup> ·2H <sub>2</sub> O	≤ 0.005	≤ 0.014	≤ 0.0088
NO <sup>+</sup> ·N <sub>2</sub>	≤ 0.40	...	...
NO <sup>+</sup> ·CO <sub>2</sub>	≤ 0.09	...	...
NO <sup>+</sup> ·N <sub>2</sub> O	...	≤ 0.20	...

incorporates the exchange and photodissociation rates. Then the rate equation for O<sub>2</sub><sup>+</sup>, for example, is

$$\frac{d[\text{O}_2^+]}{dt} = -P[\text{O}_2^+] - k_f[\text{O}_2^+][\text{H}_2\text{O}] + k_r[\text{O}_2^+ \cdot \text{H}_2\text{O}][\text{O}_2], \quad (9)$$

where  $P = \ln(I_0/I)/l$  is the rate constant for photodissociation, which depends on laser power, the cross section, and geometrical factors.

To obtain the minimum O<sub>2</sub><sup>+</sup>·H<sub>2</sub>O cross sections  $P$  for O<sub>2</sub><sup>+</sup> is chosen to obtain the observed photodissociation percentage for that ion, and the water concentration in the calculation is varied until the entire apparent O<sub>2</sub><sup>+</sup>·H<sub>2</sub>O photodissociation at 6300 Å is accounted for by reaction. This fixed the water pressure for the model at 1×10<sup>-4</sup> Torr. Then at other wavelengths  $P$  for O<sub>2</sub><sup>+</sup> is proportionately decreased by the measured decrease in the O<sub>2</sub><sup>+</sup> cross section, and  $P$  for the hydrate increased until the observed apparent hydrate photodestruction at the new wavelength is matched by the model. The ratio of  $P$  values is the ratio of cross sections, and thus the minimum values for the hydrate cross section are established.

The limits on the O<sub>2</sub><sup>+</sup>·H<sub>2</sub>O photodissociation cross sections resulting from these considerations are plotted in Fig. 3. The data labeled maximum values in this figure refer to our uncorrected cross section measurements, while the data labeled minimum values have been corrected for the equilibrium with O<sub>2</sub><sup>+</sup>, as discussed above. A probable threshold near 6200 Å is indicated. The data of Ref. 9 at longer wavelengths indicates a larger cross section than our maximum value. This may result from a larger, uncorrected equilibration with O<sub>2</sub><sup>+</sup>, caused by different geometrical factors. Note, for example, that their cross sections varied with the positioning of the laser relative to the extraction aperture.<sup>9</sup> The larger values measured by Ref. 8 at shorter wavelengths, however, should be relatively unaffected by these reaction effects.

The O<sub>2</sub><sup>+</sup>·H<sub>2</sub>O ion is an important ion in the  $D$  region of the ionosphere,<sup>1</sup> and its confirmed photodissociation should be considered in the chemistry of this region. The existence in the visible of a structureless dissociative state for the weakly bound O<sub>2</sub><sup>+</sup>·H<sub>2</sub>O ion suggests a low-lying unbound charge transfer state O<sub>2</sub><sup>+</sup>·H<sub>2</sub>O<sup>+</sup>, provided the ground state configuration can be viewed as O<sub>2</sub><sup>+</sup>·H<sub>2</sub>O. As Beyer and Vanderhoff point out<sup>8</sup> the failure to observe the H<sub>2</sub>O<sup>+</sup> photofragment does not rule out this hypothesis, since fast charge transfer to O<sub>2</sub> is expected under our experimental conditions.

The ions NO<sup>+</sup>·H<sub>2</sub>O and NO<sup>+</sup>·2H<sub>2</sub>O were formed in 0.40 Torr CO<sub>2</sub> with less than 1% each NO and H<sub>2</sub>O (line 6, Table I). The ions are initially produced from NO<sup>+</sup> by fast three-body reactions



The rate constants for these reactions, which have been measured<sup>9</sup> for the case of N<sub>2</sub> as the third body, are approximately 1.6 and 11×10<sup>-30</sup> cm<sup>3</sup>/s, respectively. Neither ion was observed to dissociate between 5300 and 6200 Å, and limits on the cross sections, generally in the 10<sup>-20</sup> cm<sup>2</sup> range, are given in Table III. Measurements in large partial pressures of NO were purposely avoided, since the equilibrium reactions



with rate constants<sup>9</sup>  $k_f = 1.4 \times 10^{-9}$  cm<sup>3</sup>/s and  $k_r = 9.0 \times 10^{-16}$  cm<sup>3</sup>/s would effectively cause some of the NONO<sup>+</sup> photodissociation to appear as a reduction in the amount of NO<sup>+</sup>·H<sub>2</sub>O when the laser is on. A previous upper limit of 10<sup>-19</sup> cm<sup>2</sup> for NO<sup>+</sup>·H<sub>2</sub>O at 6471 Å has been reported.<sup>11</sup>

## V. CO<sub>2</sub><sup>+</sup>

This ion was formed in 5% O<sub>2</sub>/95% CO<sub>2</sub> (line 8, Table I) by the three-body reaction<sup>13</sup>



The photodissociation cross section of CO<sub>2</sub><sup>+</sup> has been measured at 25 Å intervals between 5300 and 6200 Å. Our results are given by the solid points in Fig. 4 and clearly show a lack of structure in the cross section. Photodissociation cross sections for CO<sub>2</sub><sup>+</sup> have been reported by Beyer and Vanderhoff,<sup>8</sup> and their data, shown as the open circles in Fig. 4, are in excellent agreement with the present results. Above 5800 Å the apparent cross section increased with the addition of more O<sub>2</sub> to the mixture. This is likely the effect of an increased amount of O<sub>2</sub><sup>+</sup>, whose photodissociation becomes equilibrated with CO<sub>2</sub><sup>+</sup>, presumably via the reactions



The measurements presented in Fig. 4 clearly show a threshold near 6200 Å, so such an equilibrium can have no significant effect on the much larger values recorded below 6000 Å. Reaction (14) is presumably the major CO<sub>2</sub><sup>+</sup> production mechanism.

Here CO<sub>2</sub><sup>+</sup> is the major photofragment ion, implying an electronic structure analogous to that proposed for the hydrate O<sub>2</sub><sup>+</sup>·H<sub>2</sub>O. These results suggest the ground state is a cluster ion best described by O<sub>2</sub><sup>+</sup>·CO<sub>2</sub>, with an unbound, excited, charge-transfer state O<sub>2</sub><sup>+</sup>·CO<sub>2</sub><sup>+</sup>. Excitation of this dissociative state is presumably the observed process.

An upper limit to the O<sub>2</sub><sup>+</sup>·CO<sub>2</sub> bond energy can be derived from these measurements, as previously noted in Ref. 8. The threshold appears to be close to 2.00 eV (6200 Å). The observed CO<sub>2</sub><sup>+</sup> product channel, however, exceeds the lowest thermodynamic one by the difference



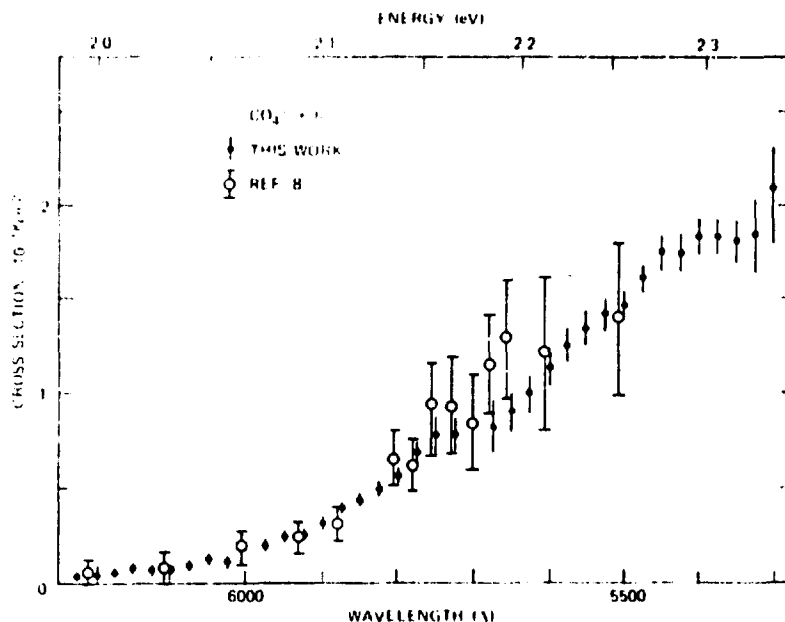
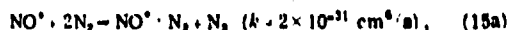


FIG. 4. Photodissociation cross section for  $\text{CO}_2^+$  from 5300 to 5225 Å given by the solid points. The open circles are data from Ref. 8, included for comparison.

between  $\text{CO}_2$  and  $\text{O}_2$  ionization potentials of 1.71 eV. The remaining 0.30 eV is then an upper bound on  $D_0^0(\text{O}_2^+ \cdot \text{CO}_2)$ . Note, however, that an uncertainty of  $\sim 100$  Å in the true position of the threshold for thermal ions introduces an uncertainty of 0.03 eV in this estimate. The estimate also implicitly assumes the  $\text{CO}_2^+$  product channel observed at 5800 Å is the relevant one in the region of the threshold.

#### VI. $\text{NO}^+$ CLUSTER IONS WITH $\text{N}_2$ , $\text{N}_2\text{O}$ , AND $\text{CO}_2$

Several attempts were made to measure the  $\text{NO}^+ \cdot \text{N}_2$  photodissociation cross section. This ion is very weakly bound and difficult to make at 300 K,<sup>18</sup> since a variety of three-body  $\text{NO}^+$  reactions and bimolecular exchange reactions<sup>1</sup> occur, including Reaction (3) and <sup>19,20</sup>



and also



and



In  $\text{N}_2$  (line 0, Table I) with less than 0.5% NO the apparent  $\text{NO}^+ \cdot \text{N}_2$  photodestruction cross section at 5400 Å varied with NO pressure in a way consistent with an equilibrium between  $\text{NONO}^+$  and  $\text{NO}^+ \cdot \text{N}_2$ . Attempts to decrease the  $\text{NONO}^+$  effects by lowering NO below 0.1% only decrease the already small amount of  $\text{NO}^+ \cdot \text{N}_2$  present, and increase the possibility of equilibrium effects with  $\text{N}_2^+$ , which also dissociates<sup>18</sup> and is present in significant quantities. (The abundance of the mass 58 ion relative to that of  $\text{N}_2^+$  is much too large to be identified

as  $^{15}\text{N}_2\text{N}_2^+$ .) Our results set an upper limit on the photodissociation of  $\text{NO}^+ \cdot \text{N}_2$  of  $4 \times 10^{-19} \text{ cm}^2$  at 5400 Å. The actual cross section may well be zero, in view of the equilibrium fit with  $\text{NONO}^+$  and the failure of other mixed  $\text{NO}^+$  clusters to photodissociate.

The validity of the equilibrium model is illustrated by the results for  $\text{NO}^+ \cdot \text{CO}_2$ . In these experiments (line 10, Table I) the fraction of NO in  $\text{CO}_2$  was varied from 10% to 0.01%. The apparent cross sections at 5300 Å are shown in Fig. 5. The relevant exchange reactions are<sup>21</sup>



and



The effect of Reaction (17) is negligible for NO concentrations above 0.1%, while the effect of Reaction (16) is negligible for the 0.01% NO mixture. By measuring the ratio of ion intensities  $\text{NO}^+ \cdot \text{CO}_2 / \text{NONO}^+$  at various NO concentrations it was confirmed that equilibrium exists, with an equilibrium constant  $K_{16} \sim 2 \times 10^{-3}$ . Choosing a model forward rate constant of  $10^{-10} \text{ cm}^3/\text{sec}$  for Reaction (16) the 0.1%-10% NO data can be fit as shown in Fig. 5. A constant model photodissociation rate was used for  $\text{NONO}^+$ , and  $\text{NO}^+ \cdot \text{CO}_2$  was assumed not to photodissociate. The measured equilibrium was used to give  $k_{16} \sim 5 \times 10^{-10} \text{ cm}^3/\text{s}$ . The ratio of the  $\text{NO}^+ \cdot \text{CO}_2$  to  $\text{NONO}^+$  apparent cross sections does not vary from 5300-5800 Å. This is consistent with a zero cross section or a constant, small cross section for  $\text{NO}^+ \cdot \text{CO}_2$ . If the cross section is nonzero, it will be difficult to determine accurately amidst the large reactive transfer

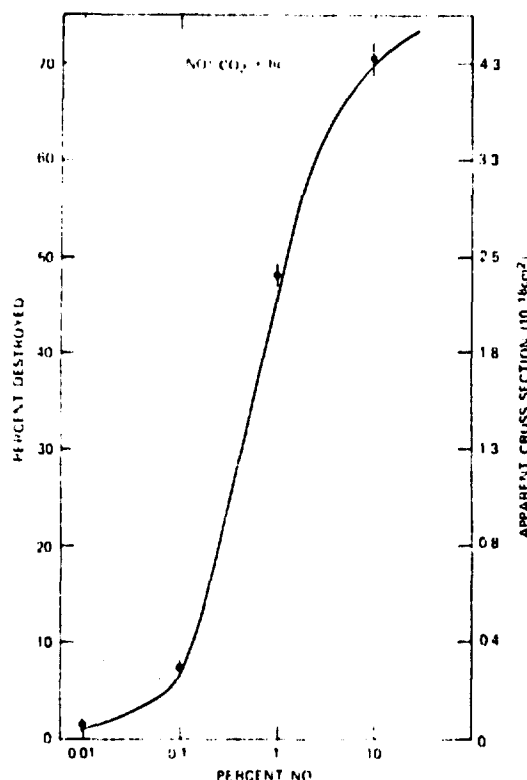


FIG. 5. Effect of the NO mole fraction on the apparent  $\text{NO}^+ \cdot \text{CO}_2$  photodissociation at 5500 Å. The model prediction (solid line) considers the effects of  $\text{NONO}^+$  and  $\text{CO}_2\text{CO}_2^+$  photodissociation on this observed loss (data points), via the equilibrium reactions (16) and (17).

of  $\text{NONO}^+$  photodissociation, due to experimental uncertainties.

An upper limit on the cross section for  $\text{NO}^+ \cdot \text{CO}_2$  may be derived by the model from the 0.01% NO results. The apparent photodestruction can be attributed either to the Reaction (17) equilibrium with a model forward rate constant of  $10^{-11} \text{ cm}^3/\text{s}$  or a true photodissociation cross section of  $6 \times 10^{-20} \text{ cm}^2$ . This is an upper limit, therefore, on the  $\text{NO}^+ \cdot \text{CO}_2$  photodissociation cross section at 5500 Å, although it is likely much smaller throughout the 5300–5650 Å range.

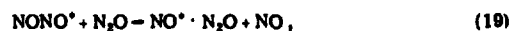
Because copious quantities of  $\text{NO}^+$  and little  $\text{NO}^+ \cdot \text{CO}_2$  are present at 0.01% NO, effects of the three-body reaction



must be investigated here. This reaction, with the reverse of Reaction (17), probably accounts for the bulk of  $\text{NO}^+ \cdot \text{CO}_2$  and  $\text{CO}_2\text{CO}_2^+$  production. Those  $\text{NO}^+ \cdot \text{CO}_2$  ions formed in the postlaser region are not subject to photodissociation, and thus artificially decrease the observed cross section. In adding this process to our kinetic scheme and numerically integrating, the maximum

effect is to increase the cross section limit to  $9 \times 10^{-20} \text{ cm}^2$ .

Reactive effects also dominate attempts to measure the  $\text{NO}^+ \cdot \text{N}_2\text{O}$  cross section in 0.40 Torr  $\text{N}_2\text{O}$  (line 11, Table I) at 5750 Å. The apparent photodestruction of  $\text{NO}^+ \cdot \text{N}_2\text{O}$  increases with decreasing  $E/N$ , when the ions have a longer time to equilibrate with the photodissociating  $\text{NONO}^+$ , which is present in larger quantities. The relevant reactions appear to be



Since we are attempting to fit an  $E/N$  dependence, diffusion effects must be considered, as must the three-body reaction



One effect of diffusion, as previously illustrated, is to cause the apparent  $\text{NONO}^+$  cross section to vary with  $E/N$  (drift time). To accommodate this properly the model  $\text{NONO}^+$  photodissociation rate was permitted to vary with  $E/N$  in a linear fashion as shown in Fig. 2, to fit the observed loss. Constant values were chosen for  $k_{10}$  and for the  $\text{NO}^+ \cdot \text{N}_2\text{O}$  photodissociation cross section, to obtain the best fit of data at all  $E/N$ . Once again equilibrium was assumed between the two ions to calculate  $k_{20}$ . The  $\text{NO}^+ \cdot \text{N}_2\text{O}$  cross section is the ratio of model ion photodissociation rates times the observed  $\text{NONO}^+$  cross section. The  $k_{10}$  and  $\sigma(\text{NO}^+ \cdot \text{N}_2\text{O})$ , derived from the fit of the model to the data and applicable at both 5750 and 5800 Å, are  $3.5 \times 10^{-13} \text{ cm}^3/\text{s}$  and  $2.0 \times 10^{-19} \text{ cm}^2$ , respectively. The data and fit are shown in Fig. 6.

The rate constant of Reaction (21) is unknown, but its qualitative effect can be estimated. Ions are slowest at 5 Td, and a great fraction of the  $\text{NO}^+ \cdot \text{N}_2\text{O}$  ions is created by Reaction (21) in the postlaser region, leading to an underestimated cross section. When corrected for this effect of Reaction (21) the  $E/N$  data is even more nonlinear. A proper fit now requires an increase in the equilibration rate constant  $k_{10}$ , and a decrease in the model  $\text{NO}^+ \cdot \text{N}_2\text{O}$  photodestruction cross section. Furthermore, it is possible that more complicated diffusion effects introduce added uncertainty into the 5 Td results. It is then possible to fit the remaining data with a larger  $k_{10}$  and no  $\text{NO}^+ \cdot \text{N}_2\text{O}$  photodissociation. Thus, the value of  $2.0 \times 10^{-19} \text{ cm}^2$  is an upper limit to the true  $\text{NO}^+ \cdot \text{N}_2\text{O}$  cross section, which may be zero at these wavelengths.

Note that in contrast to the asymmetric  $\text{O}_2^+$  cluster ions those of  $\text{NO}^+$  do not have appreciable cross sections at the wavelengths studied here. This suggests the transition to a repulsive charge-transfer state (e.g.,  $\text{H}_2\text{O}^+ \cdot \text{NO}$ ) lies at higher energies due to the much lower NO ionization potential. One would not expect the well depth of the bound state or the steepness and nature of the repulsive state to be very different from the asymmetric  $\text{O}_2^+$  cluster ions.

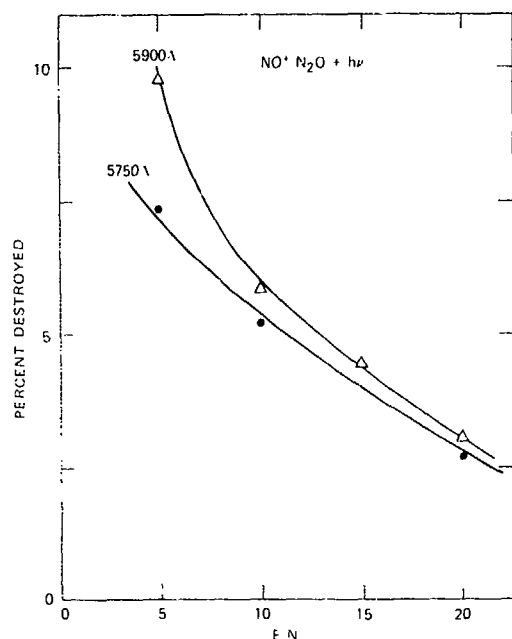


FIG. 6. Variation of the apparent  $\text{NO}^+\cdot\text{N}_2\text{O}$  photodissociation as a function of  $E/N$  at two wavelengths. The model fits shown by the solid lines illustrate the effect of  $\text{NONO}^+$  photodissociation through Reactions (19) and (20).

## VII. HYDRONIUM IONS

The water based ions  $\text{H}_3\text{O}^+(\text{H}_2\text{O})_n$  are among the most abundant of the  $D$  region cluster ions.<sup>1</sup> Good *et al.*,<sup>20</sup> have outlined the complicated reaction mechanism for production of these ions. The photodissociation cross sections for the first three ions of the series have been measured in this study between 5300 and 6200 Å. No statistically significant photodissociation was observed, but upper limits were set on the cross sections, and are given in Table IV. These limits are generally an order of magnitude below those set by Henderson and Schmeltekopf,<sup>22</sup> and are also below the limits set by Beyer and Vanderhoff<sup>6</sup> to the red and blue of our wavelength region. With the drift tube operated with less than 1% water in  $\text{O}_2$  (line 12, Table I) little  $\text{H}_3\text{O}^+(\text{H}_2\text{O})_3$  was observed. Thus, the cross section limits are not underestimated due to possible photofragments from higher hydrates.

## VIII. SUMMARY

Our measurements on the photodissociation cross sections for the ions  $\text{O}_4^+$ ,  $\text{CO}_2\text{CO}^+$ ,  $\text{NONO}^+$ ,  $\text{O}_2^+\cdot\text{H}_2\text{O}$ ,  $\text{CO}^+\cdot\text{H}_2\text{O}$ ,  $\text{NO}^+\cdot\text{N}_2$ ,  $\text{NO}^+\cdot\text{N}_2\text{O}$ ,  $\text{NO}^+\cdot\text{CO}_2$ ,  $\text{H}_3\text{O}^+$ ,  $\text{H}_3\text{O}^+\cdot\text{H}_2\text{O}$ , and  $\text{H}_3\text{O}^+(\text{H}_2\text{O})_2$  are summarized in Figs. 1-3, and 4 and in Tables II-IV. The dimer ions have large cross sections, the asymmetric  $\text{O}_2^+$  clusters have thresholds near 6200 Å, and the hydronium ion and asymmetric  $\text{NO}^+$  clusters do not appear to photodissociate. These ions generally exhibit the photodissociation characteristics of pseudodiatomics. In contrast to  $\text{CO}_2^+$  the

TABLE IV. Hydrate cross section upper limits ( $10^{-18} \text{ cm}^2$ ).

$n =$	$\text{H}_3\text{O}^+(\text{H}_2\text{O})_n$		
	0	1	2
5300 Å	$\leq 0.027$	$\leq 0.027$	$\leq 0.063$
5500 Å	$\leq 0.047$	$\leq 0.047$	$\leq 0.092$
5800 Å	$\leq 0.039$	$\leq 0.032$	$\leq 0.054$
6200 Å	$\leq 0.023$	$\leq 0.031$	$\leq 0.101$

upper states all appear to be repulsive, and the cross sections show no structure. Finally, in demonstrating the effects of diffusion and equilibria this work has shown the importance of examining the chemistry of the experimental system when photodissociation measurements are made in moderate gas pressures. Refinements of the modeling techniques used here could result in determinations of ion-molecule reaction rates and equilibrium constants, particularly in cases where an ion which is known not to photodissociate is in equilibrium with an ion undergoing photodissociation.

- <sup>1</sup>J. L. Thomas, *Radiat. Sci.*, **9**, 121 (1974); E. E. Ferguson and F. E. Fehsenfeld, *J. Geophys. Res.*, **74**, 5713 (1969); J. M. Heimerl, J. A. Vanderhoff, L. J. Puckett, and F. E. Niles, BRL Rep. 7570, Aberdeen Proving Ground, MD (1972); and EOS Trans., AGU **52**, 870 (1971); F. E. Niles, J. M. Heimerl, and C. W. Keller, EOS Trans., AGU **53**, 456 (1972); R. S. Narcisi, A. D. Bailey, L. E. Wlodyka, and C. R. Philbrick, *J. Atmos. Terr. Phys.*, **33**, 1117 (1971); D. Krankowsky, F. Arnold, H. Wider, J. Kissel, and J. Zahringer, *Radio Sci.*, **7**, 93 (1972); J. N. Rowe, A. P. Mitra, A. J. Ferraro, and H. S. Lee, *J. Atmos. Terr. Phys.*, **36**, 755 (1974).
- <sup>2</sup>K. G. Spears, *J. Chem. Phys.*, **57**, 1850 (1972).
- <sup>3</sup>C. E. Busch and K. R. Wilson, *J. Chem. Phys.*, **56**, 3626 (1972); J. T. Moseley, P. C. Cosby, and J. R. Peterson, *J. Chem. Phys.*, **65**, 2312 (1976); J. T. Moseley, M. Tadjeddine, J. Durup, J. B. Ozanne, C. Pernot, and A. Tabche, *Phys. Rev. Lett.*, **37**, 891 (1976).
- <sup>4</sup>P. C. Cosby, R. A. Bennett, J. R. Peterson, and J. T. Moseley, *J. Chem. Phys.*, **63**, 1612 (1975).
- <sup>5</sup>P. C. Cosby, J. H. Ling, J. T. Peterson, and J. T. Moseley, *J. Chem. Phys.*, **65**, 5267 (1976); D. S. Burch, S. J. Smith, and L. M. Branscomb, *Phys. Rev.*, **112**, 171 (1958).
- <sup>6</sup>E. W. McDaniel, *Collision Phenomena in Ionized Gases* (Wiley, New York, 1964), p. 494.
- <sup>7</sup>D. A. Darden, P. Kebarle, and A. Good, *J. Chem. Phys.*, **50**, 805 (1969).
- <sup>8</sup>H. A. Beyer and J. A. Vanderhoff, *J. Chem. Phys.*, **65**, 2313 (1976).
- <sup>9</sup>J. L. Puckett and M. W. Teague, *J. Chem. Phys.*, **54**, 2654 (1971).
- <sup>10</sup>H. W. Ellis, R. Y. Pai, F. W. McDaniel, E. A. Mason, and L. A. Viehland, *At. Data Nucl. Data Tables*, **17**, 177 (1976).
- <sup>11</sup>J. A. Vanderhoff, Abstracts of Twenty-ninth Annual Gaseous Electronics Conference, Paper IA2, 1976; *J. Chem. Phys.*, **67**, 2332 (1977).
- <sup>12</sup>R. R. Burke and R. P. Wayne, *Int. J. Mass Spectrom. Ion Phys.*, (in press).
- <sup>13</sup>L. W. Steele and R. Gordon, Jr., *J. Res. Natl. Bur. Stand. Sect. A*, **78**, 315 (1974).
- <sup>14</sup>M. L. Vestal and G. H. Maclaurin, *Chem. Phys. Lett.*, **43**, 499 (1976).
- <sup>15</sup>T. M. Miller, J. H. Ling, R. P. Saxon, and J. T. Moseley, *Phys. Rev. A*, **13**, 2171 (1976).
- <sup>16</sup>T. M. Miller, J. L. Heldrich, and J. T. Moseley, IX

- ICPEAC *Abstracts of Papers* (University of Washington, Seattle, 1975), p. 7.
- <sup>17</sup>C. J. Howard, V. M. Bierbaum, H. W. Rundle, and F. Kaufman, *J. Chem. Phys.* **57**, 3491 (1972).
- <sup>18</sup>D. L. Turner and D. C. Conway, *J. Chem. Phys.* **65**, 3944 (1976).
- <sup>19</sup>J. M. Helmerl and J. A. Vanderhoff, *J. Chem. Phys.* **60**, 4362 (1974).
- <sup>20</sup>A. Good, D. A. Durden, and P. Kebarle, *J. Chem. Phys.* **52**, 212, 222 (1970).
- <sup>21</sup>D. B. Dunkin, F. C. Fehsenfeld, A. L. Schmeltekopf, and E. E. Ferguson, *J. Chem. Phys.* **54**, 3817 (1971).
- <sup>22</sup>W. R. Henderson and A. L. Schmeltekopf, *J. Chem. Phys.* **57**, 4502 (1972).

# Laser-ion coaxial beams spectrometer

B. A. Huber,<sup>a)</sup> T. M. Miller, P. C. Cosby, H. D. Zeman,<sup>b)</sup> R. L. Leon, J. T. Moseley, and J. R. Peterson

*Molecular Physics Center, SRI International, Menlo Park, California 94025*

(Received 7 June 1977; in final form, 30 June 1977)

An apparatus has been constructed to provide laser excitation of ion beams in both coaxial and crossed configurations. The coaxial geometry provides very high sensitivity and nearly Doppler-free wavelength resolution for spectroscopic measurements, and allows the use of the Doppler shift to "tune" the wavelength. A novel transverse quadrupole electric field arrangement is used to deflect the ion beam into and out of the laser beam axis. The ion beam is highly collimated and a high-resolution 180° electrostatic analyzer is used for photofragment energy analysis. The apparatus has demonstrated a resolution of better than 10 meV for normal photofragment spectroscopy and 0.001 meV for coaxial beams photofragment spectroscopy using a single-mode laser. While providing these high resolutions the apparatus has an overall sensitivity several orders of magnitude greater than conventional ones.

## I. INTRODUCTION

In recent years, several research efforts have been initiated to study the photodissociation of molecular ions in beams. Von Busch and Dunn<sup>1</sup> first examined the wavelength dependence of H<sup>+</sup> production from H<sub>2</sub><sup>+</sup>, using an Xe arc lamp and monochromator, in a crossed-beams arrangement. Subsequently, Ozenne, Pham, and Durup at Orsay,<sup>2</sup> and van Asselt, Maas, and Los in Amsterdam<sup>3</sup> measured the energy spectra of the dissociation fragment ions using fixed-frequency lasers in a crossed-beams geometry. Such photofragment spectroscopy studies yield information on the potential energy curves, on bond energies, on the population of vibrational levels of the parent ions, and on the energy partitioning among the dissociation fragments of polyatomic ions. Recently the group at Orsay<sup>4</sup> showed that a modification of this technique, using tunable dye lasers at wavelengths near the dissociation threshold, can be used to obtain high-resolution spectroscopic data on molecular ions via transitions to predissociating states. In all of these experiments the laser beam intersected the ion beam orthogonally, where there is no Doppler shift (although a Doppler spread exists due to the angular divergence in the ion beam).

Experiments have also made use of Doppler shifts of single-frequency laser lines to excite fast beams. In some cases,<sup>5</sup> laser lines have been shifted by varying the laser-fast beam intersection angle, and in others the Doppler frequencies were "velocity tuned" to the absorption frequency by varying the particle beam energy, with the laser inclined at a small angle<sup>6</sup> or parallel<sup>7-9</sup> to the fast beam. These latter experiments also benefited from a very effective narrowing of the Doppler line profile that can occur in coaxial laser-fast beam arrangements, as is discussed below.

We describe here an apparatus designed to accommodate both laser excitation and dissociation studies of ions in both coaxial (merged beam) and crossed-beams configurations. A novel and efficient ion beam deflec-

tion system is used to merge the ion beam with the laser axis in the coaxial case. The apparatus can operate with the ion beam vacuum chamber in the resonant cavity of the laser for increased photon flux in both configurations. The coaxial configuration offers a much longer (10<sup>2</sup>–10<sup>3</sup> times) interaction path than the crossed-beams arrangement; thus, the apparatus has a much greater ultimate sensitivity than previous ion photodissociation apparatuses. A high-resolution ( $\Delta E/E \approx 3 \times 10^{-3}$ ) energy analyzer, used for ion photofragment energy measurements, can provide a resolution of 10<sup>-4</sup> when combined with deceleration of the ions. The apparatus is a versatile and sensitive tool for high-resolution photofragment and optical spectroscopy studies on ion beams.

## II. DESCRIPTION OF THE APPARATUS

### A. Basic requirements and general description

Because, among other uses, the apparatus is intended for photofragment energy measurements, the ion beams must be well collimated and have low-energy spread and yet must have sufficient intensity to perform the desired experiments. The energy and angular resolution required for photofragment spectroscopy can be estimated as follows.

The velocity diagram in Fig. 1 defines various kinematic parameters in a dissociation event. If a molecule moving with initial kinetic energy  $E_0$  and speed  $v_0$  in the laboratory frame dissociates into two fragments of mass  $m_1$  and  $m_2$ , with total center of mass (c.m.) kinetic energy release  $W$ , the laboratory energy of  $m_1$ , ejected at c.m. angle  $\varphi$ , or laboratory angle  $\theta$ , with respect to the beam direction is

$$E_1 = \frac{m_1 m_2}{m_2 + m_1} \left[ \frac{E_0}{m_1} + 2 \left( \frac{E_0 W}{m_1 m_2} \right)^{1/2} \cos \varphi + \frac{W}{m_1} \right].$$

To simplify matters, we consider the case of a homonuclear diatomic molecule ( $m_1 = m_2$ ); then

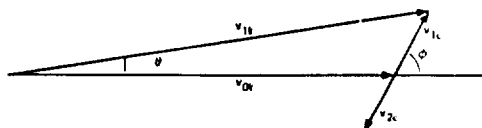


FIG. 1. Velocity diagram for a photodissociation event.  $\theta$  and  $\varphi$  are the laboratory and center-of-mass angles, respectively, for ejection of a photofragment with respect to the laboratory velocity  $v_0$ . The center-of-mass velocities of the two photofragments are  $v_{1c}$  and  $v_{2c}$ .

$$E_1 = \frac{1}{2}E_0[1 + 2(W/E_0)^{1/2} \cos\varphi + W/E_0]. \quad (2)$$

The term  $W/E_0$  is always small ( $\sim 10^{-3}$ ) in our experiments, and we shall neglect it in determining the design parameters of the apparatus. Thus

$$E_1 = \frac{1}{2}E_0[1 + 2(W/E_0)^{1/2} \cos\varphi]. \quad (3)$$

Requirements on energy resolution of the apparatus can be estimated by noting that for variations in  $W$  only,

$$\Delta E_1 = \frac{\partial E_1}{\partial W} \Delta W = \frac{1}{2} \left( \frac{E_0}{W} \right)^{1/2} \cos\varphi \Delta W. \quad (4)$$

As a typical example, let  $E_0 = 3000$  eV,  $W = 1$  eV, and  $\varphi = 0$ . If the energy difference between the vibrational levels in the parent ion is  $400 \text{ cm}^{-1}$  (a reasonably small value), then in order to distinguish between ions dissociating from adjacent levels we must resolve  $\Delta W = 0.05$  eV. The ions dissociating in the forward direction ( $\varphi = 0$ ) would be separated by a laboratory energy  $\Delta E_1 = 1.4$  eV at  $E_1 \sim 1555$  eV, and a resolution of  $\Delta E/E \sim 10^{-3}$  would be required.

The effective energy resolution is decreased as the range of  $\theta$  near  $0^\circ$  accepted by the energy analyzer is increased, allowing ions with larger values of  $\varphi$  to be detected. To estimate the required angular collimation,

let the laboratory energy of fragment ion A, dissociated at  $\varphi = 0$  and  $W = W_0$ , just equal that of another ion B, at  $\varphi = \varphi_{\max}$  (the maximum  $\varphi$  allowed by collimation) and  $W = W_0 + \Delta W$ . From Eq. (3) these conditions establish

$$\varphi_{\max} = \cos^{-1}[W/(W + \Delta W)]^{1/2}. \quad (5)$$

The relationship between  $\theta$  and  $\varphi$  can be seen from Fig. 1 to be

$$\begin{aligned} \theta &= \tan^{-1}[v_{1c} \sin\varphi / (v_{0l} + v_{1c} \cos\varphi)] \\ &= \tan^{-1}[W^{1/2} \sin\varphi / (E_0^{1/2} + W^{1/2} \cos\varphi)] \\ &\approx (W/E_0)^{1/2} \sin\varphi. \end{aligned} \quad (6)$$

The approximation in Eq. (6) is made by dropping the second term in the denominator because  $W \ll E_0$ , and by noting that  $\theta \ll 1$ . The required collimation,  $\theta_{\max}$ , can be obtained from Eq. (6) by letting  $\varphi = \varphi_{\max}$  obtained from Eq. (5). Again, for the case  $E_0 = 3000$  eV,  $W = 1$  eV, and  $\Delta W = 0.05$  eV, we find from Eq. (5) that  $\varphi_{\max} = 0.22$  rad and  $\theta_{\max} = 4.0 \times 10^{-3}$  rad. In order to permit the actual resolution of vibrational levels separated by  $0.5$  eV, we estimate the required angular definition by letting  $\Delta W' = 0.02$  eV, less than half that of the vibrational spacing. This value sets  $\varphi_{\max} = 0.14$  rad and  $\theta_{\max} = 2.5 \times 10^{-3}$  rad. The resolution of the apparatus is actually about  $2 \times 10^{-3}$  rad.

A diagram of the apparatus is shown in Fig. 2. Ions are extracted from an ion source (described below), focused, mass selected, and enter the main collimating drift space which is defined by two 2-mm-diam apertures A2 and A3 separated by 1 m. Sets of vertical and horizontal deflection plates are placed at several appropriate positions along the beam path.

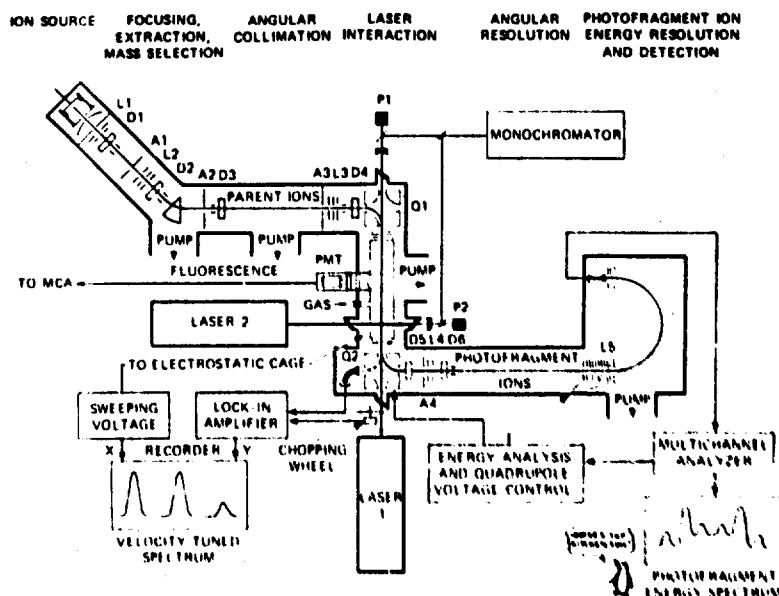


FIG. 2. Schematic of the coaxial beams spectrometer. Ion beam lenses are designated by L, deflectors by D, apertures by A, laser power meters by P, and the quadrupoles by Q.

The collimated ion beam is next deflected 90° and into the laser beam by an electric quadrupole field whose axis is perpendicular to the ion beam. These quadrupole deflectors<sup>10</sup> have exceptionally good ion optical properties as well as a very useful physical configuration for coaxial laser-ion beam experiments. After traversing a 50-cm drift length, the beam (or the desired photofragment sample) is further deflected 90°, parallel to its original direction, by a second electric quadrupole. The potentials on the second deflector are set to direct either the desired fragment ions or the main beam along the final drift path. This path is 1.3 m long and collimation to  $\sim 2.5 \times 10^{-3}$  rad is obtained from a 2-mm entrance aperture to the deceleration lens that precedes the energy analyzer.

After energy analysis, the ions are detected by a Channeltron electron multiplier and the resulting pulse signals are counted in a multichannel scaler whose channels are advanced synchronously with the voltage in the energy analyzer so that a spectrum of the dissociation fragment ions is stored in the scaler for eventual readout to a CRT, recorder, or off-line computer.

The laser beam can be placed either coaxially with the ion beam in the interaction region, or at 90°, depending on the polarization requirements, and the interaction chamber can be operated intracavity with the laser. Brewster window ports in the chamber walls minimize the power loss.

## B. Ion source

For many of the anticipated photodissociation and spectroscopic studies on molecular ions, it is important to have an ion source capable of operating at relatively high pressures so that ions can be formed from three-body reactions (for complex and rare-gas molecular ions); also it should be possible to form ions that are not too vibrationally or rotationally hot. For these purposes we have chosen a cold-cathode discharge source based on a design of Lange, Huber, and Wiesemann.<sup>11</sup> However, we use a hollow cathode instead of their planar geometry, in order to achieve a quiet discharge and to improve the lifetime of the source. The source operates at pressures between 0.1 and 1 Torr. The cathode-anode spacing can be varied and optimized for maximum output. The ions are extracted from a 0.6-mm aperture in the anode. The anode and extraction lens are shaped to form a planar Pierce system to minimize space charge effects. For ions formed by direct electron impact ( $\text{Ar}^+$ ,  $\text{O}_2^+$ ,  $\text{O}^+$ , etc.), the extracted ion current behind the extraction lens is in the range of  $10^{-6}$ – $10^{-7}$  A. Ions formed from three-body or secondary reactions such as  $\text{Ar}_2^+$  may be 100 times less abundant. The width of the kinetic energy distribution was measured to be as small as 0.6 eV for  $\text{Ar}_2^+$  ions, and it was found to depend on source pressure and cathode-anode potential. For  $\text{O}_2^+$  formed at low pressure under conditions that maximize  $\text{O}_2^+(^4\Pi_u)$  production, the energy spread was found to be  $\sim 3$  eV.

## C. Ion optics

As mentioned above, the experiment requires a mass selected ion beam with an angular divergence of about 2 mrad to obtain adequate energy resolution and a beam diameter close to 2 or 3 mm to maximize overlap with the laser. In order to satisfy these conditions without large losses in beam intensity we deflect the beam through 45° using a magnetic sector with equal entrance and exit angles of 14.38° (between ion beam and the perpendicular to the pole faces). These angles were chosen<sup>12</sup> to achieve equal focusing properties in the bending and in the nonbending planes. Calculations of the ion trajectories, taking into account the effect of the extended fringing field, revealed a distance of 26.88 cm between the focal point and the entrance face of the magnet for point-to-parallel focusing.

In order to obtain a well-collimated ion beam beyond the magnet, the ion optics between the source and the magnet were designed so that the extraction region can be imaged at the focal point of the magnet. The ion optics consist of two einzel lenses separated by a small limiting aperture A1 (Fig. 2). The geometry of the einzel lenses was chosen to minimize aberration effects; the focusing properties were computed using standard matrix methods.<sup>13</sup> The first lens focuses the extracted ion beam onto the aperture and the second lens forms a virtual image at the focal point. The 2-mm apertures A2 and A3 in the drift region following the magnet finally define the ion beam with a maximum angular divergence of 2 mrad. Using the calculated potentials for the einzel lenses (optimized within 10%) we found a 30% loss in ion beam intensity at each of these apertures, resulting in usable ion currents between  $1 \times 10^{-8}$  and  $3 \times 10^{-10}$  A for  $\text{O}_2^+$  and  $\text{Ar}_2^+$  ions, respectively.

The primary function of the magnet is to provide mass selection for the ion beam. The ions are deflected through an angle of about 45°. From purely geometrical considerations, an angular collimation of  $2 \times 10^{-3}$  in the beam will give a mass resolution  $\Delta m/m$  of about  $5.6 \times 10^{-3}$ . This is twice the observed value of about  $2.8 \times 10^{-3}$  FWHM obtained in a  $\text{Kr}_2^+$  mass spectrum; thus the effective angular collimation must actually approach  $1 \times 10^{-3}$ .

There is also an energy selectivity associated with the magnetic deflection of a single mass. The relative energy selectivity  $\Delta E/E$  should have the same value as the observed  $\Delta m/m$ , so would be expected to be about  $3 \times 10^{-3}$ . This provides a predicted window of about 9-eV FWHM at 3000 eV, which does not affect the positive ion beams, whose natural energy spreads are much less. For negative ion beams, whose energy widths may exceed 10 eV, a reduction in the size of A1 and A3 can be used to limit the width of the energies transmitted to the interaction region.

For those cases where a higher ion current is needed and the high angular resolution is not necessary, two additional einzel lenses are installed before the first and after the second quadrupole deflector. Thus, a focal

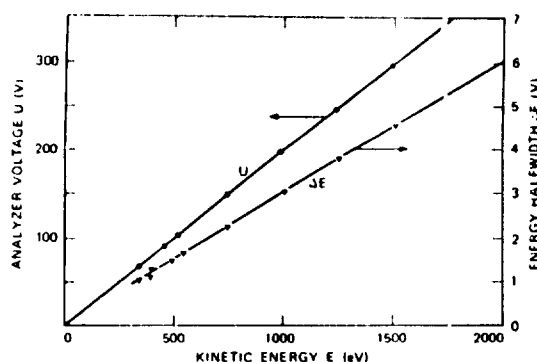


FIG. 3. Energy analyzer test data. Potential  $U$  between analyzer plates versus transmitted energy  $E$ —dots. Energy width  $\Delta E$  of analyzer versus  $E$ —triangles.

point of the ion beam can be formed in the interaction region between the two bending units.

#### D. Energy analysis

The relative energy resolution  $\Delta E/E$  necessary for photofragment spectroscopy is about  $(2-3) \times 10^{-4}$ . In the experiment this value is obtained by using a hemispherical  $180^\circ$  electrostatic analyzer combined with a deceleration system. The kinetic energy of the photofragments is first reduced by a factor of 10 without large intensity loss so that the resolution of the analyzer itself has to be only about  $2 \times 10^{-3}$ .

The deceleration system is formed from the first half of a filter lens.<sup>14</sup> It consists of 13 plates with 3-mm apertures, each plate separated by 3 mm. The ion kinetic energy is reduced in a parabolic electric field<sup>14</sup> (achieved with a resistor divider chain) by a factor of 10, accompanied by ion losses of only about 30%–60%. The exit of the deceleration system and the entrance of the energy analyzer are connected by an einzel lens in order to collimate the slightly diverging beam into the entrance aperture of the analyzer.

The  $180^\circ$  hemispherical electrostatic analyzer used for the final energy analysis has a median radius of 150 mm and a gap distance of 15 mm. The width of the two electrodes is 60 mm and the sides of the gap are shielded by two "Matsuda" plates,<sup>15</sup> the potential of which can be adjusted with respect to the center potential. This type of analyzer was chosen rather than a  $127^\circ$  cylindrical analyzer because of the higher energy dispersion and the focusing properties in both planes.

The voltage  $U$  between the two electrodes and the kinetic energy  $E$  of the ions are related by the following equation<sup>16</sup>:

$$U = 2r_0(r_1 - r_2)E/(r_1r_2) = cE, \quad (7)$$

where  $r_1, r_2$ , and  $r_0$  are the radii of the outer and inner electrodes and the central trajectory, respectively. For a gap distance of 15 mm and  $r_0 = 15$  mm, the analyzer constant  $c$  was calculated to be 0.2005. This value agrees with an experimental determination from a least-squares

fit to the data in Fig. 3, which shows the results of an experimental check of Eq. (7). In order to obtain the same potential for the central trajectory as for the entrance and exit apertures, the potentials of the inner and outer electrodes had to be asymmetric by 5% with respect to central potential. The optical properties of the analyzer, the fringing field effects and the image aberrations, which limit the resolving power, were calculated to second order using the matrices given in Ref. 16. For entrance and exit slits of 1-mm width the calculated<sup>16</sup> resolution of the analyzer was  $6.67 \times 10^{-3}$ . In the experiment we measured the half-width of the primary beam for different kinetic ion energies. The result is also shown in Fig. 3. The linear increase at the energies of these data is due to the finite energy resolution of the analyzer; at lower energies the data would approach a constant value of  $\Delta E$  of about 0.6 eV, which was previously found to be characteristic of this type of ion source. From the slope of the curve we obtain a resolution of  $3.0 \times 10^{-3}$ . Thus the overall resolution of the detection unit with a factor of 10 deceleration is  $3.0 \times 10^{-4}$ . Better resolution is, of course, possible if the entrance and exit slits are narrower or if greater deceleration is used. However, since the energy half-width of the primary ion beam is about 1 eV, the present geometry is adequate for ion transmission energies of up to 200 eV (after deceleration).

The photofragments exiting the energy analyzer are accelerated again to about 3 keV before entering the Channeltron detector. The pulses are normalized in a preamplifier and accumulated in a multichannel scaler. The photofragment kinetic energy spectrum is obtained by setting the hemispherical analyzer voltages for a fixed ion transmission energy (typically 200–300 eV) and linearly varying the voltage applied to the deceleration lens system over the desired range of photofragment energies. The sweep of the deceleration voltage is generated by a D–A converter/high voltage op-amp combination which is driven by the channel address of the multichannel scaler. Thus, the spectra are obtained with constant transmission energy and energy resolution, and nearly constant transmission efficiency. Since the quadrupole benders are also weakly energy selective (energetic window 40 eV at 1500 eV), the potentials on the second quadrupole must also be changed proportionally to the change in detected photofragment energy. If the einzel lens E5 is used, its voltage must be scanned in a similar manner.

#### E. Quadrupole beam deflectors

The deflection systems that bend the ion beam into and out of the laser beams are electrostatic quadrupoles oriented perpendicularly to the bending plane, a novel ion optical arrangement,<sup>10</sup> which is very well suited for this use. It permits an ion beam to merge coaxially with a laser beam without either the use of cumbersome magnets or the more conventional types of electrostatic deflection electrodes which would usually require some



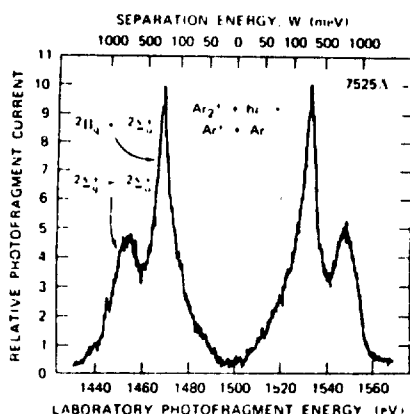


FIG. 4. Photofragment energy spectrum for  $\text{Ar}_2^+ + h\nu \rightarrow \text{Ar}^+ + \text{Ar}$  at 7525 Å. The lower energy scale gives the laboratory photofragment energy, which is directly measured; the upper scale gives the total separation energy determined as discussed in the text.

form of opening to be placed in one of the electrodes to afford passage of the laser beam at the expense of field homogeneity. The capability of viewing the ion beam axis before and after deflection greatly eases alignment procedures. Moreover, the quadrupole deflectors are quite achromatic, creating little distortion in the ion beam after it has been bent through 90°. Ions on one side of the beam in the plane of deflection are switched to the opposite side after passage through the quadrupole, but the angular collimation of the beam is essentially unchanged even for a relatively large energy dispersion (10%). Edge effects due to fringing fields at the entrance and exits of the quadrupoles are corrected with shim electrodes as described in Ref. 10. In tests of this apparatus with a 3-keV ion beam whose energy spread was about 1 eV, essentially all of the beam that had passed through the two collimating apertures A2 and A3 (2-mm diam separated by 1 m) also passed through a 3-mm aperture at the end of the 33-cm drift space following the first 90° deflection.

The energy dispersion of a quadrupole deflector is about 85% of that of a conventional 127° energy analyzer of equal angular aberration,<sup>10</sup> and is manifested in a displacement of the ion trajectories in the bending plane, rather than an angular dispersion, so that a long coaxial drift path following the first deflection can be accommodated without loss of overlap of the ion beam with the laser. The absence of angular dispersion due to the benders also permits a high degree of angular resolution without loss of signal at the energy analyzer and permits a much higher resolution of the ion dissociation fragment energy spectra than has been possible in previous experiments.

As the energies of the fragment ions are scanned by the 180° energy analyzer, the potentials on the second quadrupoles are swept so that fragment ions of the proper energy are directed onto the center of the entrance aperture of the energy analyzer. The quadrupole voltage is approximately 0.7 times the kinetic energy (eV) of the transmitted ions.<sup>10</sup>

### III. PROPERTIES OF THE APPARATUS

The apparatus can accommodate laser-ion beam studies in both coaxial and 90° crossed-beams geometries. In each case, the ion fragments ejected at angles near  $\theta = 0$  or 180° are observed along the beam axis at the lab angle  $\theta_1 = 0 \pm 0.001$  ( $\Delta\theta \sim 2 \times 10^{-3}$  rad). Proper adjustment of the second quadrupole potentials is required to assure that  $\theta = 0$ ; otherwise the values of  $W$  deduced from Eq. (2), with  $\theta = 0$  (or  $\pi$ ), will be incorrect (and will always be low). This complication is a necessary by-product of the coaxial geometry which requires deflection of the dissociated ions before they are energy analyzed, and did not exist in earlier experiments. However, this alignment problem is easily solved and has presented no real drawback to the method.

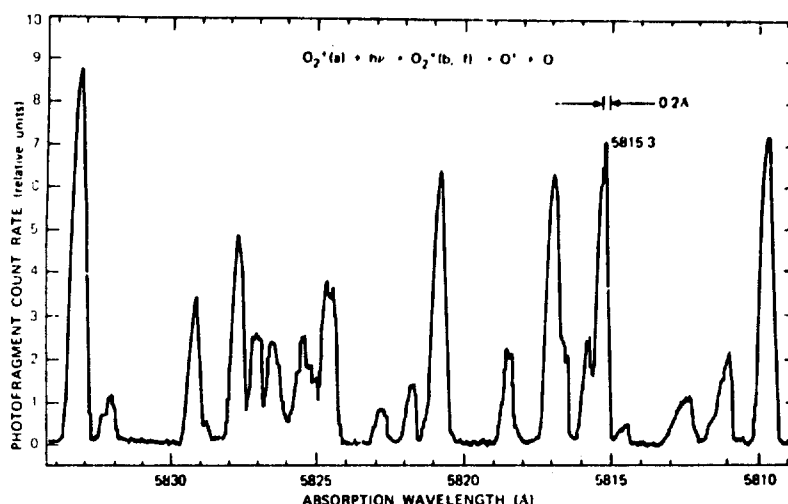
#### A. Coaxial laser-ion beam configuration

The coaxial configuration permits a large interaction volume; the laser and ion beams are merged over a 33-cm length. Since the laser beam is usually about 2 mm in diameter, the interaction volume is 100–200 times larger than that afforded by the conventional crossed-beams geometry, and the resulting sensitivity of the apparatus is similarly increased. However, since the laser polarization is always at right angles to the ion velocities, this advantage is fully effective only for "perpendicular" transitions, where the fragment ions are ejected primarily perpendicularly to the laser polarization, and thus in the direction of motion of the parent ion beam ( $\theta = 0$  or  $\pi$ ) for dissociations near the energetic threshold ( $W \sim 0$ ), or for excitations that do not result in dissociation.

A typical spectrum for the reaction  $\text{Ar}_2^+(^2\Sigma_u^+) + h\nu \rightarrow \text{Ar}^+ + \text{Ar}$  is shown in Fig. 4 for a 3-keV parent ion beam and coaxial laser at 7525 Å. The spectrum is symmetric since photofragments ejected into c.m. angles 0 and  $\pi$  are detected with nearly equal efficiency. The center of the spectrum is at 1500 eV, as expected for the photodissociation of a homonuclear diatomic. A scale in the photodissociation energy  $W$ , as calculated from Eq. (2), is shown at the top of the figure. A detailed study has been made of this photodissociation using both coaxial and crossed laser beams at 14 wavelengths between 4579 and 7993 Å. This work<sup>17</sup> was used to determine the  $^2\Sigma_u^+$ ,  $^2\Sigma_g^+$ , and  $^2\Pi_u$  potential curves of  $\text{Ar}_2^+$  to substantially higher accuracy than had been previously possible. The identification of the peaks shown in Fig. 4 was based on this work.

We note that individual vibrational levels are not resolved here, as they have been for  $\text{H}_2^+$ <sup>1,3</sup> and  $\text{O}_2^+$ .<sup>18</sup> This is not surprising since the spacing of the  $\text{Ar}_2^+$  vibrational levels is only about 30 meV, and the rotational spread at our ion source temperature ( $\sim 400$  K) is of this order. When this rotational spread is combined with the finite energy resolution of the apparatus, it is clearly difficult to resolve the individual vibrational levels in  $\text{Ar}_2^+$ . An example will be shown later where vibrational levels

FIG. 5. Spectrum of photofragments observed near  $W = 0$  as a function of wavelength for the transition indicated on the figure.



of  $O_2^+$  are well resolved, and the energy resolution of the apparatus is demonstrated to be about  $5 \times 10^{-4}$ .

The angular dependence of the photodissociation fragment ions has been treated by Zare and Hershbach<sup>19</sup> for cases of zero and infinite dissociation (or predissociation) times and by Ling<sup>20</sup> for varying lifetimes of the intermediate state. In the zero-lifetime case<sup>19</sup> the distributions behave as  $P(\beta) \propto [1 + \beta/2(3 \cos^2 \beta - 1)]$ , where  $\beta$  is the angle between the laser polarization vector and the c.m. fragment ion velocity, and  $-1 \leq \beta \leq 2$ .

The angular distribution can thus vary from isotropic to  $\cos^2 \beta$  or  $\sin^2 \beta$ . Inclusion of varying lifetimes<sup>20</sup> and the effects of spin-orbit coupling<sup>17</sup> significantly complicate this picture, but all basically tend to make the angular distribution more nearly isotropic. Thus fragment ion spectra can often be observed even for basically parallel transitions ( $\Delta A = 0$ ), with coaxial beams where  $P(\beta) \propto \sin^2 \beta$  in the limiting case. An example of this is the  $^2\Sigma_u^+ \leftarrow ^2\Sigma_u^+$  transition shown in Fig. 4.

The coaxial beams arrangement is also well suited to the threshold (or, perhaps better, "predissociation") photofragment spectroscopy.<sup>4</sup> With this technique, a tunable laser is used to investigate photodissociations as a function of laser wavelength, near the threshold, which result in near-zero-energy photofragments. These photodissociations can result from transitions to a repulsive potential, to quasibound levels near the dissociation limit (as in rotational predissociation), or to a predissociating bound state. For predissociations such as are observed in  $O_2^+$ , the resolution depends primarily on the lifetime of the predissociating level, the energy spread in the ion beam, and the linewidth of the laser. The characteristics of the photofragment spectra observed as a function of both kinetic energy and wavelength allow the dissociating state to be identified, and levels of both initial and final states to be determined. A typical wavelength spectrum of the dissociation cross section obtained in this way for the transition  $O_2^+(a^1\Pi_u, v = 4) + h\nu \rightarrow O^+ + O$  is shown in Fig. 5. Here the observed energy resolution is 0.1 meV, as compared with

about 30 meV for normal photofragment spectroscopy.<sup>2,3,17,18</sup> The peaks shown in this figure correspond to transitions between specific rotational and fine structure levels of the  $a^1\Pi_u$  state and the  $b^4\Sigma_u^-$  and  $f^4\Pi_g$  states. Work is currently underway to interpret results such as those shown in Fig. 6 in terms of the energy levels of these states. In order to avoid the complication of the two Doppler-shifted frequencies,  $\nu_0(1 \pm v/c)$ , seen by the beam in the intracavity operation, these data are obtained using the extracavity laser beam.

Another advantage of the coaxial configuration is that the ions in fast beams can have a very narrow Doppler width for absorption of the laser photons. This effect was recognized early in the planning of our apparatus and has since been discussed<sup>21</sup> and exploited<sup>6-9</sup> by others. The energy spreads of a few eV or less in the laboratory frame of reference that characterize

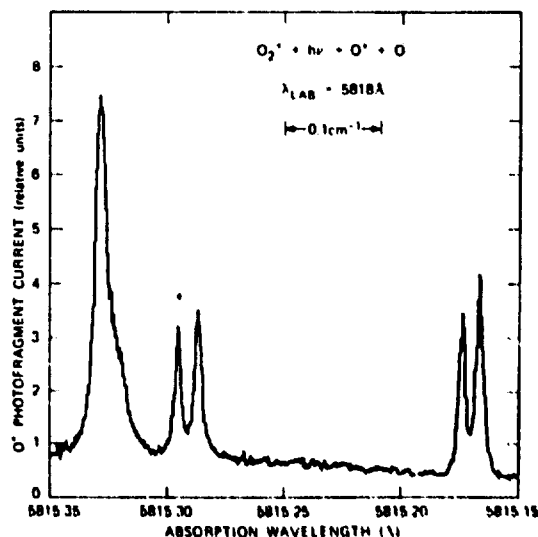


FIG. 6. Velocity-tuned spectrum of  $O^+$  photofragments covering the 0.2-Å wavelength range near 5815 Å indicated in Fig. 5 (laser was operated single mode).

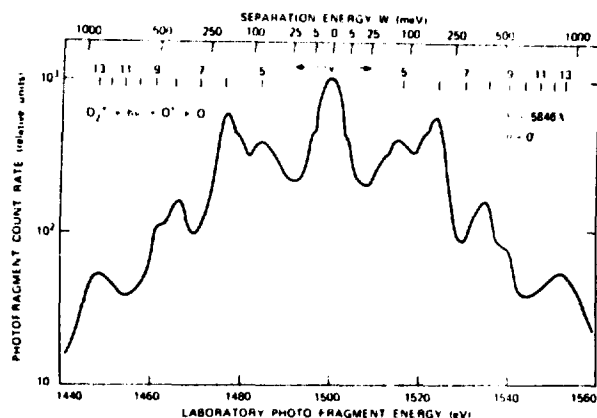


FIG. 7. Photofragment energy spectrum for  $O_2^+(a^1\Pi_g) + h\nu \rightarrow O^+ + O$  obtained at 5846 Å using crossed beams.

beams from many ion sources are unchanged when the ions are accelerated through electrostatic fields and the c.m. distribution of velocity components along the beam axis becomes very narrow, with equivalent kinetic temperatures, as seen by the laser, of a few kelvins. The increased absorption strength at line center and narrowness of optical transition lines can be very useful in high-resolution spectroscopic studies and photoexcitation of ions, or using fast neutral beams produced by charge transfer from ion beams. To achieve optimum resolution, single-frequency lasers must be used. Fine "tuning" of the absorption wavelengths can be achieved at a fixed laser frequency by varying the ion beam energy and Doppler-shifting the absorption lines through the laser frequency. The electrostatic cage shown in Fig. 2 is used to vary the beam energy and obtain such a "velocity-tuned" spectrum. Thus by use of a relatively simple voltage sweep one can effectively use fixed frequency, multiline lasers such as CO and CO<sub>2</sub> lasers as though they were continuously tunable, and can "tune" single-frequency dye lasers in the visible over several angstroms.

An example of a velocity-tuned spectrum is shown in Fig. 6. To obtain this spectrum, the beam energy was swept from 3180 to 3600 eV, while the laser was operating single-frequency near 5818 Å. While the absolute wavelength is uncertain by  $\pm 1$  Å, the relative wavelength is precise to within  $\pm 0.0005$  Å (50 MHz) and the laser linewidth was only 0.0001 Å. The five distinct peaks and the shoulder all lie within the band of 0.2 Å indicated in Fig. 6, and together make up the peak labeled 5815.3 in that figure. The peak widths in this spectrum vary from 170 MHz ( $0.7 \times 10^{-6}$  eV) to 700 MHz ( $2.9 \times 10^{-6}$  eV), reflecting the lifetime of the predissociating states. The 3-eV energy spread of the ion beam causes a Doppler width of 120 MHz which is folded into the observed widths. This technique should yield measurements of transition energies that are an order of magnitude more precise than existing spectrographic measurements.

Obviously, the velocity-tuned spectroscopy described above can also be applied using a collisional detection

scheme<sup>7,8</sup> for both vibrational and electronic transitions. This technique has the advantage of not requiring that the transition lead to predissociation, but requires the use of phase-sensitive detection since a small change in the primary ion current must be observed.

Finally, although this capability has not yet been demonstrated, calculations show that it should not be difficult to observe laser-induced fluorescence from the beam. A photomultiplier and filter for this type of observation are indicated in Fig. 2. In some cases, it should be possible to use a monochromator to observe the fluorescence and determine not only the absorbing states but also the fluorescence channels.

## B. Crossed-beam configuration

When "parallel" transitions ( $\Delta\lambda = 0$ ) in photodissociation yield angular distributions with near-zero fragment ion intensities along the axis in the coaxial arrangement, the laser polarization vector can be oriented along the beam axis by directing the laser at 90° to the ion beam axis in the more traditional arrangement. An example is shown in Fig. 7, which shows the photofragment energy spectra of the photofragments following the  $a^1\Pi_u \rightarrow f^1\Pi_g$  transition in  $O_2^+$ , as was observed by Tabché-Fouhaillé *et al.*<sup>18</sup> (as compared to the wavelength dependence of the cross section near threshold as shown in Fig. 5). Here the vibrational spacings of the  $a^1\Pi_u$  initial state are sufficiently large to be well resolved by the energy analyzer, and the structure seen in Fig. 7 shows the high-energy resolution obtainable in this apparatus.

These data were obtained at 5846 Å, and are directly comparable to the same results shown in Fig. 5 of Ref. 18. The apparent differences are the larger peak at  $W = 0$  and the additional structure in our data. The main vibrational levels observed here ( $v' = 5, 6$ , and 8) agree with those in Ref. 18 within the combined experimental uncertainties ( $\pm 20$  meV), and with the locations expected from optical and photoelectron spectroscopy (see Ref. 18). Dissociation from levels  $v' = 9$  and 13, not observed in Ref. 18, is clearly present here as are shoulders on the  $v' = 5$  and 6 peaks and on the central peak. The  $v' = 5$  and 6 shoulders probably arise from dissociation via the  $O(^3P_1)$  state.<sup>18</sup> The fact that the  $W = 0$  peak is larger in the present data can be due to a very slight difference in wavelength in the two experiments, since the photofragment signal near 5846 Å varies rapidly with wavelength, as in the data of Fig. 5.

## ACKNOWLEDGMENT

This work was supported by the National Science Foundation, Army Research Office, Air Force Office of Scientific Research, and SRI International through its Independent Research and Development Program.

<sup>18</sup> Present address: Ruhruniversität Bochum, 4630 Bochum, West Germany.

<sup>19</sup> Present address: High Energy Physics Laboratory, Stanford University, Stanford, CA.

<sup>20</sup> G. von Busch and G. H. Dunn, *Phys. Rev. A* **5**, 1726 (1972).

- <sup>1</sup> J.-B. Ozenne, D. Pham, and J. Durup, *Chem. Phys. Lett.* **17**, 422 (1972).
- <sup>2</sup> N. P. F. B. van Asselt, J. G. Maas, and J. Los, *Chem. Phys. Lett.* **24**, 555 (1974).
- <sup>3</sup> J. T. Moseley, M. Tajeddine, J. Durup, J.-B. Ozenne, C. Pernot, and A. Tabché-Fouhailé, *Phys. Rev. Lett.* **37**, 891 (1976).
- <sup>4</sup> H. J. André, A. Gaupp, and W. Wittmann, *Phys. Rev. Lett.* **31**, 501 (1973), and subsequent publications. An extreme example of this method is given by H. C. Bryant *et al.*, *Phys. Rev. Lett.* **38**, 228 (1977).
- <sup>5</sup> W. H. Wing, G. A. Ruff, W. E. Lamb, Jr., and J. J. Spezeski, *Phys. Rev. Lett.* **36**, 1488 (1976).
- <sup>6</sup> P. M. Koch, L. D. Gardner, and J. E. Bayfield, *Proc. Fourth Int. Conf. on Beam-Foil Spectroscopy*, edited by I. Sellin and D. Pegg (Plenum, New York, 1976).
- <sup>7</sup> M. Dufay, M. Carré, M. L. Gaillard, G. Neunier, H. Winter, and A. Zgainski, *Phys. Rev. Lett.* **37**, 1678 (1976).
- <sup>8</sup> A. Carrington and P. J. Sarre, *Mol. Phys.* **33**, 1495 (1977).
- <sup>9</sup> H. D. Zeman, *Rev. Sci. Instrum.* **48**, 1079 (1977).
- <sup>10</sup> G. Lange, B. Huber, and K. Weisemann, *J. Phys. E* **9**, 734 (1976).
- <sup>11</sup> H. A. Enge, *Rev. Sci. Instrum.* **35**, 278 (1963).
- <sup>12</sup> L. Hanszen, in *Focusing of Charged Particles*, edited by A. Septier (Academic, New York, 1967), Vol. I.
- <sup>13</sup> H. D. Zeman, K. Jost, and S. Gilad, *Rev. Sci. Instrum.* **42**, 487 (1971).
- <sup>14</sup> H. Matsuda, *Rev. Sci. Instrum.* **32**, 850 (1961).
- <sup>15</sup> H. Wollnik, in *Focusing of Charged Particles*, edited by A. Septier (Academic, London, 1967), Vol. II, p. 263.
- <sup>16</sup> J. T. Moseley, R. P. Saxon, B. A. Huber, P. C. Cosky, R. Abouaf, and M. Tajeddine, *J. Chem. Phys.* **67** (15 Aug. 1977).
- <sup>17</sup> A. Tabché-Fouhailé, J. Durup, J. T. Moseley, J.-B. Ozenne, C. Pernot, and M. Tajeddine, *Chem. Phys.* **17**, 81 (1976).
- <sup>18</sup> R. N. Zare and D. R. Herschbach, *Proc. IEEE* **51**, 173 (1963).
- <sup>19</sup> J. H. Ling, Ph.D. thesis (University of California, San Diego, 1975) (unpublished).
- <sup>20</sup> S. L. Kaufman, *Opt. Commun.* **17**, 309 (1976).

## APPENDIX C

### PHOTODISSOCIATION CROSS SECTIONS OF $\text{Ne}_2^+$ , $\text{Ar}_2^+$ , $\text{Kr}_2^+$ , AND $\text{Xe}_2^+$ FROM 3500 TO 5400 Å

L. C. Lee and G. P. Smith  
Molecular Physics Laboratory  
SRI International, Menlo Park, CA 94025

#### ABSTRACT

The photodissociation (photoabsorption) cross sections of  $\text{Ne}_2^+$ ,  $\text{Ar}_2^+$ ,  $\text{Kr}_2^+$ , and  $\text{Xe}_2^+$  have been measured from 3500 to 5400 Å. The rare gas dimer ions were produced in a drift tube mass spectrometer, and the  $\text{Kr}^+$  and  $\text{Ar}^+$  ion laser lines were used as the photon source. The cross sections decrease monotonically with increasing photon wavelength from 3500 to 5000 Å, and then increase with photon wavelength. The cross sections have values of 1.93, 13.3, 24.8, and  $29.6 \times 10^{-18} \text{ cm}^2$  at 3569 and 3507 Å for  $\text{Ne}_2^+$ ,  $\text{Ar}_2^+$ ,  $\text{Kr}_2^+$ , and  $\text{Xe}_2^+$ , respectively. The current measurements are compared with various theoretical calculations. The dependence of the  $\text{Ne}_2^+$  and  $\text{Ar}_2^+$  cross sections on the effective kinetic temperature was investigated by increasing the ion drift velocity, and was attributed to vibrational excitation of the ions.

## I Introduction

The photoabsorption cross sections of rare gas dimer ions,  $\text{Ne}_2^+$ ,  $\text{Ar}_2^+$ ,  $\text{Kr}_2^+$ , and  $\text{Xe}_2^+$ , have recently been extensively investigated, because these processes are important for detailed characterization and optimization of the rare gas excimer and rare gas-halogen lasers.<sup>1</sup> The photoabsorption of rare gas dimer ions occurs by transitions<sup>2,3</sup> from the bound ground electronic state,  $1(\frac{1}{2})u$ , to repulsive states, which results in dissociation. Several measurements have been made<sup>4,5</sup> on the photodissociation cross sections of the  $1(\frac{1}{2})g \leftarrow 1(\frac{1}{2})u$  transition in the visible region. The experimental data for this transition are reasonably consistent with theoretical calculations.<sup>2-6</sup> On the other hand, absolute photodissociation cross section measurements on the  $2(\frac{1}{2})g \leftarrow 1(\frac{1}{2})u$  transition in the ultraviolet region have only been made by Vanderhoff<sup>7</sup> for  $\text{Ar}_2^+$ ,  $\text{Kr}_2^+$ , and  $\text{Xe}_2^+$  at 3.0 and 3.5 eV, and relative photoabsorption cross section measurements attributed to  $\text{Ar}_2^+$  and  $\text{Kr}_2^+$  have been made by Hunter et al.<sup>8</sup> Theoretical calculations on this photoabsorption band are very extensive.<sup>2,6,9,10</sup> Since this ultraviolet absorption band is important in various laser applications involving the rare gases, additional experimental study of this band is of interest. We report here absolute photodissociation cross section measurements on all four of these ions in the 3500-5400 Å region.

## II Experimental

The measurements reported here were made using a drift tube mass spectrometer which has been described in detail in a previous paper.<sup>11</sup>

Basically, the apparatus consists of an ion source, drift region, mass analyzer, and ion detector. The source and drift regions were filled with the gas of interest at a pressure of 0.4 torr. Ions produced in an electron impact source move along the drift tube under the influence of a weak uniform electric field toward a 1-mm diameter exit aperture. For the photodissociation cross section measurements, the ratio of the applied electric field to the gas number density,  $E/N$ , was limited to 10 and 20 Townsend ( $1 \text{ Td} = 10^{-17} \text{ V-cm}^2$ ). The dependence of the apparent photodissociation cross section on the applied electric field was also studied by varying  $E/N$  from 10 to 170 Td.

The drifting ions intersect a laser beam of diameter  $\sim 1.5 \text{ mm}$  in front of the exit aperture. Various visible lines of  $\text{Ar}^+$  and  $\text{Kr}^+$  ion lasers, tuned by a prism, were used as the photon source. The ions were inside the laser cavity. At the uv lines of the  $\text{Kr}^+$  ion laser, which consists of 25% 3569 Å and 75% 3507 Å, the ions were outside the laser cavity. The photodissociation cross sections at these photon wavelengths are large, so the laser power was reduced to avoid the diffusion effect caused by a high percentage of ion destruction.<sup>12</sup> The laser was mechanically chopped at 100 Hz. The ions of interest were selected by a quadrupole mass spectrometer and detected by a channeltron electron multiplier. The number of ions were

counted for equal periods during which the laser was on and off. The cross sections were placed on an absolute scale by normalization to the  $O^-$  and  $O_2^-$  photodetachment cross sections.<sup>13,14</sup> The reduced ion mobilities used for such normalization were obtained from the recent literature.<sup>15,16</sup>

At each wavelength the number of ion counts were accumulated until the statistical uncertainty in the photodestruction signal was less than 10%. The relative intracavity photon intensity is determined by measurement of the laser output power, with an uncertainty of less than 5% for every wavelength measured. The ion mobility is known to within 5% of its true value. Including the uncertainty in the  $O^-$  and  $O_2^-$  photodetachment cross sections used for normalization, the experimental uncertainty for the absolute photodissociation cross sections is estimated to be  $\pm 20\%$ .

### III Photodissociation Cross Sections at Low E/N

The photodissociation cross sections of molecular ions are dependent<sup>2,9</sup> on the rotational and vibrational populations of the ions. Thus, data on photodissociation cross sections are meaningful only if the populations of the ions are reasonably well defined. The populations of dimer ions can be affected by the applied electric field (see Section IV) and by the processes<sup>5</sup> that form the ions. The dimer ions are mainly formed by a three-body reaction<sup>5</sup> that may produce the ions in vibrationally excited states. However, at low values of E/N (less than about 20 Td), the ion kinetic energies acquired from the field are much less than from thermal collisions at room temperature, and these ions will be well relaxed by collisions in the drift region. They are essentially in thermal equilibrium<sup>5</sup> at near room temperature (300 K). The photodissociation cross sections



of  $\text{Ne}_2^+$ ,  $\text{Ar}_2^+$ ,  $\text{Kr}_2^+$ , and  $\text{Xe}_2^+$  at various photon wavelengths are listed in Table I, where  $\text{Ne}_2^+$  and  $\text{Ar}_2^+$  were measured at 10 Td, and  $\text{Kr}_2^+$  and  $\text{Xe}_2^+$  at 20 Td. The reduced ion mobilities used to calculate their drift velocities are 6.26, 1.83, 0.995, and  $0.617 \text{ cm}^2/\text{V}\cdot\text{sec}$  for  $\text{Ne}_2^{+15}$ ,  $\text{Ar}_2^{+15}$ ,  $\text{Kr}_2^{+16}$  and  $\text{Xe}_2^{+16}$  respectively, in their parent gases.

The photoabsorption bands reported here result from the  $2(\frac{1}{2})g \leftarrow 1(\frac{1}{2})u$  transition.  $1(\frac{1}{2})u$  is the ground electronic state, which is bound.  $2(\frac{1}{2})g$  is a repulsive state dissociating into  $\text{Rg}^+(^2P_{1/2}) + \text{Rg}$ , where  $\text{Rg} = \text{Ne}, \text{Ar}, \text{Kr}, \text{or Xe}$ . These potential curves are described in detail in the literature.<sup>2,3,9,10</sup>

The present results are compared with other experimental measurements<sup>7</sup> and theoretical calculations<sup>2,3,6,9,10</sup> in Figures 1-3. The present measurements agree very well with the experimental data given by Vanderhoff<sup>7</sup> at 3.0 and 3.5 eV for the  $\text{Ar}_2^+$  and  $\text{Kr}_2^+$  ions, but to a lesser degree for  $\text{Xe}_2^+$ . For  $\text{Xe}_2^+$ , the present data are lower than the values of Vanderhoff,<sup>7</sup> but are consistent within the experimental uncertainties. The theoretical calculations agree qualitatively with the present measurements, but quantitatively the theoretical calculations require adjustment. For  $\text{Ar}_2^+$ , the present data agree best with the ab initio calculations of Stevens et al.<sup>2</sup> In these calculations<sup>2</sup> a basis set of Slater-type functions has been used to construct the single-configuration wavefunctions for the four  $\text{Ar}_2^+$  electronic states,  $^2\Sigma_u^+$ ,  $^2\Sigma_g^+$ ,  $^2\Pi_g$ , and  $^2\Pi_u$ . A large basis set has been used in anticipation that the transition moment would be sensitive to any deficiencies. As shown in Fig. 1, their calculations<sup>2</sup> agree very well with

the measurements. The calculations of Moseley et al.<sup>10</sup> for  $\text{Ar}_2^+$  and Abouaf et al.<sup>6</sup> for  $\text{Kr}_2^+$  are semiempirical. In these calculations the potential curves and the transition moments were adopted from the ab initio calculation,<sup>2,3</sup> but the potential curves were adjusted in accord with the observations of photofragment spectroscopy.<sup>6,10</sup> As shown in Fig. 2, these semiempirical calculations for  $\text{Kr}_2^+$  agree quite well with the cross section measurements. The band shapes for the ab initio calculations of Wadt et al.<sup>9</sup> also agree quite well with the measurements, as shown in Figs. 1-3. However, their peak positions require a shift toward shorter wavelengths. This shift has been pointed out by Wadt et al.<sup>9</sup> in comparing their calculations with the photoabsorption measurements of Hunter et al.<sup>8</sup> Nevertheless, this shift of the peak positions requires an adjustment in the potential curves of less than 0.1 eV. This adjustment is within the possible error of 0.1-0.2 eV in the potential curves as indicated by Wadt et al.<sup>9</sup> From these investigations, the photodissociation cross sections of the  $\text{Ar}_2^+$  and  $\text{Kr}_2^+$  dimer ions in the ultraviolet band seem well established. For  $\text{Xe}_2^+$ , however, the discrepancy between the theoretical calculations and experimental measurements is large, indicating the need for substantial adjustment in the potential curves.

The relative cross sections measured by Hunter et al.<sup>8</sup> are consistent with the calculation of Stevens et al.<sup>2</sup> for  $\text{Ar}_2^+$ , and with Abouaf et al.<sup>6</sup> for  $\text{Kr}_2^+$ . When the relative absorption data of Hunter et al.<sup>8</sup> are normalized to the present measurements, both sets of data agree. This

suggests that the absorptions measured by Hunter et al.<sup>8</sup> may be properly attributable to  $\text{Ar}_2^+$  and to  $\text{Kr}_2^+$ .

#### IV Photodissociation Cross Sections at High E/N

An attempt to investigate qualitatively the relationship between E/N and vibrational excitation was made. When an ion drifts under the influence of an electric field, it acquires kinetic energy in addition to its thermal energy. This additional kinetic energy may result in excitation of the dimer ions into higher rotational or vibrational states. Since each state has its own transition probability, the apparent photodissociation cross sections of the dimer ions can depend strongly on their initial excitations.<sup>2,9</sup> The cross sections can thus be affected by the acquired kinetic energy. In order to study this effect, the photodissociation cross sections were measured at a drift distance of 20 cm and a gas pressure of 0.4 torr for various E/N values from 10 to 170 Td. The results for photodissociation of  $\text{Ne}_2^+$  at (3569 and 3507) Å and of  $\text{Ar}_2^+$  at 4131 Å are shown in Table II, in which the ion kinetic energy and the effective translational temperature are also listed. The ion kinetic energy,  $E_K$ , is calculated from the ion drift velocity,  $v_d$ , as given by<sup>15,17,18</sup>

$$E_K = \frac{1}{2} m v_d^2 + \frac{1}{2} M v_d^2 + \frac{3}{2} k T,$$

and the effective kinetic "temperature" is defined as

$$T^* = \frac{2}{3} E_K / k$$

where m and M are the masses of ion and parent molecule, respectively, T is

the gas temperature, and  $k$  is the Boltzmann constant. The ion drift velocity is calculated from the product of the reduced ion mobility,<sup>15,16</sup>  $E/N$ , and the Loschmidt number ( $2.69 \times 10^{19}$  molecules/cm<sup>3</sup>). The effective kinetic temperature is not a true temperature. The translational, rotational, and vibrational populations at an effective kinetic temperature are not expected to have Boltzmann distributions.

As shown in Table II, the apparent cross section of  $\text{Ar}_2^+$  is less affected by the applied electric field than for  $\text{Ne}_2^+$ . This is because  $\text{Ar}_2^+$  has a lower reduced mobility than  $\text{Ne}_2^+$ , and therefore its kinetic energy and resulting vibrational excitation are less sensitive to the applied electric field. Since  $\text{Kr}_2^+$  and  $\text{Xe}_2^+$  have even lower reduced mobilities, their photodissociation cross sections will be less sensitive to  $E/N$  than  $\text{Ar}_2^+$ .

Translational to rotational energy transfer is expected to be a fast process, largely because the energy gap between rotational quantum states is small for the heavier diatomics. The effective rotational temperature of the ions at any  $E/N$  should therefore be close to the effective translational temperature. Furthermore, Stevens et al.<sup>2</sup> have shown theoretically that rotational excitation does not affect the  $\text{Ar}_2^+$  photodissociation cross section. Thus only vibrational excitation is likely to be responsible for any  $E/N$  variation in the cross section. The amount of vibrational excitation is determined by two competing processes: translational to vibrational energy transfer from the kinetically hot  $\text{Ar}_2^+$  (excitation), and vibrational

to translational energy transfer from  $\text{Ar}_2^+$  collisions with the 300 K Ar gas (deexcitation). Such V-T processes are generally slow, but in this case they will be augmented by the switching reaction  $\text{Ar}_2^+ + \text{Ar} \rightarrow \text{Ar} + \text{Ar}_2^+$ . The rates for the excitation and the deexcitation processes may depend on the kinetic energy of the  $\text{Ar}_2^+$  ions acquired. Currently, little quantitative information is available on these important energy transfer rates.

At 4131 Å, the dependence of the  $\text{Ar}_2^+$  photodissociation cross sections on the vibrational and the effective kinetic temperatures is shown in Fig. 4. The cross sections for the vibrational temperature, where the rotational and vibrational populations are in a Boltzmann distribution, were obtained from the theoretical calculations of Stevens et al.<sup>2</sup> For a suitable comparison, the cross section given by Stevens et al.<sup>2</sup> at 300K was normalized to the present measurement. The calculated cross sections of Stevens et al.<sup>2</sup> are larger than the experimental measurements, but their relative values for various vibrational temperatures are probably correct, because their calculations are very consistent with the experimental measurements for both the visible<sup>5</sup> and the ultraviolet bands (see Fig. 1). As shown in Fig. 4, at low effective kinetic temperature,  $T^*$ , the apparent photodissociation cross section is equal to the value at the same vibrational temperature. This temperature equivalence indicates that the excitation process determines the vibrational excitation. At high effective kinetic temperature, the cross section at each  $T^*$  is smaller than the value at the same vibrational temperature. The deexcitation of  $\text{Ar}_2^+$  by collision with

the surrounding 300 K gas becomes dominant, and a maximum vibrational excitation is approached.

The apparent cross sections at the various applied electric fields are not dependent on the ion drift distance. This indicates that a steady state is quickly established at each E/N. The vibrational excitation in the steady state may depend on the gas pressure and composition. From such dependence, quantitative data, such as vibrational excitation and relaxation rates, may be obtained. Further investigations on this subject are planned.

#### V. Concluding Remarks

Including the results reported in a previous paper,<sup>5</sup> the measurements for the rare gas dimer ions now cover the photon wavelength region from 3500 to 8600 Å. Combining these experimental measurements with the extensive theoretical investigations,<sup>2,3,6,9,10</sup> the photodissociation cross sections for the transitions,  $2(\frac{1}{2})g \rightarrow 1(\frac{1}{2})u$  and  $1(\frac{1}{2})g \rightarrow 1(\frac{1}{2})u$ , are very well established.

The photodissociation cross sections monotonically decrease with increasing photon wavelength from 3500 to 5000 Å. At longer photon wavelengths the photodissociation cross sections increase again. This increase is caused by the photoabsorption of the  $1(\frac{1}{2})g \rightarrow 1(\frac{1}{2})u$  transition, which has been investigated previously.<sup>4,5</sup>

The ultraviolet absorption bands of rare gas dimer ions reported here are red shifted with increasing atomic number as predicted by theoretical calculations.<sup>9</sup> At the uv lines (3569 and 3507 Å)  $\text{Ne}_2^+$  is just starting to absorb, while  $\text{Xe}_2^+$  is apparently near the absorption maximum. The oscillator strengths for this ultraviolet absorption band are of the same magnitude<sup>3</sup> for all the rare gas dimer ions reported here, in contrast to the visible band, where the absorption oscillator strengths<sup>3,5</sup> increase from  $\text{Ne}_2^+$  to  $\text{Ar}_2^+$  to  $\text{Kr}_2^+$  to  $\text{Xe}_2^+$ . The ultraviolet band has a large transition moment, and the electronic states involved are similar for all rare gas dimer ions. In contrast, the transition moment responsible for the visible band is very small,<sup>2,3</sup> and its transition strength depends strongly on the spin-orbit coupling<sup>2-6</sup> which increases as the atomic number of the rare gas increases. Because of the weak spin-orbit coupling, the absorption cross section of  $\text{Ne}_2^+$  in the visible region was too small to be measured.

#### Acknowledgement

We are indebted to Dr. J. T. Moseley for suggesting this work and helpful discussions. We also wish to thank Dr. J. W. Peterson and Dr. P. C. Cosby for helpful comments. The authors gratefully acknowledge the use of a laboratory computer system obtained under an equipment grant from the National Science Foundation. This work was supported by the U.S. Army Research Office and the U.S. Air Force Office of Scientific Research.

## REFERENCES

1. J. J. Ewing and C. A. Brau, Appl. Phys. Lett. 27, 350 (1975); E. R. Ault, R. S. Bradford, Jr. and M. L. Bhaumik, Appl. Phys. Lett. 27, 413 (1975); C. A. Brau and J. J. Ewing, Appl. Phys. Lett. 27, 435 (1975); J. A. Mangano and J. H. Jacob, Appl. Phys. Lett. 27, 495 (1975); J. M. Hoffman, A. K. Hays, and G. C. Tisone, Appl. Phys. Lett. 28, 538 (1976); J. R. Murray and H. T. Powell, Appl. Phys. Lett. 29, 252 (1976).
2. W. J. Stevens, M. Gardner, A. Karo, and P. Julianne, J. Chem. Phys. 67, 2860 (1977).
3. W. R. Wadt, J. Chem. Phys. 68, 402 (1978).
4. T. M. Miller, J. H. Ling, R. P. Saxon, and J. T. Moseley, Phys. Rev. A 13, 2171 (1976).
5. L. C. Lee, G. P. Smith, T. M. Miller, and P. C. Cosby, Phys. Rev. 17, 2005 (1978).
6. R. Abouaf, B. A. Huber, P. C. Cosby, R. P. Saxon, and J. T. Moseley, J. Chem. Phys. 68, 2406 (1978).
7. J. A. Vanderhoff, J. Chem. Phys. 68, 3311 (1978).
8. R. O. Hunter, J. Oldenettel, C. Howton, and M. V. McCusker, "UV Absorptions of Rare Gas Ions in E-Beam Pumped Rare Gases," to be published.
9. W. R. Wadt, D. C. Cartwright, and J. S. Cohen, Appl. Phys. Lett. 31, 672 (1977).



10. J. T. Moseley, R. P. Saxon, B. A. Huber, P. C. Cosby, R. Abouaf, and M. Tadjeddine, J. Chem. Phys. 67, 1659 (1977).
11. J. T. Moseley, P. C. Cosby, R. A. Bennett, and J. R. Peterson, J. Chem. Phys. 62, 4826 (1975).
12. G. P. Smith, P. C. Cosby, and J. T. Moseley, J. Chem. Phys. 67 3818 (1977).
13. L. M. Branscomb, S. J. Smith, and G. Tisone, J. Chem. Phys. 43, 2906 (1965).
14. L. C. Lee and G. P. Smith, "Photodissociation and Photodetachment Cross Sections of Atmospheric Negative Ions. VI. Ions in  $O_2/CH_4/H_2O$  Mixtures from 4000 to 8600 Å", to be published.
15. E. W. McDaniel and E. A. Mason, The Mobility and Diffusion of Ions in Gases (Wiley, New York, 1973); also, H. W. Ellis, R. Y. Pai, E. W. McDaniel, E. A. Mason, and L. A. Viehland, Atom. Data. Nucl. Data Tables 17, 177 (1976).
16. H. Helm, J. Phys. B: Atom. Molec. Phys. 9, 2931 (1976).
17. G. H. Wannier, Phys. Rev. 83, 281 (1951); 87, 795 (1952); Bell Syst. Tech. J. 32, 170 (1953).
18. N. McFarland, D. L. Albritton, F. C. Fehsenfeld, E. E. Ferguson, and A. L. Schmeltekopf, J. Chem. Phys. 59, 6620 (1973).

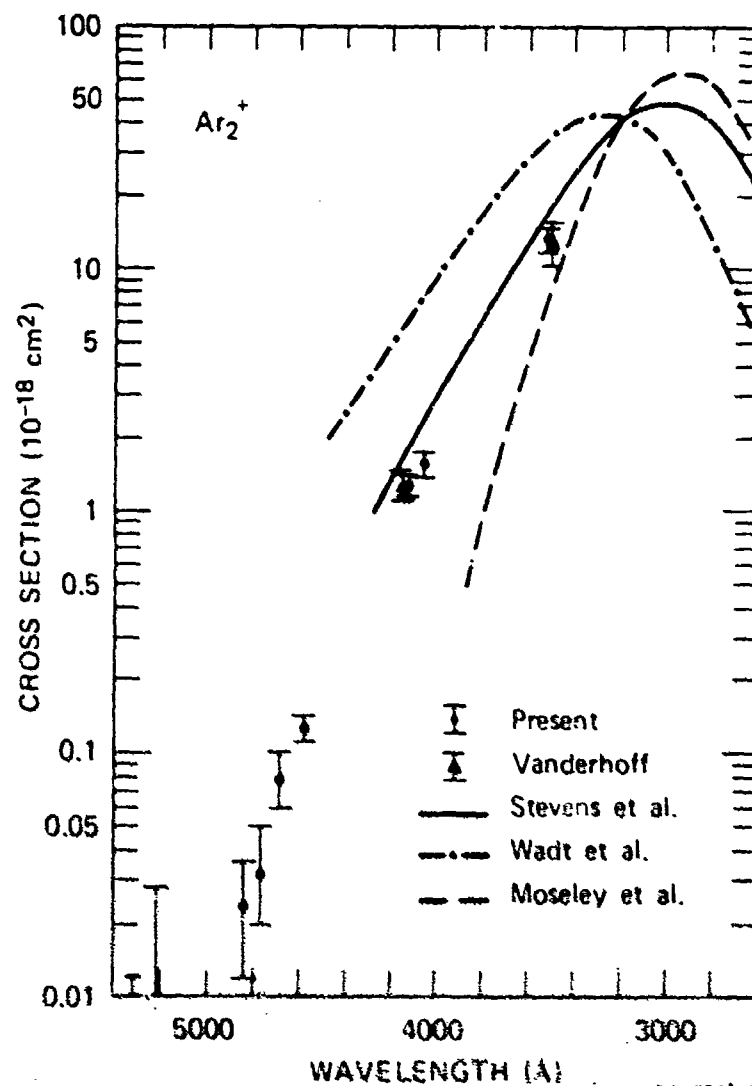
Table I  
 Photodissociation cross sections ( $10^{-18} \text{ cm}^2$ ) of dimer ions  
 at various photon wavelengths,  $\lambda$ .  $\text{Ne}_2^+$  and  $\text{Ar}_2^+$  were  
 measured at 10 Td, and  $\text{Kr}_2^+$  and  $\text{Xe}_2^+$  at 20 Td

$\lambda (\text{\AA})$	$\text{Ne}_2^+$	$\text{Ar}_2^+$	$\text{Kr}_2^+$	$\text{Xe}_2^+$
5309		$< 0.012$	$0.033 \pm 0.004$	$0.028 \pm 0.005$
5208		$< 0.028$	$0.026 \pm 0.006$	$0.022 \pm 0.004$
4825		$0.024 \pm 0.012$	$0.100 \pm 0.014$	$0.102 \pm 0.011$
4762	$< 0.11$	$0.035 \pm 0.016$	$0.122 \pm 0.013$	$0.147 \pm 0.016$
4680		$0.082 \pm 0.022$	$0.203 \pm 0.022$	$0.244 \pm 0.024$
4579		$0.130 \pm 0.012$	$0.39 \pm 0.03$	$0.64 \pm 0.03$
4131	$< 0.09$	$1.05 \pm 0.10$	$3.18 \pm 0.28$	$5.50 \pm 0.55$
4067		$1.60 \pm 0.17$	$3.63 \pm 0.37$	$7.32 \pm 1.33$
{ 3569 3507	$1.93 \pm 0.20$	$13.3 \pm 1.1$	$24.8 \pm 1.9$	$29.6 \pm 2.0$

Table II

Apparent photodissociation cross section  $\sigma(10^{-18} \text{ cm}^2)$ , average ion kinetic energy  $E_K$  (meV), and effective kinetic temperature  $T^*$  (K) at various  $E/N$  ( $10^{-17} \text{ V}\cdot\text{cm}^2$ ).  $\text{Ne}_2^+$  was photodissociated by photons of wavelengths  $(3569 + 3507) \text{ \AA}$  and  $\text{Ar}_2^+$  by  $4131 \text{ \AA}$ .

E/N	$\text{Ne}_2^+$			$\text{Ar}_2^+$		
	$E_K$	$T^*$	$\sigma$	$E_K$	$T^*$	$\sigma$
0	39	300		39	300	
10	48	368	$1.93 \pm 0.20$	40	312	$1.05 \pm 0.10$
20	78	602	$2.96 \pm 0.19$	45	349	$1.45 \pm 0.10$
30				53	406	$1.69 \pm 0.18$
40	208	1604	$3.97 \pm 0.35$	65	502	$1.75 \pm 0.20$
50				78	602	$2.00 \pm 0.23$
60				96	744	$2.88 \pm 0.15$
70				119	917	$3.11 \pm 0.35$
80				145	1118	$3.88 \pm 0.26$
100				208	1604	$4.89 \pm 0.32$
120				281	2173	$6.25 \pm 0.36$
140				359	2775	$7.00 \pm 0.42$
160				440	3398	$7.35 \pm 0.74$
170				462	3571	$8.17 \pm 0.82$



SA-6976-1

FIGURE 1. PHOTODISSOCIATION CROSS SECTIONS FOR Ar<sub>2</sub><sup>+</sup>. The data given by Vanderhoff (Ref. 7) and the theoretical results given by Stevens et al. (Ref. 2), Wadt et al. (Ref. 9), and Moseley et al. (Ref. 10) are shown.

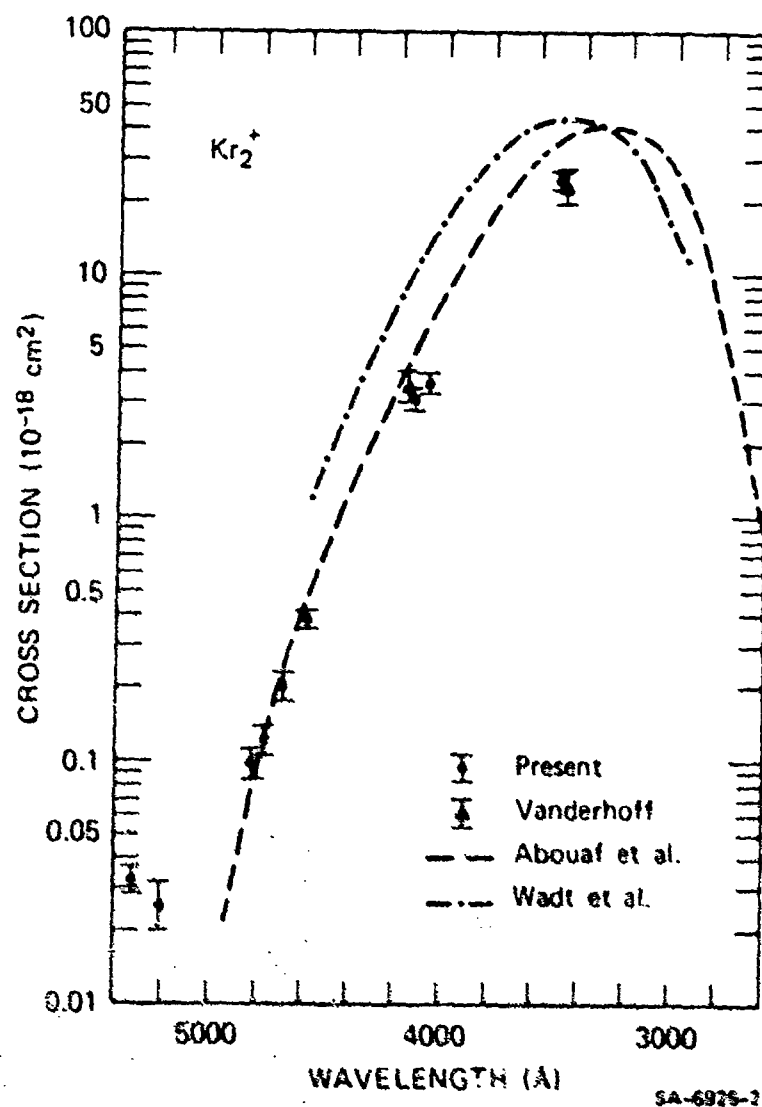


FIGURE 2. PHOTODISSOCIATION CROSS SECTIONS FOR  $Kr_2^+$ . The data given by Vanderhoff (Ref. 7) and the theoretical results given by Abouaf et al. (Ref. 6) and Wadt et al. (Ref. 9) are shown.

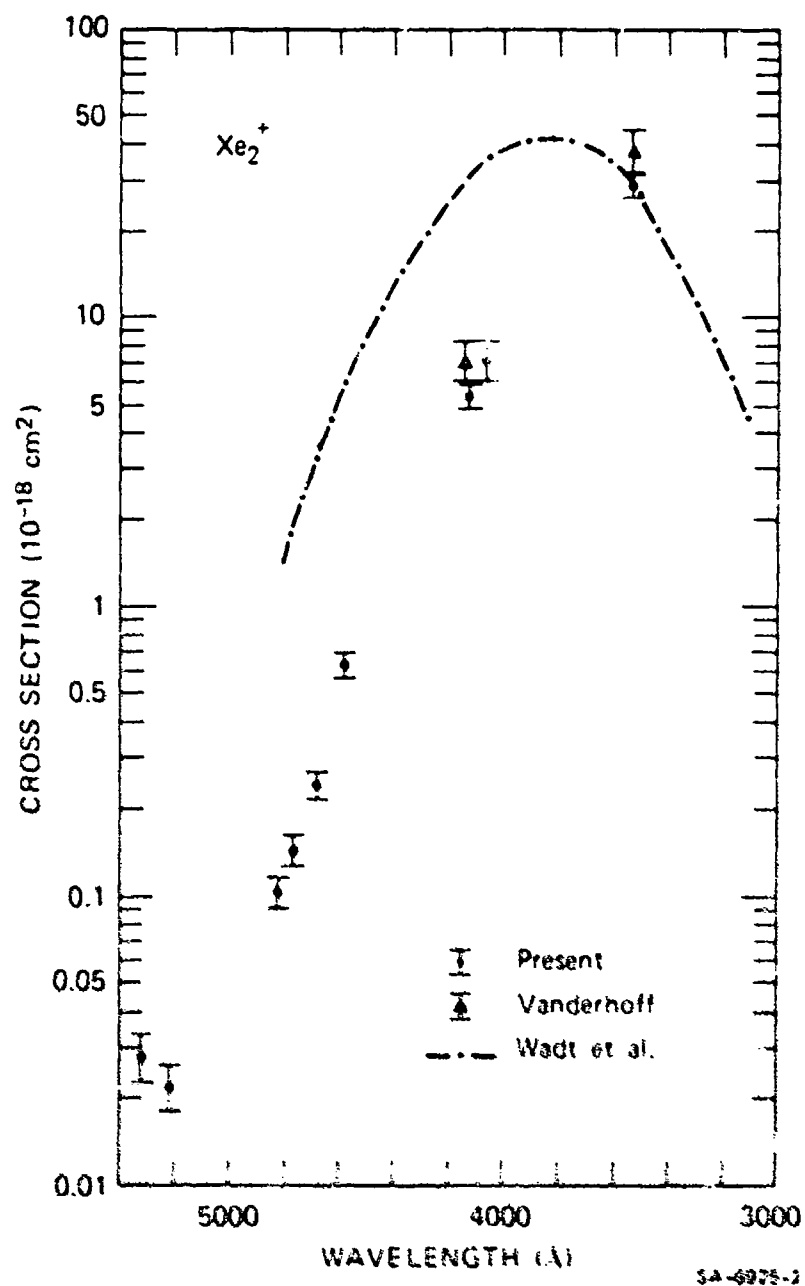
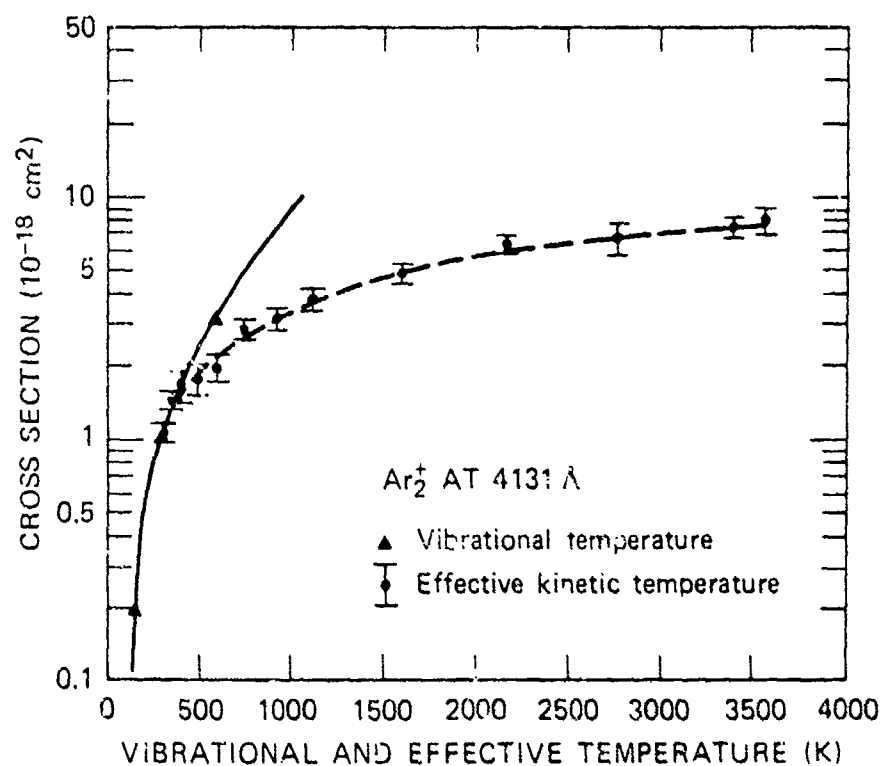


FIGURE 3. PHOTODISSOCIATION CROSS SECTIONS FOR  $\text{Xe}_2^+$ . The data given by Vanderhoff (Ref. 7) and the theoretical results given by Wadt et al. (Ref. 9) are shown.



SA-6925-4

FIGURE 4. THE DEPENDENCE OF THE  $\text{Ar}_2^+$  PHOTODISSOCIATION CROSS SECTIONS ON THE VIBRATIONAL AND THE EFFECTIVE KINETIC TEMPERATURES.  $\text{Ar}^+$  was photodissociated at 4131 Å. The vibrational temperature dependence was adopted from the calculations of Stevens et al. (Ref. 2) and normalized to the present measurement at 300 K.

## Photodissociation of atmospheric positive ions. II. 3500–8600 Å

G. P. Smith and L. C. Lee

Molecular Physics Laboratory, SRI International, Menlo Park, California 94025  
(Received 15 August 1978)

Using a drift tube mass spectrometer, photodissociation cross sections have been measured for many positive atmospheric cluster ions at ion laser and dye laser wavelengths between 3500 and 8600 Å. Structureless cross sections were observed for the dimer ions  $O_2^+$ ,  $NONO^+$ ,  $N_2^+$ , and  $CO_2CO_2^+$ , and for cluster ions of  $O_2^+$ . The nature of the electronic states involved is discussed. Evidence of a second dissociative state for  $O_2^+$  and  $O_2^+ \cdot H_2O$  in the ultraviolet is presented. Upper limits on the cross sections of  $COCO^+$  and cluster ions of  $NO^+$  and  $H_2O^+$  below  $1 \times 10^{-18} \text{ cm}^2$  were established at many wavelengths.

### I. INTRODUCTION

In a previous paper,<sup>1</sup> we reported photodissociation cross sections for several weakly bound positive cluster ions, including  $NONO^+$ ,  $CO_2^+$ , and  $O_2^+ \cdot H_2O$ , in the wavelength region from 5300 to 6700 Å. Since such ions are important in the lower ionosphere and photodissociation by visible sunlight can be an important loss mechanism, our understanding of this region requires the determination of these photodissociation cross sections<sup>2</sup> over a wider range of wavelengths. These extended measurements also provide some information on the electronic states of ions.<sup>3</sup>

We have now extended these measurements to 3500 Å in the near uv and to 8600 Å in the near ir, using both a tunable dye laser and the lines of argon and krypton ion lasers. We report photodissociation cross sections for  $O_2^+$ ,  $NONO^+$ ,  $CO_2CO_2^+$ ,  $N_2^+$ ,  $CO_2^+$ ,  $O_2^+ \cdot H_2O$ , and  $O_2^+ \cdot 2H_2O$ . We have also determined upper limits on the cross sections for the ions  $COCO^+$ ,  $N_2H^+$ ,  $NO^+ \cdot H_2O$ ,  $NO^+ \cdot 2H_2O$ ,  $NO^+ \cdot CO_2$ ,  $NO^+ \cdot N_2$ , and  $H_2O^+ \cdot nH_2O$ ,  $n=0, 1, 2, 3$ . These measurements provide information on the electronic structure and bonding of cluster ions.

### II. EXPERIMENTAL

The drift tube mass spectrometer apparatus has been extensively described previously.<sup>1</sup> Ions formed by electron impact in the source region, and subsequent ion-molecule reactions, drift slowly down the tube under the influence of a weak applied field. At typical values of the ratio of the electric field to the gas density ( $E/N$ ) of 10–20 Td, the ion energy is essentially thermal, and most ions at the end of the drift tube have undergone thousands of collisions with the background gas. For example,  $O_2^+$  in  $O_2$  at 300 K and 10 Td has an average kinetic energy<sup>4</sup> which corresponds to a temperature of 312 K. Even if the effective vibrational temperature is equivalent, no major change in the cross section from added vibrational excitation is expected for such a small 12 K temperature variation. At the end of the drift tube, the ion swarm intersects an intracavity laser beam which is perpendicular to the drift field. The ions then exit the drift region through a 1 mm diam. hole into a high vacuum region where they are mass selected by a quadrupole mass spectrometer and detected by a channel electron multiplier. The laser beam is chopped at

100 Hz and the ions of interest are counted in two separate counters corresponding to laser off ( $I_0$ ) and on ( $I$ ).

Measurements were made using the argon laser lines at 5145, 5017, 4965, 4880, 4658, and 4579 Å, and the krypton laser lines at 5309, 5208, 4962, 4825, 4680, 4131, and 4067 Å. The krypton laser output used for the ultraviolet measurements was 66% at 3507 Å and 34% at 3569 Å. Dye laser measurements were made at 5300–5700 Å using sodium fluorescein, at 5700–6300 Å using rhodamine 6G, at 6200–6900 Å using rhodamine 640, at 7000–7700 Å using oxazine, and at 7700–8600 Å using DEOTC pumped by the krypton laser red lines.<sup>6</sup>

The positive ion photodissociation cross section is measured relative to  $O_2^+$  photodetachment and normalized<sup>7</sup> to the well-established values of this cross section. Thus,  $\sigma(A^+) = \sigma(O_2^+) \times [\ln(I_0/I)K/\phi]_A / [\ln(I_0/I)K/\phi]_{O_2}$ , where  $K$  is the ion mobility and  $\phi$  is the photon flux. The  $O_2^+$  cross sections of Cosby *et al.*<sup>7</sup> were used from 4800 to 6700 Å. Above 6700 Å, the cross sections given by Lee *et al.*,<sup>8</sup> for  $O_2^+$ , measured relative to the  $D^{+3}$  and  $O^{-10}$  photodetachment cross sections, were used. These values are ~20% higher than those of Burch *et al.*,<sup>11</sup> and vary linearly from  $1.15 \times 10^{-18} \text{ cm}^2$  at 7000 Å to  $0.90 \times 10^{-18} \text{ cm}^2$  at 8000 Å. Below 4600 Å, the cross sections for  $O_2^+$  photodetachment given by Burch *et al.*<sup>11</sup> were used. These values are confirmed by our recent measurements<sup>9</sup> on  $O_2^+$  relative to the  $O^+$  cross sections of Branscomb *et al.*<sup>10</sup> The resulting absolute uncertainty in the positive ion photodissociation cross sections from this procedure is about  $\pm 20\%$ . A direct normalization to the  $O^+$  cross section is not possible at the 400 mtorr pressures used to make most positive cluster ions because large amounts of  $O_2^+$ , which produce  $O^+$  photofragments, are present at this pressure.

Unless otherwise noted in the text, all measurements were made at 400 mtorr pressure, 20 cm drift distance, and an  $E/N$  of 10 or 20 Td. The ion mobilities used are those listed previously,<sup>1</sup> and are listed in Table I. Care was taken to avoid those conditions described in our initial report<sup>1</sup> which can cause inaccurate cross section values. Thus, gas partial pressures were chosen to avoid fast ion recombination reactions of the photodissociated fragments, formation of the ion of interest from photodissociation of larger clusters present, and the



TABLE I. Ion mobilities used.

Ion	Gas	Mobility (cm <sup>2</sup> /V s)
O <sub>2</sub> <sup>+</sup>	O <sub>2</sub>	2.08 <sup>a</sup>
NONO <sup>+</sup>	N <sub>2</sub> O	1.45 <sup>b</sup>
CO <sub>2</sub> CO <sub>2</sub> <sup>+</sup>	CO <sub>2</sub>	1.22 <sup>b</sup>
N <sub>2</sub> <sup>+</sup>	N <sub>2</sub>	2.32 <sup>a</sup>
COCO <sup>+</sup>	CO	1.90 <sup>a</sup>
CO <sub>2</sub> <sup>+</sup>	CO <sub>2</sub>	1.25 <sup>b</sup>
O <sub>2</sub> <sup>+</sup> ·H <sub>2</sub> O	O <sub>2</sub>	2.5 <sup>c</sup>
O <sub>2</sub> <sup>+</sup> ·2H <sub>2</sub> O	O <sub>2</sub>	2.4 <sup>c</sup>
N <sub>2</sub> H <sup>+</sup>	N <sub>2</sub>	2.12 <sup>a</sup>
NO <sup>+</sup> ·H <sub>2</sub> O	N <sub>2</sub> O	1.25 <sup>b</sup>
NO <sup>+</sup> ·2H <sub>2</sub> O	N <sub>2</sub> O	1.2 <sup>b</sup>
NO <sup>+</sup> ·CO <sub>2</sub>	CO <sub>2</sub>	1.25 <sup>b</sup>
NO <sup>+</sup> ·N <sub>2</sub>	N <sub>2</sub>	2.3 <sup>b</sup>
H <sub>2</sub> O <sup>+</sup>	O <sub>2</sub>	2.83 <sup>b</sup>
H <sub>2</sub> O <sup>+</sup> ·H <sub>2</sub> O	O <sub>2</sub>	2.36 <sup>b</sup>
H <sub>2</sub> O <sup>+</sup> ·2H <sub>2</sub> O	O <sub>2</sub>	2.22 <sup>b</sup>
H <sub>2</sub> O <sup>+</sup> ·3H <sub>2</sub> O	O <sub>2</sub>	2.15 <sup>b</sup>

<sup>a</sup>Reference 23.<sup>b</sup>Reference 12.<sup>c</sup>Reference 1.

establishment of fast equilibria between the ion of interest and other ions which are present in large concentrations or which have large photodissociation cross sections. All measurements were made at a photodissociation loss below 15% to prevent any effects of diffusion on the cross section values. This required most measurements for NONO<sup>+</sup> and CO<sub>2</sub>CO<sub>2</sub><sup>+</sup> above 5500 Å be made outside the dye laser cavity at very low laser powers.

### III. DIMER IONS

#### A. O<sub>2</sub><sup>+</sup>

The O<sub>2</sub><sup>+</sup> photodissociation cross section data is presented in Fig. 1. The error bars represent one standard deviation relative error attributable to counting statistics. The structureless form of the cross section, examined previously in greater detail from 5700 to 6700 Å, is confirmed over a much wider wavelength range. This behavior is predicted from a pseudohomonuclear diatomic model for dimer ions, with a weakly bound state having the charge equally shared between the two identical O<sub>2</sub> "nuclei," and a repulsive upper state. The cross section peaks near 8100 Å and extrapolation of the long wavelength data suggests a positive cross section to at least 9200 Å. These measurements agree with the results of Beyer and Vanderhoff,<sup>12</sup> also shown in Fig. 1, at various laser wavelengths between 4579 and 6764 Å.

The rise in the cross section below 4000 Å clearly indicates the onset of a second dissociative process, involving an additional excited state of O<sub>2</sub><sup>+</sup>. We also note

the possibility that a third mechanism may be responsible for the long, flat, low cross section between 4000 and 5800 Å. At photon wavelengths shorter than ~5900 Å (above 2.1 eV), production of O<sub>2</sub>(h<sup>1</sup>Σ<sup>+</sup>) from O<sub>2</sub><sup>+</sup> photodissociation is also thermodynamically allowed, and this process may be responsible for the ultraviolet dissociation.

One can also obtain an approximate estimate of the first repulsive state potential from the data. Because little is known about the O<sub>2</sub><sup>+</sup> ground state, other than its dissociation energy and total entropy, we of necessity use only a very simple approach. The ground state is represented by the (O<sub>2</sub>-O<sub>2</sub>)<sup>+</sup> stretch  $r=0$  harmonic oscillator wavefunction, bound by  $D_0=0.41$  eV.<sup>13</sup> The repulsive surface is modeled by a simple point centers of repulsion potential  $V(r)=C(r/r_0)^{-n}$ . To a rough first approximation,<sup>14</sup> the relative photodissociation cross section at energy  $D_0+V(r)$  is given by the square of the harmonic oscillator wavefunction at  $r$  times the frequency. To match the data, we must choose or fit four parameters: the internuclear separation  $r$ , the vibrational stretching frequency  $\omega$ , the index of repulsion  $n$ , and the constant  $C$ . The magnitude of the peak in the calculated cross section is normalized to the experimental value.

Before discussing the choice of parameters, an examination of the approximations involved in this technique is warranted. This "reflection" model is more fully discussed by Herzberg.<sup>14</sup> The cross section is given by  $\sigma(\nu)=\nu(f\int\psi_0'\psi_1'dr)^2$ . The ground state wavefunction  $\psi_0'$  is that for a  $r=0$  harmonic oscillator. The upper state wavefunction  $\psi_1'$  in this model is approximated by a delta function at the classical turning point. The results of this procedure deviate only slightly from those using accurate repulsive eigenfunctions.<sup>15</sup> In using a curved repulsive potential rather than a linear one, a factor related to the proper normalization of the upper state wavefunctions must be introduced. Gislason<sup>16</sup> has shown that  $\psi_1'(r)=(dV/dr)^{1/2}\delta(r)$ . Finally, the trans-

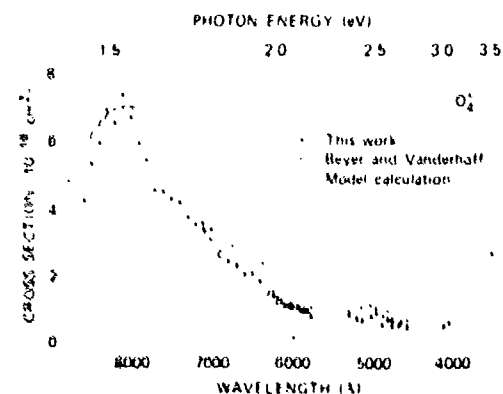


FIG. 1. Photodissociation cross section for O<sub>2</sub><sup>+</sup>. Data from 5700 to 6300 Å are from Ref. 1. Triangles show the data of Ref. 12. The solid line fit is derived from potentials described in the text.

formation to a wavelength scale gives

$$\sigma(\lambda) \propto \lambda^{-1} [\psi''(r)]^2 / [dV(r)/dr].$$

The distance  $r_e$  functions much like a scaling factor, and other parameters are rather insensitive to its variation. Thus,  $r_e$  is fixed at the approximate value<sup>13</sup> of 3.0 Å. In one sense,  $C$  is a similar scaling parameter for the potential energy, but  $C$  is roughly determined experimentally by the wavelength peak in the cross section. Thus,  $r = r_e$  and  $V(r_e) = C = E_{\text{max}} - D_0$ . The two remaining parameters  $\omega_e$  and  $n$  which determine the width and steepness of the potentials, respectively, determine the width of the cross section. The frequency  $\omega_e$  can only be estimated. We choose  $700 \pm 300 \text{ cm}^{-1}$ , in rough accord with Yang and Conway's range.<sup>13</sup> We can now determine (for  $\omega_e = 700$ ) the value of  $n$  which gives the best match to the experimental cross sections, and briefly examine its variation with  $\omega_e$ .

From the  $\text{O}_i^+$  cross section maximum at  $\sim 8000 \text{ Å}$ ,  $C = 1.15 \text{ eV}$ . For  $n = 11$ , the model gives a cross section of half-maximum ( $\sim 3.5 \times 10^{-18} \text{ cm}^2$ ) at 7100 and 9100 Å, and a cross section less than  $1 \times 10^{-18} \text{ cm}^2$  at 6400 Å, as shown by the solid line in Fig. 1. An equally reasonable fit can be accomplished for  $\omega = 400 \text{ cm}^{-1}$  and  $n = 8$  or for  $\omega = 1000 \text{ cm}^{-1}$  and  $n = 16$ . Thus, any of the values typically found<sup>17</sup> for  $n$  are possible. Secondly, the fit to the data is not particularly good, as might be expected for such a simple model. The peak of the experimental cross section is much narrower, especially on the long wavelength side, than the fitted curve indicates. This may signify a flatter repulsive potential than an inverse power potential at larger distances (short wavelength), i.e., the excited state potential may also have some attractive character. In addition to constraining the functional form of the repulsive potential, the model also neglects the effects of low frequency ground state rocking vibrations between the  $\text{O}_2$  nuclei.

The model calculation is somewhat imprecise because the value of  $n$  depends upon an uncertain choice of  $\omega_e$ . In spite of the uncertainties discussed above, the photodissociation cross section measurements do permit a determination of the ion-neutral repulsive potential to within 0.1 eV over a narrow range of distances near the ground state equilibrium radius. Scattering experiments are more difficult and typically<sup>18</sup> yield potentials of similar accuracy. Furthermore, future photofragment spectroscopy experiments on  $\text{O}_i^+$  should provide much new information, permitting a more precise determination of the potentials. This procedure was recently demonstrated for  $\text{Ar}_i^+$ <sup>19</sup> and  $\text{Kr}_i^+$ .<sup>20</sup>

### B. $\text{NONO}^+$

Figure 2 presents the  $\text{NONO}^+$  photodissociation cross section results, measured in  $\text{N}_2\text{O}$ .<sup>1</sup> The cross section varies smoothly from a threshold near 6700 Å, to a broad flat peak of  $2 \times 10^{-17} \text{ cm}^2$  between 7200 and 5800 Å, and declines to  $1.0 \times 10^{-18} \text{ cm}^2$  between 4000 and 3500 Å. The data near the peak was taken with the ions outside the dye laser cavity to avoid a power dependence due to diffusion.<sup>1</sup> Because of the low photon flux and long measurement times, the data near the peak are

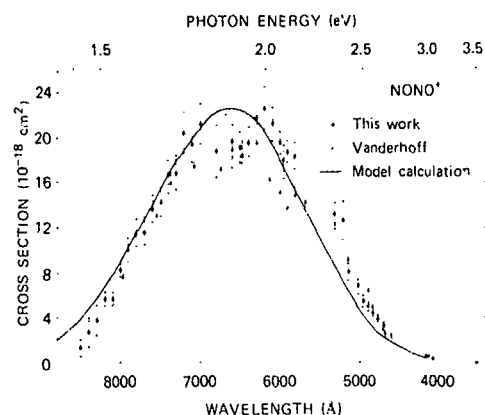


FIG. 2. Photodissociation cross section for  $\text{NONO}^+$ . Triangles represent the results of Ref. 21. The solid line fit is derived from potentials described in the text.

subject to considerable statistical noise. The results agree with those of Vanderhoff,<sup>21</sup> also shown in Fig. 2, and show no significant structure in the cross section. This again indicates direct dissociation via a repulsive upper state.

The data shown in Fig. 2 suggest a possible double peak in the cross section. We believe this is unlikely for several reasons, and that a single, broad, flat peak exists. Measurement of such large cross sections had to be made on ions outside the laser cavity, take a long time, and are subject to large error. Secondly, Vanderhoff's<sup>21</sup> measurements are similar to ours, but show no double peaking. Finally, a second repulsive  $\text{NONO}^+$  state can be ruled out, since the  $\text{NO}^2(\Pi) + \text{NO}^+(\Sigma)$  combination should form only two molecular states.

Note by comparison to  $\text{O}_i^+$  that the peak in the cross section is shifted to shorter wavelengths and is both broader and larger in magnitude. The larger  $\text{NONO}^+$  dissociation energy of 0.59 eV<sup>22</sup> indicates a stronger interaction between fragments, presumably in the repulsive upper state as well, so the  $\sim 0.4 \text{ eV}$  shift in the peak to shorter wavelengths is reasonable. Thus, for the simple potential model,  $C = 1.3 \text{ eV}$  for a peak at 6500 Å. The greater breadth of the cross section compared to  $\text{O}_i^+$  is consistent with a more repulsive, i.e., more strongly interacting, upper state.

Proceeding with a crude estimate for the repulsive potential, we again choose  $r_e \sim 3.0 \text{ Å}$  and  $\omega = 700 \text{ cm}^{-1}$ . The best fit occurs for  $C = 1.3 \text{ eV}$  and  $n = 16$ . This model gives  $\sigma = 12 \times 10^{-18} \text{ cm}^2$  (half-maximum) at 7700 and 5600 Å and  $\sigma = 2.5 \times 10^{-18} \text{ cm}^2$  at 8700 and 4700 Å, and as seen in Fig. 2 fits the data very well, with slight deviations at the flat maximum of the cross section and at the longest and shortest wavelengths. The broad flat peak may indicate that the potentials are more complex, and should include the effects of  $(\text{NO}-\text{NO})^+$  vibrations. The frequency  $\omega_e$  is not well known and may vary considerably for different dimers. Therefore, the steepness parameter  $n$  of the  $\text{NONO}^+$  repulsive potential, which

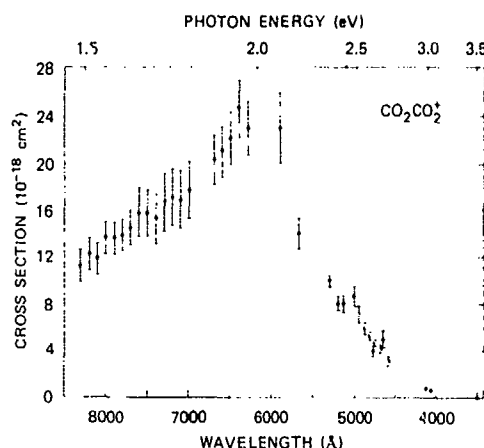


FIG. 3. Photodissociation cross section for  $\text{CO}_2\text{CO}_2^+$ . Data at 5900 Å from Ref. 1.

varies with the choice for  $\omega_e$ , cannot be compared to the value for  $\text{O}_4^+$ , although  $n$  is larger unless  $\omega$  is  $\sim 300 \text{ cm}^{-1}$  less for  $\text{NONO}^+$ . We can only note, from the peak, that the repulsive potential at  $r_e$  is larger for  $\text{NONO}^+$ . Photo-fragment energy spectra should define these potentials more clearly.

#### C. $\text{CO}_2\text{CO}_2^+$

The  $\text{CO}_2\text{CO}_2^+$  photodissociation cross section, shown in Fig. 3, reaches a large maximum exceeding  $2 \times 10^{-17} \text{ cm}^2$  near 6200 Å (2.0 eV). All measurements above

5300 Å were thus taken outside the dye laser cavity, and the lower precision of this technique is reflected in the statistical error bars. The cross section again shows no structure, indicating a repulsive upper state, but no characterization of the potential was attempted since the dissociation energy is unknown. At energies above the maximum, the cross section decreases steadily to a value less than  $1 \times 10^{-18} \text{ cm}^2$  at 3500–4100 Å. At low energies, extrapolation of the long wavelength data indicates a threshold of  $\sim 9500 \text{ Å}$ . The  $\text{CO}_2\text{CO}_2^+$  cross section is asymmetric on a wavelength scale, as reflected by the large values at long wavelength, but is nearly symmetric on an energy scale. This suggests little curvature exists in the repulsive potential at  $r_e$ , although neglected complexities of the ground state potential may also be important. In other respects, the cross section and states of  $\text{CO}_2\text{CO}_2^+$  seem quite similar to  $\text{NONO}^+$ .

#### D. $\text{N}_4^+$

Figure 4 presents the cross section data for  $\text{N}_4^+$ . The ion was produced in 400 mtorr of  $\text{N}_2$ , and drifted a distance of 20 cm at 10 Td. A value of 2.3 was used for the mobility.<sup>23</sup> The cross section has a threshold ( $< 1 \times 10^{-19} \text{ cm}^2$ ) near 6500 Å, and rises steadily into the ultraviolet, reaching  $1.1 \times 10^{-17} \text{ cm}^2$  at 3500 Å. The values agree with those of Miller *et al.*<sup>24</sup> measured between 5700 and 6700 Å. In addition, at 7100 Å, we measured a cross section of  $4 \pm 3 \times 10^{-20} \text{ cm}^2$ , and at 7500 Å established an upper limit (one standard deviation statistical error) of  $3.4 \times 10^{-20} \text{ cm}^2$ . This long low energy tail on the cross section may be due to the small fraction of vibrationally excited  $\text{N}_4^+$  ions in the drift tube at 300 K.

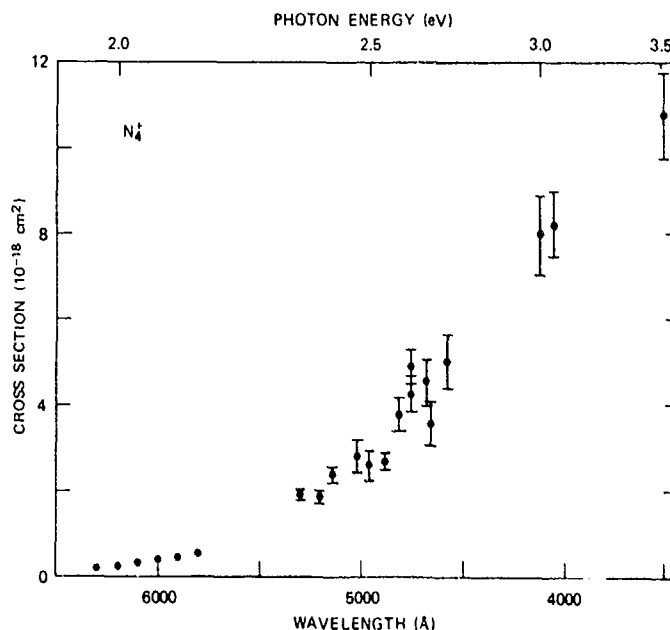


FIG. 4. Photodissociation cross section for  $\text{N}_4^+$ .

Again, for this molecular dimer ion, a smooth structureless cross section characteristic of a repulsive excited state is evident. The  $N_2^+$  dissociation energy is 1.0 eV,<sup>25</sup> larger than  $O_2^+$  and  $NONO^+$ , and the peak in the cross section is thus blue shifted. Yet, although  $N_2^+$  is bound by only 0.4 eV more than  $NONO^+$ , this peak is shifted at least 1.5 eV toward shorter wavelength. This suggests the excited state potential for  $N_2^+$  is much more repulsive at  $r_e$  than that for  $NONO^+$  or  $O_2^+$ .

We also made measurements on the isoelectronic molecular dimer ion  $COCO^+$ , and found cross sections consistent with zero and below  $10^{-18}$  cm<sup>2</sup> at all wavelengths, including 3500 Å. This apparent large shift of the bound-repulsive transition compared to  $N_2^+$  is unexpected. One can speculate that CO, with its dipole moment, forms a more strongly bound ion than  $N_2$ . Horton *et al.*<sup>26</sup> estimate a  $COCO^+$  bond energy of ~1.2 eV. Similarly, as previously observed, the more strongly interacting ion-molecule pair should have the more repulsive upper state. Thirdly, the more strongly bound  $COCO^+$  should have a smaller CO-CO bond distance, and thus the transition samples the repulsive potential at shorter distances, and hence higher energies. Yet, it is hard to envision such a large difference from  $N_2^+$  that the  $COCO^+$  has not begun to photodissociate at 3.5 eV. However, note that the  $N_2^+$  is also quite dramatically blue shifted from the slightly less strongly bound  $NONO^+$  system.

In conclusion, the molecular dimer ions examined in this work can be characterized by a pseudodiatom model. This simple picture models the dimer states after the *gerade* and *ungerade* states of  $H_2^+$ . Ions bound by less than 1 eV exhibit large, smooth, bell-shaped photodissociation cross sections in the visible, characteristic of direct dissociation through a repulsive excited state. The more strongly bound dimers have cross section maxima at higher photon energies, and the mag-

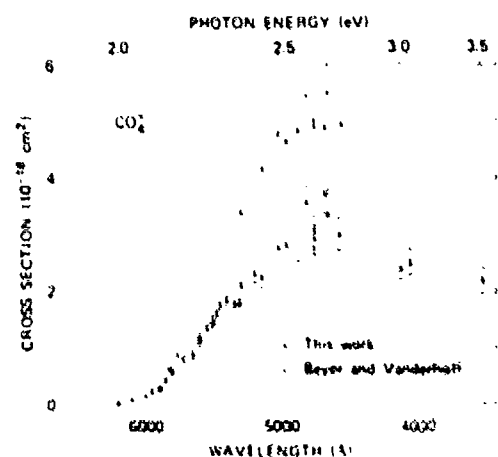


FIG. 5. Photodissociation cross section for  $CO_2^+$ . Data above 5300 Å from Ref. 1. Triangles represent the results of Ref. 12.

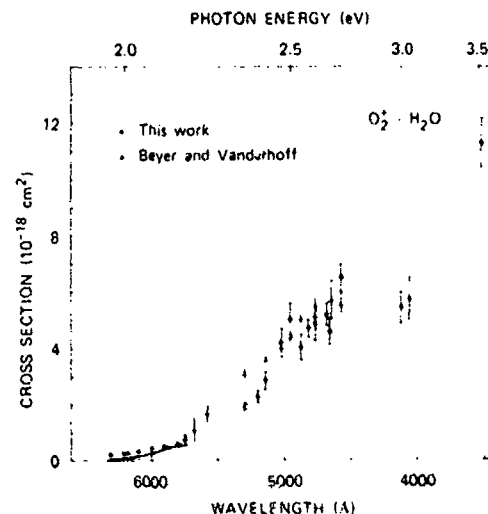


FIG. 6. Photodissociation cross section for  $O_2^+ \cdot H_2O$ . Data from Ref. 11 are shown by the triangles. The solid line above 5700 Å from Ref. 1 corrects the data for the equilibrium with  $O_2^+$ .

nitude of this shift also increases sharply with dissociation energy.

#### IV. $O_2^+$ CLUSTER IONS

The photodissociation cross sections for  $CO_2^+$ ,  $O_2^+ \cdot H_2O$ , and  $O_2^+ \cdot 2H_2O$  are shown in Figs. 5, 6, and 7, respectively. Measurements of Beyer and Vanderhoff<sup>12</sup> have also been included. For the hydrates, mobilities of 2.5 and 2.4 cm<sup>2</sup>/Vs were obtained by mass scaling from the measured value for  $O_2^+$  in oxygen.<sup>27</sup> This differs slightly from the value we used previously (2.1 cm<sup>2</sup>/Vs),<sup>1</sup> but agrees with the mobilities used by Beyer and Vanderhoff.<sup>12</sup> The results reported in this study are those measurements for wavelengths shorter than 5300 Å. The hydrate values are in good agreement with those of Ref. 11 between 4579 and 5308 Å. However, our  $CO_2^+$

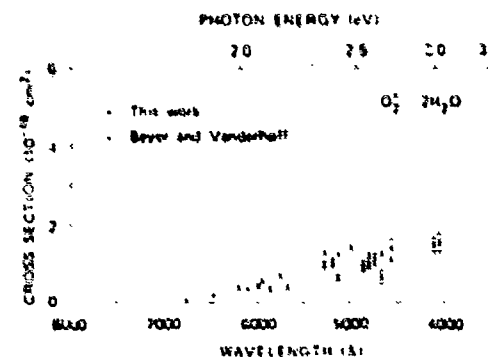


FIG. 7. Photodissociation cross section for  $O_2^+ \cdot 2H_2O$ . Data from Ref. 12.

measurements are consistently about 40% below those of Ref. 12 in this wavelength range. By contrast to our measurements, Beyer and Vanderhoff<sup>12</sup> conducted their measurements with water, and thus with  $O_2^+ \cdot H_2O$ , in the drift tube. If the equilibrium  $CO_2^+ + H_2O \rightleftharpoons O_2^+ \cdot H_2O + CO_2$  is achieved fast enough, a portion of the larger  $O_2^+ \cdot H_2O$  cross section may be incorporated in the  $CO_2^+$  measurement,<sup>1</sup> and this could possibly account for a portion of the discrepancy in results.

These results confirm and supplement the results obtained earlier<sup>1,12</sup> at long wavelengths. The  $O_2^+$  based ions appear to have structureless cross sections indicating a repulsive upper state. A more detailed dye laser examination of  $CO_2^+$  and  $O_2^+ \cdot H_2O$  in the blue region of the spectrum is planned, to clarify the shape of the cross sections and to search further for any structure in the cross sections. As Beyer and Vanderhoff<sup>12</sup> have suggested, one can probably characterize the photodissociation as a transition between the weak electrostatically bound  $O_2^+ \cdot X$  ground state and an excited charge transfer state  $X^+ \cdot O_2$ . The upper state will probably be repulsive or only very weakly bound. The potentials are similar to the dimer ion model, except that the asymptotic limits of the states no longer coincide. The thermodynamic threshold is given by the dissociation energy ( $\sim 0.3$  eV<sup>1,12</sup> for  $CO_2^+$  and  $\sim 0.7$  eV<sup>27</sup> for  $O_2^+ \cdot H_2O$ ) plus the difference between the  $X$  and  $O_2$  ionization potentials.

For all three ions, there is evidence for a second dissociative channel at higher photon energies. The  $CO_2^+$  cross section fails to decrease in the expected symmetrical pattern, suggesting the possibility of a second process at high energies. We note that photodissociation to  $CO_2$  and  $O_2(h\nu)$  is thermodynamically allowed above  $\sim 3.0$  eV,<sup>14</sup> and may correspond to the apparent ultraviolet channel. The local minimum near 4000 Å for  $O_2^+ \cdot H_2O$  more clearly supports a two channel interpretation. Here, we note the thermodynamic thresholds for production of  $O_2(h\nu)$  or  $H_2O^+(^1A_1)$  are 2.9 and 3.0 eV, respectively.<sup>14,22</sup> Photofragment spectroscopy should again prove useful in clarifying the ultraviolet channels.

For the double hydrate, the sharp rise in the cross section after a long gradually rising pattern may also suggest a second channel. Considering the lack of information on photofragments, the main potential photoprocesses, and the difficulty of describing the  $O_2^+ \cdot 2H_2O$

electronic states based on the simple model presented above, an interpretation of this cross section in terms of the molecular potentials was not attempted.

There is a fundamental difference between the positive and negative ion hydrate photodissociations studied in this laboratory. While the positive ion hydrates are characterized by a charge transfer transition, for the negative ion hydrates, the transition appears to be centered on the parent ion. This behavior is clearly reflected by the very similar  $O_3^+$ ,  $O_3^+ \cdot H_2O$ , and  $O_3^+ \cdot 2H_2O$  cross sections,<sup>23</sup> and is attributable to the fact that  $O_3$  has a visible absorption and  $H_2O^+$  is unstable.

## V. NONDISSOCIATING IONS

### A. $NO^+$ clusters

Table II gives upper limits for the photodissociation cross sections of various  $NO^+$  cluster ions at Kr<sup>+</sup> laser wavelengths from 3500–5309 Å. These ions were previously examined at longer wavelengths.<sup>1</sup> All measurements are consistent with zero cross sections, and the upper limits presented include one standard deviation from statistical counting error. Limits below  $1 \times 10^{-13}$  cm<sup>2</sup> were generally set, although the extreme difficulty of producing more than a trace of  $NO^+ \cdot N_2$  in the drift tube<sup>1</sup> precluded such precision for this ion. Zero cross sections are expected for these  $NO^+$  cluster ions from the simple charge transfer electronic states model. The lowest possible thermodynamic thresholds, given by the differences in ionization potentials<sup>24</sup> between  $NO$  and  $H_2O$ ,  $CO_2$ , and  $N_2$ , are 3.4, 4.5, and 6.3 eV, respectively.

### B. Hydronium ions

As Table II also illustrates, we have extended our earlier measurements on the ions  $H_3O^+ \cdot (H_2O)_n$ ,  $n = 0, 1, 2, 3$ , to shorter wavelengths. Photodissociation cross sections consistent with zero and limits below  $1 \times 10^{-13}$  cm<sup>2</sup> were again determined. Measurements at 3500 Å were made in  $N_2O$  to avoid apparent hydronium ion photodestruction attributable to the large photodissociation cross sections of the precursors  $O_2^+ \cdot H_2O$  and  $O_2^+ \cdot 2H_2O$  ions in oxygen.

The nondissociative behavior of  $H_3O^+$  is not surprising, since hydrogen atom loss requires 3.6 eV.<sup>25</sup> The  $H_3O^+$   $\cdot H_2O$  ion has a symmetric structure, and its zero photo-

TABLE II Upper limits on cross sections  $\sigma$ , cm<sup>2</sup>

$\lambda$ , Å	3500	3509	4047	4481	4844	5168	5309
$NO^+$	$< 1.1 \times 10^{-13}$	$< 1.1 \times 10^{-13}$	$< 1.1 \times 10^{-13}$	$< 1.1 \times 10^{-13}$	$< 1.1 \times 10^{-13}$	$< 1.1 \times 10^{-13}$	$< 1.1 \times 10^{-13}$
$NO^+ \cdot H_2O$	$< 1.1 \times 10^{-13}$	$< 1.1 \times 10^{-13}$	$< 1.1 \times 10^{-13}$	$< 1.1 \times 10^{-13}$	$< 1.1 \times 10^{-13}$	$< 1.1 \times 10^{-13}$	$< 1.1 \times 10^{-13}$
$NO^+ \cdot 2H_2O$	$< 1.1 \times 10^{-13}$	$< 1.1 \times 10^{-13}$	$< 1.1 \times 10^{-13}$	$< 1.1 \times 10^{-13}$	$< 1.1 \times 10^{-13}$	$< 1.1 \times 10^{-13}$	$< 1.1 \times 10^{-13}$
$NO^+ \cdot 3H_2O$	$< 1.1 \times 10^{-13}$	$< 1.1 \times 10^{-13}$	$< 1.1 \times 10^{-13}$	$< 1.1 \times 10^{-13}$	$< 1.1 \times 10^{-13}$	$< 1.1 \times 10^{-13}$	$< 1.1 \times 10^{-13}$
$H_3O^+$	$< 1.1 \times 10^{-13}$	$< 1.1 \times 10^{-13}$	$< 1.1 \times 10^{-13}$	$< 1.1 \times 10^{-13}$	$< 1.1 \times 10^{-13}$	$< 1.1 \times 10^{-13}$	$< 1.1 \times 10^{-13}$
$H_3O^+ \cdot H_2O$	$< 1.1 \times 10^{-13}$	$< 1.1 \times 10^{-13}$	$< 1.1 \times 10^{-13}$	$< 1.1 \times 10^{-13}$	$< 1.1 \times 10^{-13}$	$< 1.1 \times 10^{-13}$	$< 1.1 \times 10^{-13}$
$H_3O^+ \cdot 2H_2O$	$< 1.1 \times 10^{-13}$	$< 1.1 \times 10^{-13}$	$< 1.1 \times 10^{-13}$	$< 1.1 \times 10^{-13}$	$< 1.1 \times 10^{-13}$	$< 1.1 \times 10^{-13}$	$< 1.1 \times 10^{-13}$
$H_3O^+ \cdot 3H_2O$	$< 1.1 \times 10^{-13}$	$< 1.1 \times 10^{-13}$	$< 1.1 \times 10^{-13}$	$< 1.1 \times 10^{-13}$	$< 1.1 \times 10^{-13}$	$< 1.1 \times 10^{-13}$	$< 1.1 \times 10^{-13}$
$H_3O^+ \cdot 4H_2O$	$< 1.1 \times 10^{-13}$	$< 1.1 \times 10^{-13}$	$< 1.1 \times 10^{-13}$	$< 1.1 \times 10^{-13}$	$< 1.1 \times 10^{-13}$	$< 1.1 \times 10^{-13}$	$< 1.1 \times 10^{-13}$
$H_3O^+ \cdot 5H_2O$	$< 1.1 \times 10^{-13}$	$< 1.1 \times 10^{-13}$	$< 1.1 \times 10^{-13}$	$< 1.1 \times 10^{-13}$	$< 1.1 \times 10^{-13}$	$< 1.1 \times 10^{-13}$	$< 1.1 \times 10^{-13}$
$H_3O^+ \cdot 6H_2O$	$< 1.1 \times 10^{-13}$	$< 1.1 \times 10^{-13}$	$< 1.1 \times 10^{-13}$	$< 1.1 \times 10^{-13}$	$< 1.1 \times 10^{-13}$	$< 1.1 \times 10^{-13}$	$< 1.1 \times 10^{-13}$
$H_3O^+ \cdot 7H_2O$	$< 1.1 \times 10^{-13}$	$< 1.1 \times 10^{-13}$	$< 1.1 \times 10^{-13}$	$< 1.1 \times 10^{-13}$	$< 1.1 \times 10^{-13}$	$< 1.1 \times 10^{-13}$	$< 1.1 \times 10^{-13}$
$H_3O^+ \cdot 8H_2O$	$< 1.1 \times 10^{-13}$	$< 1.1 \times 10^{-13}$	$< 1.1 \times 10^{-13}$	$< 1.1 \times 10^{-13}$	$< 1.1 \times 10^{-13}$	$< 1.1 \times 10^{-13}$	$< 1.1 \times 10^{-13}$
$H_3O^+ \cdot 9H_2O$	$< 1.1 \times 10^{-13}$	$< 1.1 \times 10^{-13}$	$< 1.1 \times 10^{-13}$	$< 1.1 \times 10^{-13}$	$< 1.1 \times 10^{-13}$	$< 1.1 \times 10^{-13}$	$< 1.1 \times 10^{-13}$
$H_3O^+ \cdot 10H_2O$	$< 1.1 \times 10^{-13}$	$< 1.1 \times 10^{-13}$	$< 1.1 \times 10^{-13}$	$< 1.1 \times 10^{-13}$	$< 1.1 \times 10^{-13}$	$< 1.1 \times 10^{-13}$	$< 1.1 \times 10^{-13}$
$H_3O^+ \cdot 11H_2O$	$< 1.1 \times 10^{-13}$	$< 1.1 \times 10^{-13}$	$< 1.1 \times 10^{-13}$	$< 1.1 \times 10^{-13}$	$< 1.1 \times 10^{-13}$	$< 1.1 \times 10^{-13}$	$< 1.1 \times 10^{-13}$
$H_3O^+ \cdot 12H_2O$	$< 1.1 \times 10^{-13}$	$< 1.1 \times 10^{-13}$	$< 1.1 \times 10^{-13}$	$< 1.1 \times 10^{-13}$	$< 1.1 \times 10^{-13}$	$< 1.1 \times 10^{-13}$	$< 1.1 \times 10^{-13}$
$H_3O^+ \cdot 13H_2O$	$< 1.1 \times 10^{-13}$	$< 1.1 \times 10^{-13}$	$< 1.1 \times 10^{-13}$	$< 1.1 \times 10^{-13}$	$< 1.1 \times 10^{-13}$	$< 1.1 \times 10^{-13}$	$< 1.1 \times 10^{-13}$
$H_3O^+ \cdot 14H_2O$	$< 1.1 \times 10^{-13}$	$< 1.1 \times 10^{-13}$	$< 1.1 \times 10^{-13}$	$< 1.1 \times 10^{-13}$	$< 1.1 \times 10^{-13}$	$< 1.1 \times 10^{-13}$	$< 1.1 \times 10^{-13}$
$H_3O^+ \cdot 15H_2O$	$< 1.1 \times 10^{-13}$	$< 1.1 \times 10^{-13}$	$< 1.1 \times 10^{-13}$	$< 1.1 \times 10^{-13}$	$< 1.1 \times 10^{-13}$	$< 1.1 \times 10^{-13}$	$< 1.1 \times 10^{-13}$
$H_3O^+ \cdot 16H_2O$	$< 1.1 \times 10^{-13}$	$< 1.1 \times 10^{-13}$	$< 1.1 \times 10^{-13}$	$< 1.1 \times 10^{-13}$	$< 1.1 \times 10^{-13}$	$< 1.1 \times 10^{-13}$	$< 1.1 \times 10^{-13}$
$H_3O^+ \cdot 17H_2O$	$< 1.1 \times 10^{-13}$	$< 1.1 \times 10^{-13}$	$< 1.1 \times 10^{-13}$	$< 1.1 \times 10^{-13}$	$< 1.1 \times 10^{-13}$	$< 1.1 \times 10^{-13}$	$< 1.1 \times 10^{-13}$
$H_3O^+ \cdot 18H_2O$	$< 1.1 \times 10^{-13}$	$< 1.1 \times 10^{-13}$	$< 1.1 \times 10^{-13}$	$< 1.1 \times 10^{-13}$	$< 1.1 \times 10^{-13}$	$< 1.1 \times 10^{-13}$	$< 1.1 \times 10^{-13}$
$H_3O^+ \cdot 19H_2O$	$< 1.1 \times 10^{-13}$	$< 1.1 \times 10^{-13}$	$< 1.1 \times 10^{-13}$	$< 1.1 \times 10^{-13}$	$< 1.1 \times 10^{-13}$	$< 1.1 \times 10^{-13}$	$< 1.1 \times 10^{-13}$
$H_3O^+ \cdot 20H_2O$	$< 1.1 \times 10^{-13}$	$< 1.1 \times 10^{-13}$	$< 1.1 \times 10^{-13}$	$< 1.1 \times 10^{-13}$	$< 1.1 \times 10^{-13}$	$< 1.1 \times 10^{-13}$	$< 1.1 \times 10^{-13}$

dissociation cross section at 3500 Å indicates any dissociative, repulsive states correlating to  $\text{H}_3\text{O}^+ + \text{H}_2\text{O}$  products lie at higher energy. Production of  $\text{H}_2\text{O}^+$  would require over 5.5 eV of energy. Other investigators<sup>12,30</sup> have also observed zero cross sections for these ions at various wavelengths.

Also recorded in Table II are upper limits measured for photodissociation of  $\text{COCO}^+$ , discussed earlier, and  $\text{N}_2\text{H}^+$ . One final series of cluster ions of ionospheric importance are the alkali ion hydrates such as  $\text{Na}^+ \cdot \text{H}_2\text{O}$ . According to the simple electrostatic bonding and charge transfer state model, which has proved successful for positive cluster ions thus far, no excited states should exist below 7 eV, the  $\text{H}_2\text{O}^+ + \text{Na}$  limit, due to the very low sodium ionization potential.

## VI. CONCLUSIONS

We have presented data, and set upper limits, on the photodissociation cross sections of most positive cluster ions of atmospheric importance throughout the visible spectrum. In general, symmetric clusters such as  $\text{NONO}^+$ , and cluster ions of  $\text{O}_2^+$ , have large structureless cross sections, while  $\text{NO}^+$  and  $\text{H}_3\text{O}^+$  cluster ions do not photodissociate below 3.5 eV. A simple electronic model based on weak electrostatic bonding and a pseudodiatom characterizations of the electronic states is sufficient to account for the observations for both symmetric and asymmetric ions. We will calculate the solar loss rates via photodissociation for these ions, as well as the negative ions studied in this laboratory, and discuss the implications for D region ion chemistry in a subsequent paper.<sup>31</sup>

## ACKNOWLEDGMENTS

The authors wish to thank Drs. J. T. Moseley, P. C. Cosby, D. L. Huestis, R. P. Saxon, and J. R. Peterson for their advice and assistance. Computer services used for these measurements were provided through an instrumentation grant from the National Science Foundation. This research was supported by the U. S. Army Research Office.

<sup>1</sup>G. P. Smith, P. C. Cosby, and J. T. Moseley, *J. Chem. Phys.*, **67**, 3818 (1977).

<sup>2</sup>L. Thomas, *Radio Sci.*, **9**, 121 (1974); E. E. Ferguson and F. E. Fehsenfeld, *J. Geophys. Res.*, **74**, 5743 (1969); J. M. Heimerl, J. A. Vanderhoff, L. J. Puckett, and F. E. Niles, *BRL Report 7570*, Aberdeen Proving Ground, MD (1972), and *EOS Trans. AGU*, **52**, 870 (1971); F. E. Niles, J. M. Heimerl, and G. W. Keller, *EOS Trans. AGU*, **53**, 456 (1972).

<sup>3</sup>G. E. Busch and K. R. Wilson, *J. Chem. Phys.*, **56**, 3626

(1972); J. T. Moseley, P. C. Cosby, and J. R. Peterson, *J. Chem. Phys.*, **65**, 2512 (1976).

<sup>4</sup>P. C. Cosby, R. A. Bennett, J. R. Peterson, and J. T. Moseley, *J. Chem. Phys.*, **63**, 1612 (1975).

<sup>5</sup>E. W. McDaniel and E. H. Mason, *The Mobility and Diffusion of Ions in Gases* (Wiley, New York, 1973).

<sup>6</sup>Dye sources were as follows: Rhodamine 640 from Exciton Chemical Co., oxazine perchlorate from Eastman Kodak Co., LEOTC from Exciton Chemical Co., Nippon Kankoh-Shikiso, Kenyusho, Japan.

<sup>7</sup>P. C. Cosby, J. H. Ling, J. R. Peterson, and J. T. Moseley, *J. Chem. Phys.*, **65**, 5267 (1976).

<sup>8</sup>L. C. Lee and G. P. Smith, *J. Chem. Phys.*, (to be published).

<sup>9</sup>K. L. Bell and A. E. Kingston, *Proc. Phys. Soc. London*, **90**, 895 (1967).

<sup>10</sup>L. M. Branscomb, S. J. Smith, and G. Tisone, *J. Chem. Phys.*, **43**, 2906 (1965).

<sup>11</sup>D. S. Burch, S. J. Smith, and L. M. Branscomb, *Phys. Rev.*, **112**, 171 (1958).

<sup>12</sup>R. A. Beyer and J. A. Vanderhoff, *J. Chem. Phys.*, **65**, 2313 (1976).

<sup>13</sup>J.-H. Yang and D. C. Conway, *J. Chem. Phys.*, **40**, 1729 (1964).

<sup>14</sup>G. Herzberg, *Spectra of Diatomic Molecules* (Van Nostrand, New York, 1950), p. 391.

<sup>15</sup>A. S. Coolidge, H. M. James, and R. D. Present, *J. Chem. Phys.*, **4**, 193 (1936).

<sup>16</sup>E. A. Gislason, *J. Chem. Phys.*, **58**, 3702 (1973).

<sup>17</sup>J. O. Hirschfelder, C. F. Curtiss, and R. B. Bird, *Molecular Theory of Gases and Liquids* (Wiley, New York, 1954).

<sup>18</sup>P. R. Jones, G. M. Conklin, D. C. Lorents, and R. E. Olson, *Phys. Rev. A*, **10**, 102 (1974).

<sup>19</sup>J. T. Moseley, R. P. Saxon, B. A. Huber, P. C. Cosby, R. Abouaf, and M. Tadjeddine, *J. Chem. Phys.*, **67**, 1659 (1977).

<sup>20</sup>R. Abouaf, B. A. Huber, P. C. Cosby, R. P. Saxon, and J. T. Moseley, *J. Chem. Phys.*, **68**, 2496 (1978).

<sup>21</sup>J. A. Vanderhoff, *J. Chem. Phys.*, **67**, 2332 (1977).

<sup>22</sup>C. Y. Ng, P. W. Tiedemann, B. H. Mahan, and Y. T. Lee, *J. Chem. Phys.*, **66**, 3985 (1977).

<sup>23</sup>H. W. Ellis, R. Y. Pai, E. W. McDaniel, E. A. Mason, and L. A. Viehland, *At. Data Nucl. Data Tables*, **17**, 177 (1976).

<sup>24</sup>T. M. Miller, J. L. Heidrich, and J. T. Moseley, *IX ICPEAC Abstracts of Papers* (University of Washington, Seattle, 1975), p. 7.

<sup>25</sup>J. D. Payzant and P. Kebabian, *J. Chem. Phys.*, **53**, 4723 (1970).

<sup>26</sup>R. L. Horton, J. L. Franklin, and B. Mazzeo, *J. Chem. Phys.*, **62**, 1739 (1975).

<sup>27</sup>C. J. Howard, V. M. Bierbaum, H. W. Rundle, and F. Kaufman, *J. Chem. Phys.*, **57**, 3491 (1972).

<sup>28</sup>J. G. Dillard, K. Draxl, J. L. Franklin, F. H. Field, J. T. Heron, and H. H. Rosenstock, *Natl. Stand. Ref. Data Ser. Natl. Bur. Stand.*, **26** (1969).

<sup>29</sup>P. C. Cosby, J. T. Moseley, and G. P. Smith, *J. Chem. Phys.*, **69**, 710 (1978).

<sup>30</sup>W. R. Henderson and A. L. Schmeltekopf, *J. Chem. Phys.*, **57**, 4502 (1972).

<sup>31</sup>J. R. Peterson, L. C. Lee, G. P. Smith, P. C. Cosby, J. T. Moseley, *J. Geophys. Res.*, (to be submitted).